

國立交通大學
電子物理系所
碩士論文

利用飛秒光譜檢測具應變釷錳氧薄膜內
錳離子 $d-d$ 能隙與尼爾溫度之研究

**Mn³⁺ $d-d$ Energy Difference and Néel Temperature
in Strained YMnO₃ Thin Films
Probed by Femtosecond Spectroscopy**

研究生：陳耀宗

指導教授：吳光雄 教授

中華民國九十九年六月

誌謝

兩年多的研究生生涯伴隨論文定稿劃下休止符，這段期間承蒙吳光雄教授不辭辛勞地給予我許多研究上的建議，以及帶領我解決許多實驗上遇到的問題，在此致上由衷的感謝。另外要感謝固態研究群的莊振益教授、林俊源教授、溫增明教授、羅志偉教授以及台大物理系傅昭銘教授對本論文仔細地審核並提供寶貴的建議，讓本論文更臻於完善。感謝加州大學電機系劉佳明教授除了給予我在共軛焦顯微鏡架設的指導外，研究與經驗上的分享也使我有很深刻的學習。

研究期間，特別感謝伍道樑總教官、李佐文教官、簡泰淇教官、李昭麟教官、李耀威教官、楊恭賜教官、鄧惠成教官、陳天生教官、鄒立宇教官、馬毓君教官與劉美華教官對於我的愛護及生活上的照顧。感謝陳裕仁學長、石訓全學長、林宗漢學長、朱培源學長與陳龍羿學長在實驗上提供寶貴的建議與協助，另外感謝黃彥智同學於同步輻射量測的協助、林俊宇同學協助薄膜成長、吳東引學長、周書楷學長與曾俊斌學弟於光學量測上的協助。感謝實驗室的夥伴們陳學儒同學，王雅卿同學、即將念博士的廖佑廣同學以及人數非常眾多的碩一與剛進入實驗室的學弟妹無論是實驗的協助或是營造實驗室歡樂的氣氛，都讓生活變得更豐富。

最後，要感謝我的家人以及汪佳慧對我的支持與關懷，讓我能夠順利完成學業，在此將這份成就及喜悅獻給我最摯愛的家人。

陳耀宗 於新竹交通大學

西元 2010 年 6 月

利用飛秒光譜檢測具應變鈮錳氧薄膜內

錳離子 $d-d$ 能隙與尼爾溫度之研究

研究生：陳耀宗

指導教授：吳光雄 教授

國立交通大學 電子物理系所

摘要

此論文中，我們利用脈衝雷射鍍膜系統分別於 MgO(100), MgO(111)與 YSZ(111)三種基板上成功地製備沿 c 軸(001)成長的鈮錳氧化物薄膜。並以 X 光繞射儀、四環繞射儀等量測晶格不匹配所對應樣品的晶格結構以及其應變效應。進一步，我們藉由可變波長之飛秒雷射激發-探測系統(OPOP)研究這些磊晶應變效應對鈮錳氧化物錳離子之間 d 軌域躍遷能隙(E_{dd})以及尼爾溫度(T_N)的影響。

Mn³⁺ *d-d* Energy Difference and Néel Temperature

in Strained YMnO₃ Thin Films

Probed by Femtosecond Spectroscopy

Student: Yao-Tsung Chen

Adviser: Kaung-Hsiung Wu

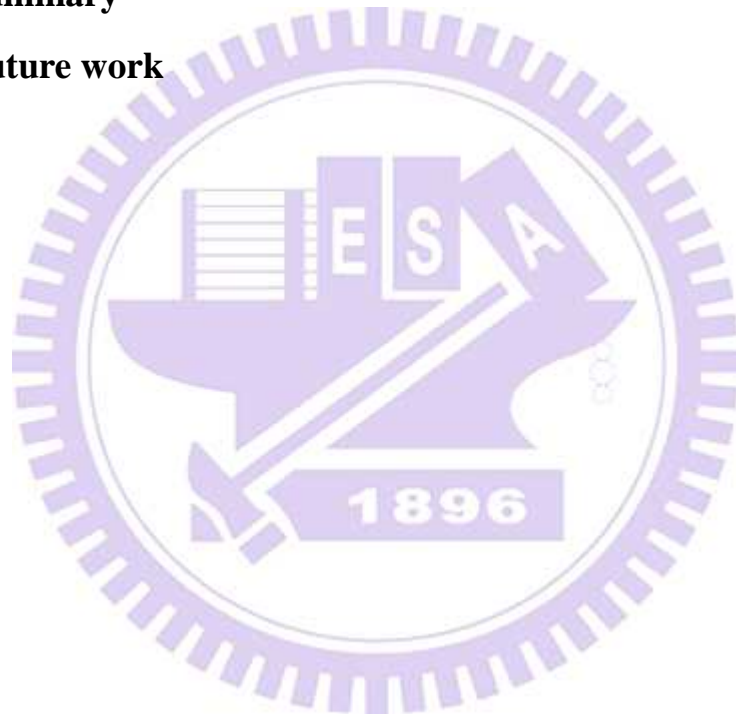
Abstract

In this thesis, we prepared pure (001)-oriented *h*-YMnO₃ thin films on (100)MgO, (111)MgO and (111)YSZ substrates by pulsed laser deposition(PLD), respectively. And we get the crystal structure and strain effect of these thin films by X-ray diffraction and phi-scan. In further, we will show the results of the ultrafast dynamics in these samples probed by the tunable wavelength optical pump-optical probe technique. Especially, the influence of epitaxial strain due to lattice mismatch between the substrate and *h*-YMO films on the magnitude of E_{dd} and Néel temperature (T_N).

Contents

Abstract (in Chinese)	i
Abstract (in English)	ii
Contents	iii
List of Figures	v
List of Tables	ix
List of Equations	ix
Chapter 1 Introduction	
1-1 What's the multiferroics	1
1-2 Hexagonal phase of RMnO₃	3
1-3 Motivation	6
Chapter 2 Sample preparation and basic properties measurement	
2-1 The preparation of <i>h</i>-YMnO₃ films	
2-1-1 Analysis of lattice mismatch	8
2-1-2 Pulse laser deposition (PLD)	9
2-2 The measurement of the physical properties	
2-2-1 X-ray diffraction	10
2-2-2 Φ-scan	14
2-2-3 SQUID	16
Chapter 3 Optical pump-optical probe (OPOP)	
3-1 OPOP background	22
3-2 System of OPOP	24
3-3 Cooling system	26
3-4 Time delay zero point positioning	27
3-5 Experimental methods and process	28

Chapter 4 Experimental Result and Discussion	
4-1 Epitaxial-strain effect on Mn³⁺ <i>d-d</i> energy difference	30
4-1-1 Pump-Probe results (Fix wavelength)	31
4-1-2 Pump-Probe results (Tunable wavelength)	42
4-1-3 $\Delta R/R$ Signal analysis	53
4-2 Epitaxial-strain effect on Néel temperature shift	61
Chapter 5 Summary and future work	
5-1 Summary	69
5-2 Future work	70
References	71



List of figures

- Fig.1-1 Relationship between multiferroic and magnetoelectric materials [2].
- Fig.1-2 *h*-YMO ferroelectric (FE) phase and paraelectric (PE) structure [10].
- Fig.1-3 (a) Side view of *h*-YMnO₃ structure, (b) Top view of *h*-YMnO₃ structure along *c*-axis.
- Fig.2-1 *h*-YMnO₃ thin film thickness (Pulse number: 9KP).
- Fig.2-2 these schematics show the in-plane arrangements between the *h*-YMnO₃ thin films (red line) and substrates (black line). Left hand side shows *h*-YMnO₃/MgO (111); Right hand side shows *h*-YMnO₃/YSZ(111).
- Fig.2-3 The illustration of pulsed laser vacuum deposition system.
- Fig.2-4 XRD patterns of (a) *h*-YMnO₃/MgO(100), (b) *h*-YMnO₃ single crystal, (c) *h*-YMnO₃/MgO(111) and (d) *h*-YMnO₃/YSZ(111) samples.
- Fig.2-5 XRD patterns of the different thickness of *h*-YMnO₃/YSZ(111).
- Fig.2-6 shows the relationship of *c*-axis lattice constant and pulse number.
- Fig.2-7 show Φ -scan result of *h*-YMO/MgO(100) [13].
- Fig.2-8 show Φ -scan result of *h*-YMO/MgO(111).
- Fig.2-9 show Φ scan result of *h*-YMO/YSZ(111).
- Fig.2-10 The growth situation of *h*-YMO/MgO(100). The structure of YMnO₃ is hexagonal, MgO(100) substrate is square.
- Fig.2-11 show magnetization vs temperature (M-T) curves and the reciprocal magnetization vs temperature (1/M-T) for *h*-YMO/MgO(100) with FC and ZFC parallel to the film surface.
- Fig.2-12 show susceptibility vs temperature (χ -T) curves and the inset is reciprocal susceptibility vs temperature (1/ χ -T) for *h*-YMO single crystal I [14].
- Fig.2-13 show magnetization vs temperature (M-T) curves and the reciprocal magnetization vs temperature (1/M-T) for *h*-YMO/MgO(111) with FC and ZFC parallel to the film surface.
- Fig.2-14 show magnetization vs temperature (M-T) curves and the reciprocal magnetization vs temperature (1/M-T) for *h*-YMO/YSZ(111) with FC and ZFC parallel to the film surface.
- Fig. 3-1 The setup of pump-probe spectroscopy. AOM: acousto-optic modulator. P: polarizer. CCD: CCD camera. PD: photodiode. M: multimeter. RF: RF driver. F: function generator. D: delay controller. The solid and dashed lines represent the laser beam path and the dotted lines stand for the electrical signal connection [15].
- Fig. 4-1 The transient reflectivity $\Delta R/R$ curves of *h*-YMnO₃/MgO(100) samples measured at various temperatures.
- Fig. 4-2 The transient reflectivity $\Delta R/R$ curves of *h*-YMnO₃/MgO(100) samples

measured at various temperatures (Part of Fig.4-1 data).

Fig.4-3 The transient reflectivity $\Delta R/R$ curves of h -YMnO₃ single crystal samples measured at various temperatures.

Fig.4-4 The transient reflectivity $\Delta R/R$ curves of h -YMnO₃ single crystal samples measured at various temperatures (Part of Fig.4-3 data).

Fig.4-5 The transient reflectivity $\Delta R/R$ curves of h -YMnO₃/MgO(111) samples measured at various temperatures.

Fig.4-6 The transient reflectivity $\Delta R/R$ curves of h -YMnO₃/MgO(111) samples measured at various temperatures (Part of Fig.4-5 data).

Fig.4-7 The transient reflectivity $\Delta R/R$ curves of h -YMnO₃/YSZ(111) samples measured at various temperatures.

Fig.4-8 The transient reflectivity $\Delta R/R$ curves of h -YMnO₃/YSZ(111) samples measured at various temperatures (Part of Fig.4-7 data).

Fig.4-9 (a) The amplitude of $\Delta R/R$ as a function of temperature at 800nm taken from Fig.4-8 at zero delay time. (b) Energy difference of the Mn³⁺ energy levels in the local environment MnO₅ for photon energy above and below E_{dd}. (c) Orbital-resolved densities of states of Mn 3d orbitals and the in-plane O 2p orbital for YMnO₃ [15].

Fig.4-10 it illustrates the splitting of the Mn³⁺ energy levels in the local environment MnO₅.

Fig.4-11 Three primary features of dynamics in the $\Delta R/R$ curves.

Fig.4-12 The transient reflectivity $\Delta R/R$ curves of h -YMnO₃/YSZ(111) samples measured with the same pump and probe beam wavelength(815nm) at various temperatures.

Fig.4-13 The transient reflectivity $\Delta R/R$ curves of h -YMnO₃/YSZ(111) samples measured with the same pump and probe beam wavelength(800nm) at various temperatures.

Fig.4-14 The transient reflectivity $\Delta R/R$ curves of h -YMnO₃/YSZ(111) samples measured with the same pump and probe beam wavelength(785nm) at various temperatures.

Fig.4-15 The transient reflectivity $\Delta R/R$ curves of h -YMnO₃/YSZ(111) samples measured with the same pump and probe beam wavelength(777nm) at various temperatures.

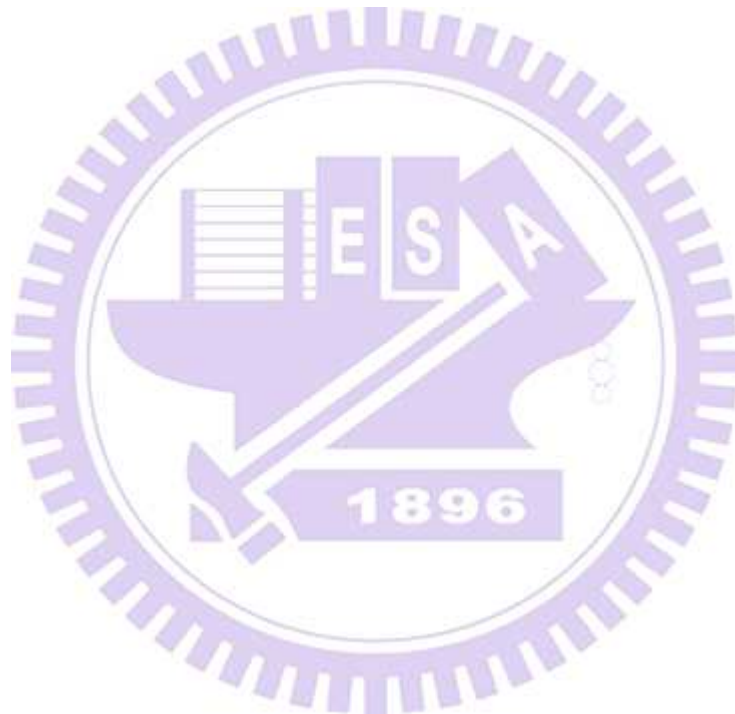
Fig.4-16 The transient reflectivity $\Delta R/R$ curves of h -YMnO₃/YSZ(111) samples measured with the same pump and probe beam wavelength(770nm) at various temperatures.

Fig.4-17 The transient reflectivity $\Delta R/R$ curves of h -YMnO₃/YSZ(111) samples measured with the same pump and probe beam wavelength(755nm) at various temperatures.

- Fig. 4-18 Normalized amplitude of $\Delta R/R$ as a function of temperature of h -YMnO₃/YSZ(111) at various wavelengths (λ) at zero delay time.
- Fig. 4-19 Normalized amplitude of $\Delta R/R$ as a function of temperature of h -YMnO₃ single crystal at various wavelengths (λ) at zero delay time.
- Fig.4-20 The energy gap E_{dd} as a function of temperature T(K). E_{dd} is estimated from the different wavelengths (755,770,785,800,815nm). The black line is the T_N (Néel temperature) for the YMnO₃ single crystal to be a standard sample.
- Fig.4-21 Optical conductivity spectra of hexagonal HoMnO₃, DyMnO₃, TbMnO₃, and GdMnO₃ thin films. For clarity, the spectra have been plotted with offsets of $1250 \Omega^{-1} \text{ cm}^{-1}$ vertically between each curve, and the base line for each curve is shown by the horizontal dashed line. The arrows in the TbMnO₃ spectrum indicate the three peak positions where optical absorption occurs. The vertical dotted line indicates the first optical transition peak position of YMnO₃ [15].
- Fig.4-22 Schematic representation of the crystal field splitting changes due to flattening of the MnO₅ triangular bipyramid. The flattening occurs due to the increase of the rare earth ionic radius with the fixed c -axis lattice constant. As the flattening occurs, due to the orbital symmetries, the $d_{3z^2-r^2}$ orbital will shift to higher energy, whereas the d_{xy} and $d_{x^2-y^2}$ orbitals stay the same [15].
- Fig.4-23 the lattice constant ratio (\bar{ac} , filled symbols) and the in-plane lattice constant (a , empty symbols) of bulk hexagonal RMnO₃ (<circles, R =Lu, Yb, Tm, Er, Y, and Ho [24]>, and film hexagonal RMnO₃ (squares, R =Dy, Tb, and Gd).
- Fig.4-24 shows the fitting of h -YMnO₃. There are fast, slow1, slow2 and oscillation components. When $T < T_{SO}$, we added a slow 2 component for magnetization.
- Fig.4-25 Amplitude of slow 2 component as various temperatures.
- Fig.4-26 Strain pulse model (Interference between surface and strain layer).
- Fig.4-27 Coherent acoustic phonon mode measured at 140 K in (a) and at various temperatures in (b).
- Fig.4-28 The amplitude (A_0) of coherent acoustic phonon mode at various temperatures.
- Fig.4-29 The period of coherent acoustic phonon mode at various temperatures
- Fig.4-30 The energy gap E_{dd} as a function of T (K) for h -YMnO₃/MgO(100).
- Fig.4-31 The slope (dE_{dd}/dT) as a function of T (K) for h -YMnO₃/MgO(100).
- Fig.4-32 The energy gap E_{dd} as a function of T (K) for h -YMnO₃/Single Crystal.
- Fig.4-33 The slope (dE_{dd}/dT) as a function of T (K) for h -YMnO₃/ Single Crystal.
- Fig.4-34 The energy gap E_{dd} as a function of T (K) for h -YMnO₃/Single Crystal.
- Fig.4-35 The slope (dE_{dd}/dT) as a function of T (K) for h -YMnO₃/MgO(111).
- Fig.4-36 The energy gap E_{dd} as a function of T (K) for h -YMnO₃/YSZ(111).
- Fig.4-37 The slope (dE_{dd}/dT) as a function of T (K) for h -YMnO₃/YSZ(111).
- Fig.4-38 Temperature dependence of the optical transition at ~1.7 eV.(a)Temperature dependence of the peak positions normalized to the peak position at T_N (w_n) as a

function of the normalized temperature $T_{Nn} (=T/T_N)$. Temperature values of 56, 70, 60, 75, and 90 K were used as T_N and the energy values of 1.9725, 1.77, 1.785, 1.7711, and 1.7249 eV were used as the peak energy values at T_N for R=Gd, Tb, Dy, Ho, and Lu, respectively. (b) Absolute value of normalized peak position differentiated to normalized temperature [25].

Fig.4-39 Temperature dependence of the peak energy (Blue circle) of the 1.7 eV feature and its spectral weight (Red square) [26]



List of tables

Table 2-1 The substrate temperature and oxygen pressure.

Table 2-2 The lattice mismatch between substrate and h -YMnO₃ thin film.

Table 2-3 c-axis lattice constants, a/c ratio and ratio of out-of-plane.

Table 2-4 c-axis lattice constant of different thickness of h -YMnO₃/YSZ(111) thin films.

Table 4-1 The parameter of a/c ratio, c-axis lattice constant (Å), T(K, $\Delta R/R=0$) at 1.55eV, and E_{ad} at 200K of h -YMO/MgO(100), h -YMO/single crystal, h -YMO/MgO(111) and h -YMO/YSZ(111), respectively.

Table 4-2 The parameter of T (K), $\Delta R/R=0$ at 1.55eV and 1.58eV of h -YMO/MgO(100), h -YMO/single crystal, h -YMO/MgO(111) and h -YMO/YSZ(111), respectively.



List of equations

Eq. 2-1 Bragg's law

Eq. 2-2 (hkl) planes the lattice constants for hexagonal structure

Eq. 3-1, $I_o(t)$ is DC voltage signal that it stand for the intensity of reflectivity. And $\Delta I(t)$ is stand for the change (ΔR) of reflectivity.

Eq. 4-1 The formula of heating effect from reference [18]

Chapter 1 Introduction

1-1 What's the multiferroic?

Multiferroics have been defined as materials that exhibit more than one primary ferroic order parameter simultaneously (i.e. in a single phase) [1]. And ferroics as two or more states exist and can be shifted by field [2].

The four basic primary ferroic order parameters are ferromagnetism, ferroelectricity, ferroelasticity and ferrotoroidicity, the latter still being under debate.

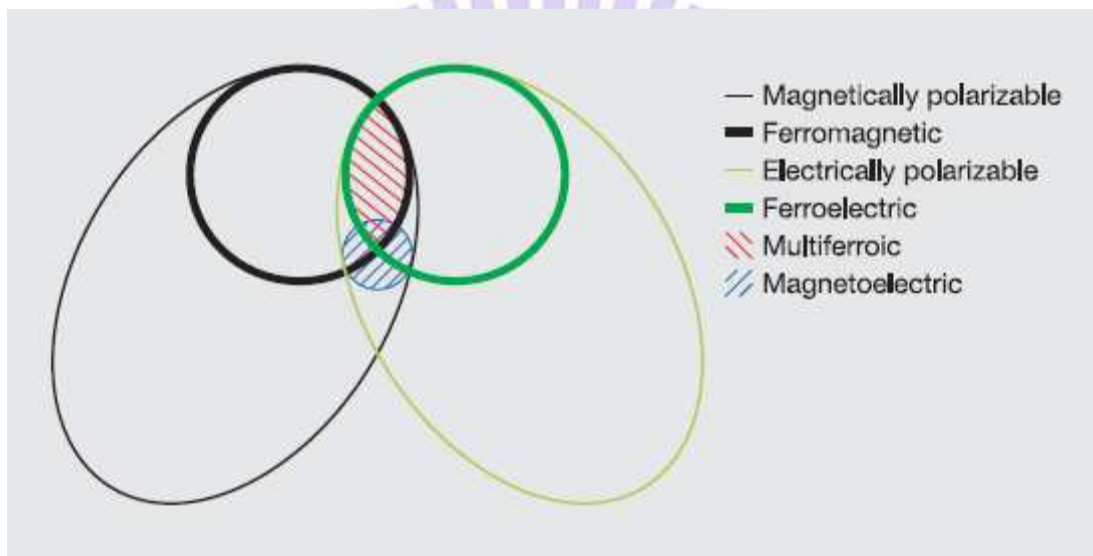


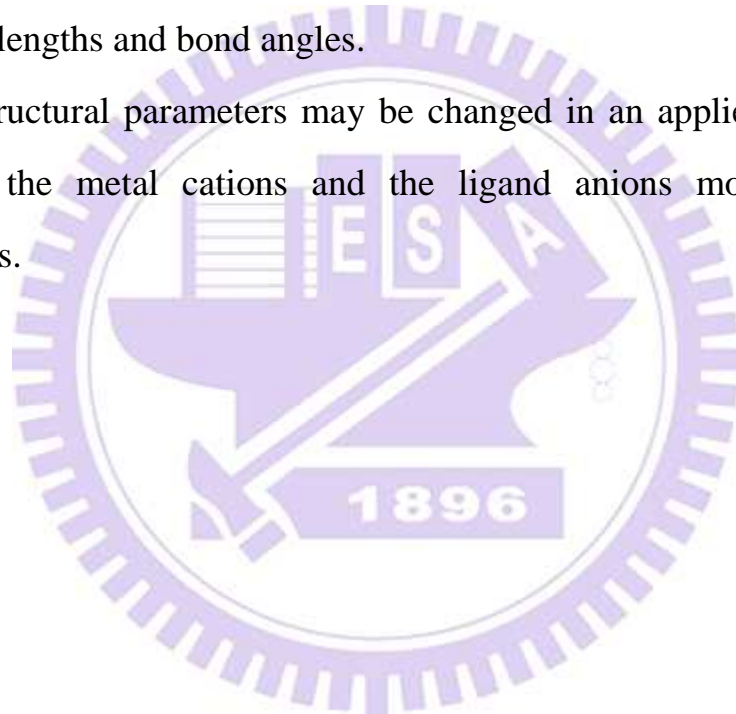
Fig.1-1 Relationship between multiferroic and magnetoelectric materials [2].

Ferromagnets (ferroelectrics) form a subset of magnetically (electrically) polarizable materials such as paramagnets and antiferromagnets (paraelectrics and antiferroelectrics). The intersection (red hatching) represents materials that are multiferroic. Magnetoelectric coupling (blue hatching) is an independent phenomenon that can, but need not, arise in any of the materials that are both magnetically and electrically polarizable. In practice, it is likely to arise in all such materials, either directly or via strain.

Multiferroics exhibit at least two types of order: polarization, magnetization,

or deformation. In a multiferroic crystal with both electric and magnetic order, interdependence between the two orders may exist: An applied electric field induces a linear change of magnetization and an applied magnetic field induces a linear change of polarization. This kind of coupling is called a magnetoelectric (ME) effect and was predicted 1894 and observed first in 1960[3]. The microscopic origins of the ME effect is twofold:

- (1) The magnetic ordering is driven by (super)exchange interactions whose strength depends sensitively on the overlap of magnetic orbitals, that is, on bond lengths and bond angles.
- (2) These structural parameters may be changed in an applied electric field, because the metal cations and the ligand anions move in opposite directions.



1-2 Hexagonal Phase of RMnO_3

A major series that show ferroelectricity along with magnetic ordering consist of materials of the general formula RMnO_3 ($R = \text{Y, Lu, Ho, Er, Tm, Sc, Yb}$ etc.). Base on the structural point, magnetic ordering occurs in both hexagonal (space group $P6_3\text{cm}$) and orthorhombic (space group Pnma) manganites, whereas ferroelectric ordering occurs only in hexagonal phase which is noncentrosymmetric. Hexagonal RMnO_3 compounds have antiferromagnetic ordering with the Néel temperature $T_N < 70\text{-}130$ K, and ferroelectric ordering at much higher temperature $T_E < 600\text{-}900\text{K}$ [4-6].

The hexagonal YMnO_3 exhibit the ferroelectric transition at high temperature, $T_C \sim 910\text{K}$ [7] and become A-type antiferromagnetic below the Neél temperature in single crystalline, $T_N \sim 70\text{K}$ [8,9]. Above 910K, the paraelectric (PE) phase has the hexagonal structure with $P6_3/\text{mmc}$ space group symmetry, and the ferroelectric (FE) phase has the hexagonal structure in $P6_3\text{cm}$ symmetry.

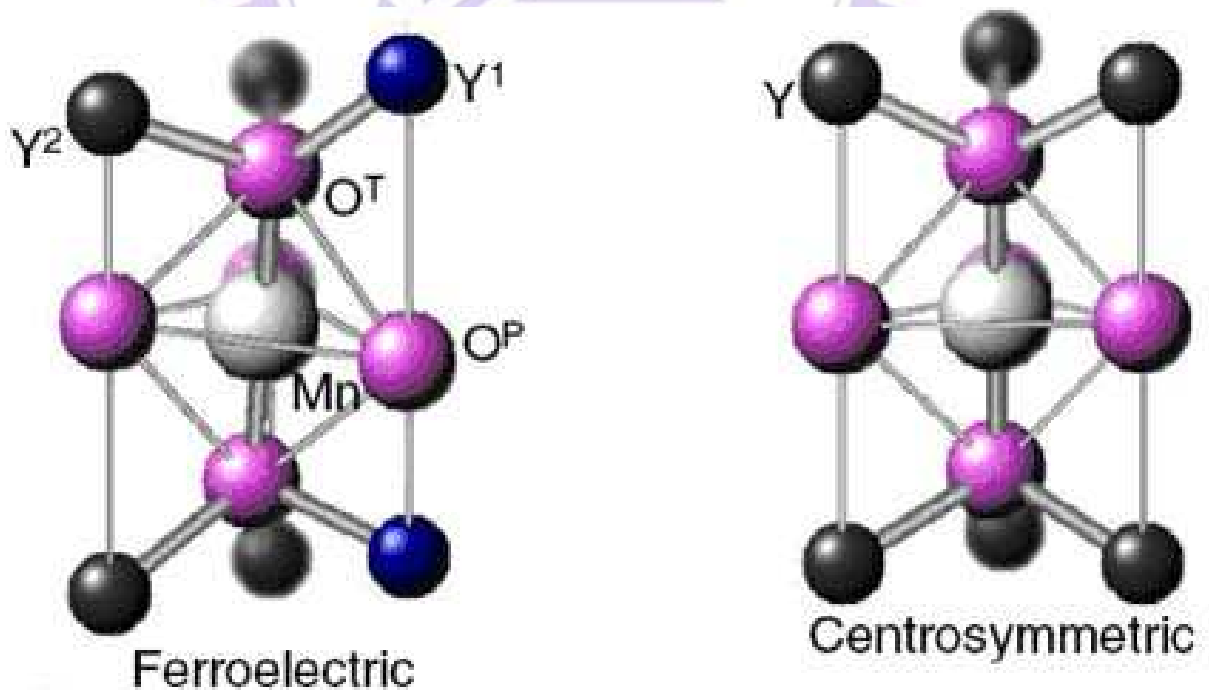
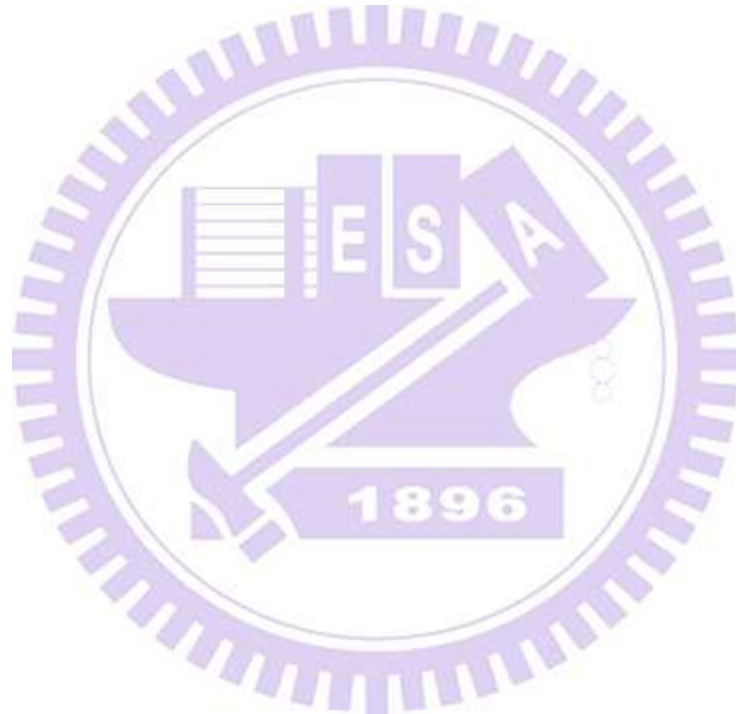


Fig.1-2 h -YMO ferroelectric (FE) phase and paraelectric (PE) structure [10].

In h - YMnO_3 (see Fig.1-3), each Mn ion is surrounded by five oxygen ions.

These MnO_5 blocks are connected two dimensionally through their corners and the triangular lattice of Mn^{3+} ions with $S=2$ are formed. There are two magnetic transition temperature ($T_N=70\text{K}$ and $T_{SR}=40\text{K}$). The first temperature, Mn^{3+} ions interact antiferromagnetically below $T_N=70\text{K}$ and lead to geometrical frustration (GF) in the system [10]. The second temperature is due to Mn^{3+} ions spin reorientation (SR).

Moreover, the ferroelectric polarization is caused by MnO_5 blocks tilt and leading to displacement of Y^{3+} ion along c-axis, the value is about $5.6\mu\text{C}/\text{cm}^2$.



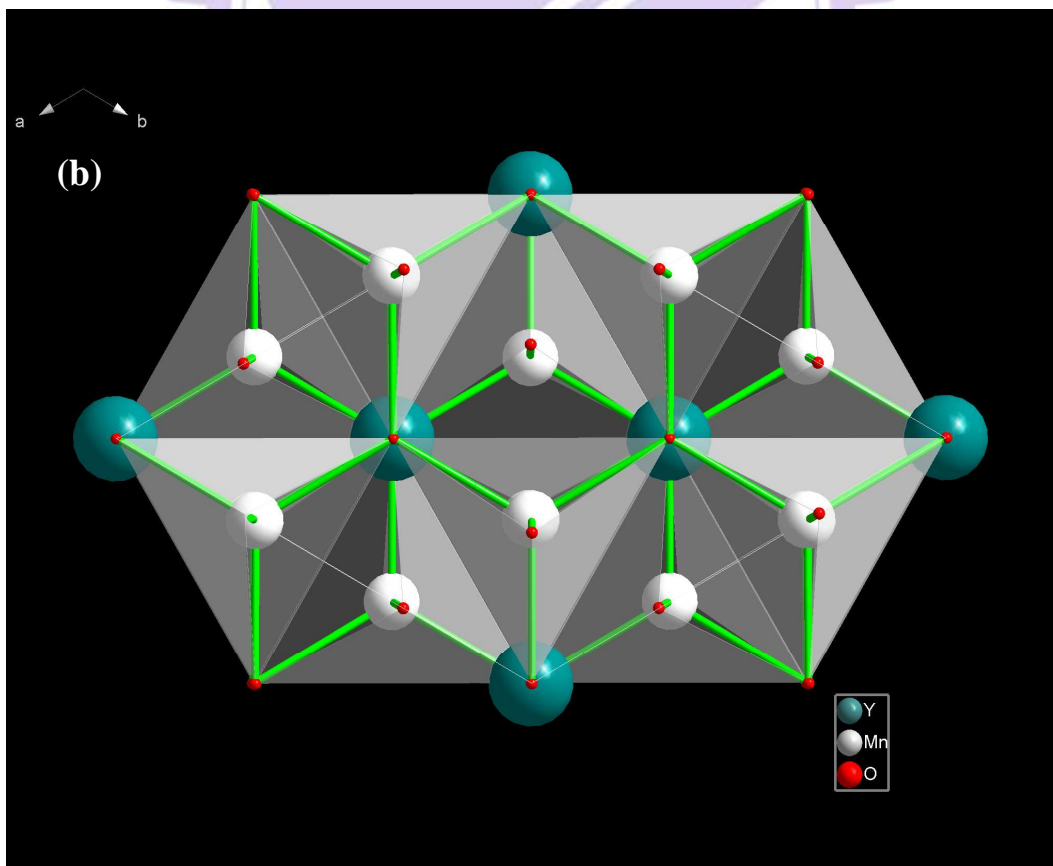
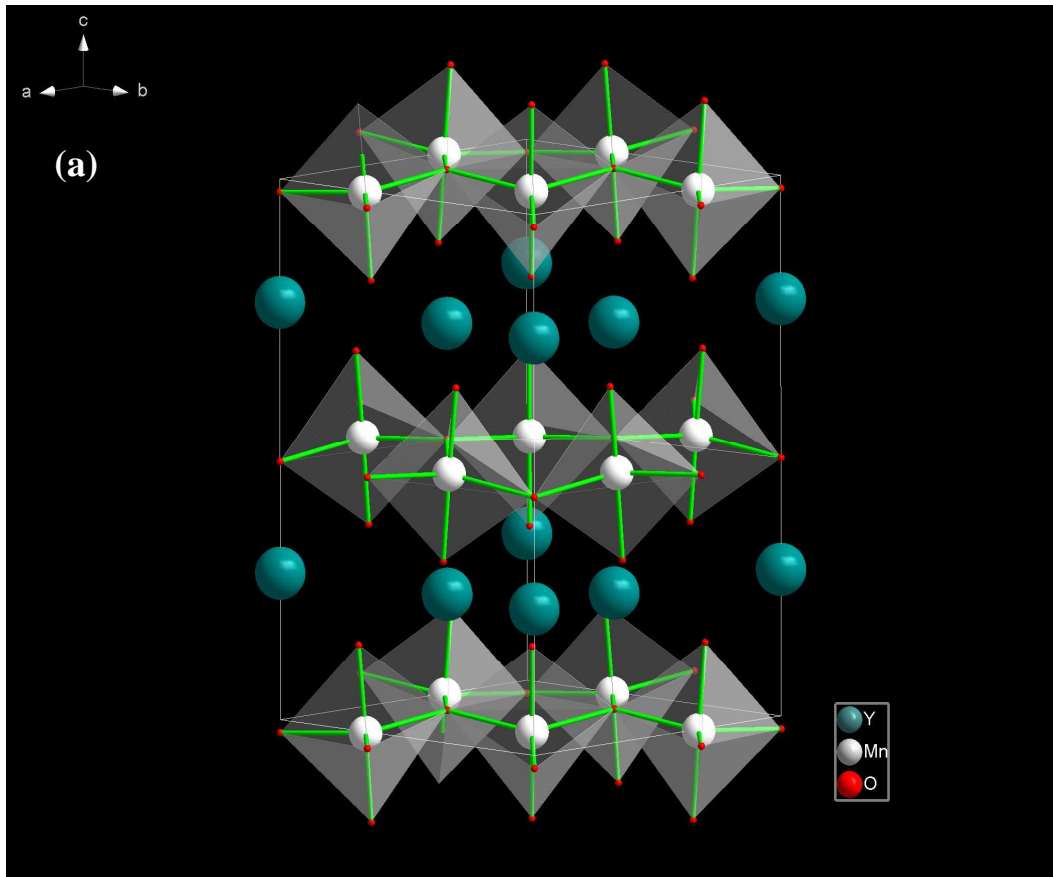


Fig.1-3 (a) Side view of h -YMnO₃ structure, (b) Top view of h -YMnO₃ structure along c -axis.

1-3 Motivation

The hexagonal multiferroic manganites have attracted much scientific attention in recent years because they exhibit a wide variety of exotic physical properties, include the origins of ferroelectric ordering and magnetic frustration, the significant coupling between the magnetic and electric order parameters (magnetoelectric ME effect), and the anomalous dielectric constant and blueshift of the absorption peak (~ 1.7 eV) in the optical spectra near the Néel temperature (T_N).

Recently ultrafast optical pump-optical probe (OPOP) spectroscopy provides a powerful tool to investigate the strongly correlated electron materials since the relative contributions of electron, phonon and spin dynamics in these materials can be directly resolved temporally. We have studied the ultrafast dynamics in h -HoMnO₃ single crystal by the OPOP technique previously [11]. The temperature dependences of on-site Mn d - d transition energy $E_{dd}(T)$, the anomalous blueshift near T_N and how they related to the magnetic ordering and the magnetization dynamics have been revealed and discussed in the experiment. An open question that is of current interest is **whether the above properties (and thus the ME effect) can be changed/controlled by introducing the strain into the system [12].**

In this work, we prepared pure (001)-oriented h -YMnO₃ thin films on respectively. We will show the results of the ultrafast dynamics in these samples probed by the OPOP technique, especially. The influence of strain due to lattice mismatch between the substrate and h -YMnO₃ films on the magnitude of E_{dd} . We found that E_{dd} change slightly due to the small change of the ratio of lattice constants a/c .

Chapter 2 Sample preparation and basic properties measurement

2-1 The preparation of YMnO_3 films

h - YMnO_3 thin films were successfully grown on MgO (100), MgO (111), and Y-stabilized ZrO_2 , YSZ (111) substrates by pulse laser deposition (PLD). Using a KrF excimer laser (wavelength 248 nm and pulse duration about 30 ns) operating at a repetition rate of 5 Hz, pulse number 9K and with an energy density around $3\text{-}5 \text{ J} \cdot \text{cm}^{-2}$. The substrate temperature and oxygen pressure are show in Table 2-1.

	MgO(100)	MgO(111)	YSZ(111)
Temperature ($^{\circ}\text{C}$)	860	860	880
Oxygen pressure (Torr)	0.003	0.3	0.1

Table 2-1 the substrate temperature and oxygen pressure

The film thickness (pulse number: 9KP) was about 175nm as determined by scanning electron microscope (SEM). Show in Fig. 2-1

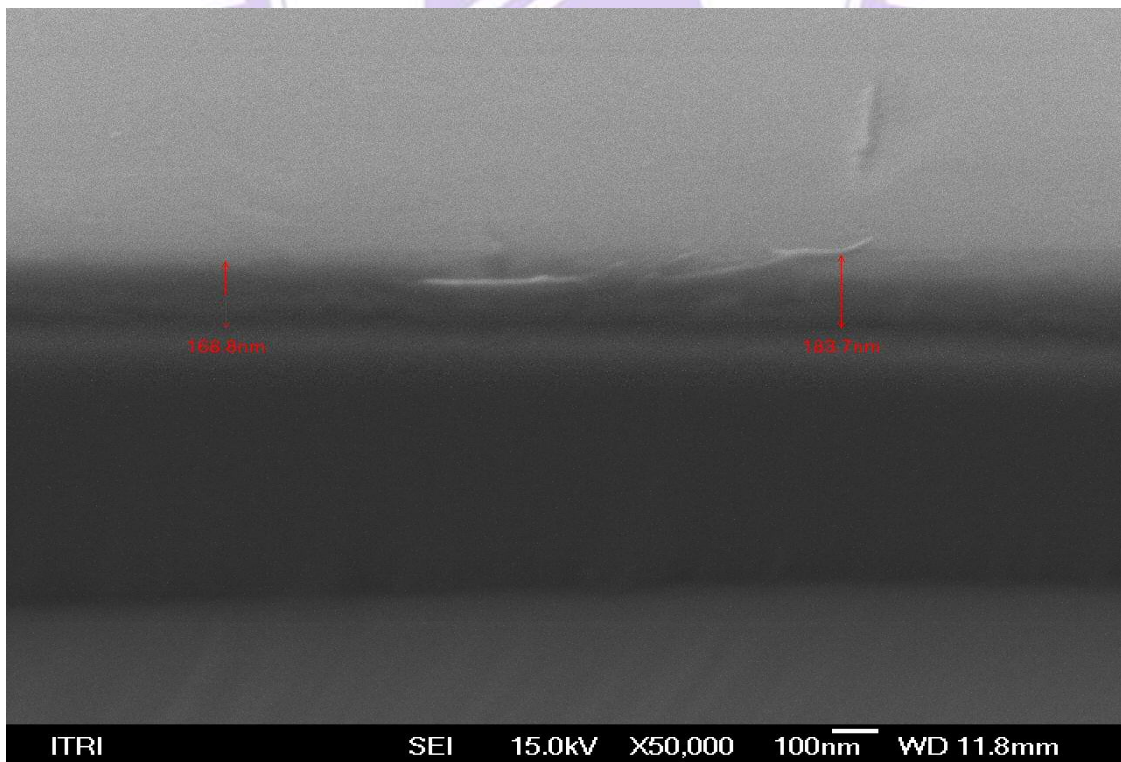


Fig. 2-1 h - YMnO_3 thin film thickness (Pulse number: 9KP).

2-1-1 Analysis of lattice mismatch

	a(Å)	b(Å)	c(Å)	In-plane lattice constant(Å)	In-plane mismatch(%)
<i>h</i> -YMnO ₃	6.136	6.136	11.40	6.136(Single Crystal)	0.00
MgO(100)	4.236	4.236	4.236	5.990/MgO(111)	-2.38
YSZ(100)	5.147	5.147	5.147	6.304/YSZ(111)	+2.74

Table 2-2 the lattice mismatch between substrate and *h*-YMnO₃ thin film.

According to the above comparison, MgO(100), MgO(111) and YSZ(111) substrates have the least mismatch, these substrates are suitable to deposit *h*-YMnO₃ thin films. We predict MgO(111) will get rise to compressive strain with the mismatch value (-2.38%) while YSZ(111) will have the tensile strain with mismatch value (+2.74%).

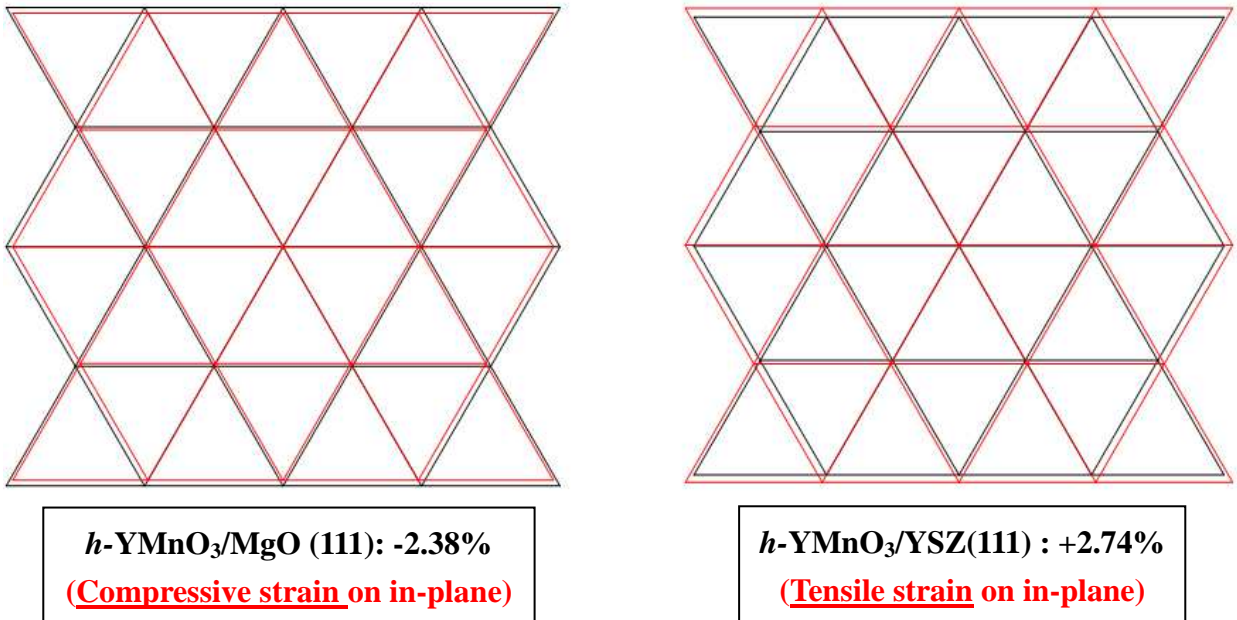


Fig. 2-2 These schematics show the in-plane arrangements between the *h*-YMnO₃ thin films (red line) and substrates (black line). Left hand side shows *h*-YMnO₃/MgO (111); Right hand side shows *h*-YMnO₃/YSZ(111).

2-1-2 Pulse laser deposition (PLD)

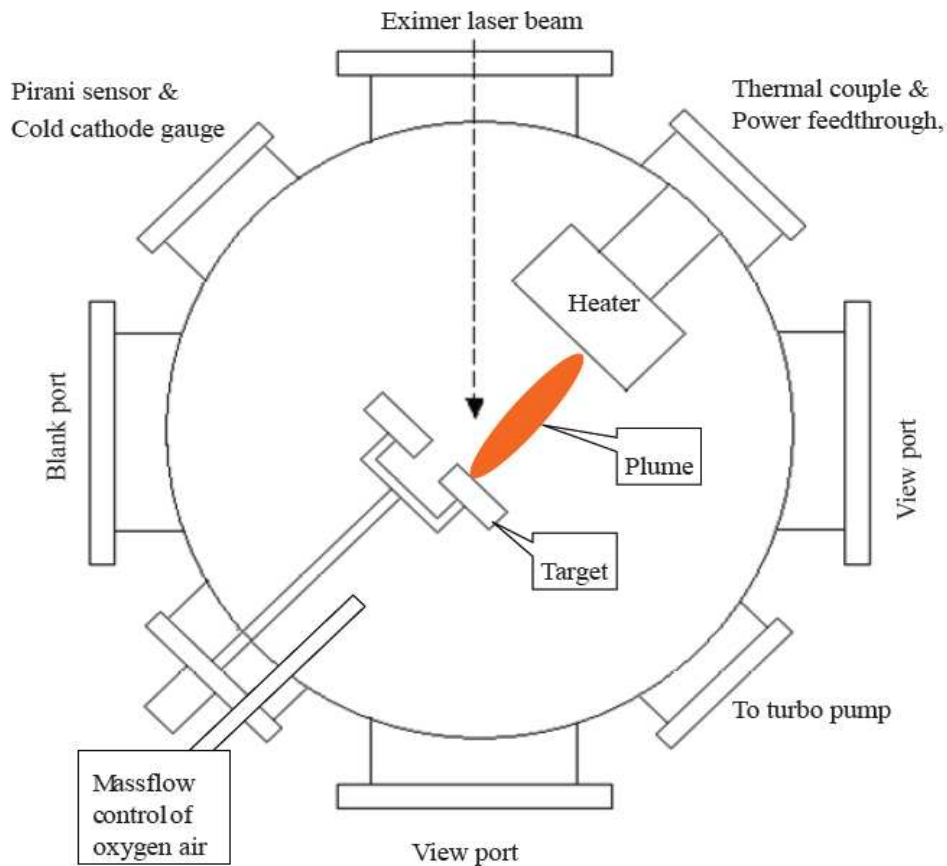


Fig.2-3 the illustration of pulsed laser vacuum deposition system.

Pulse laser deposition is one of technology of depositing thin films. Fig.2-3 is the pulse laser deposition (PLD) system. Before the deposition, we need to clean the substrate by acetone, methanol and D. I. Water in order to getting superior quality thin films. Using the mechanism and turbo pump to decrease the vacuum pressure below 1×10^{-6} torr. Then we start to heat the substrate temperature, filling oxygen gas into the chamber.

Next, we guide the laser beam to the YMnO_3 target and rotate the target. When pulse laser beam hit the target, it will form plasma to deposit on the substrate. After the deposition, close the heater and E. M. Valve, then filling a great deal of oxygen gas to do quench process.

2-2 The measurement of the physical properties

2-2-1 X-ray diffraction

The structure of YMnO_3 thin films and single crystal were determined by X-ray diffraction (XRD). As Fig.2-4 show, we successfully growth only c -axis direction peaks of YMnO_3 , except for the substrate peak.

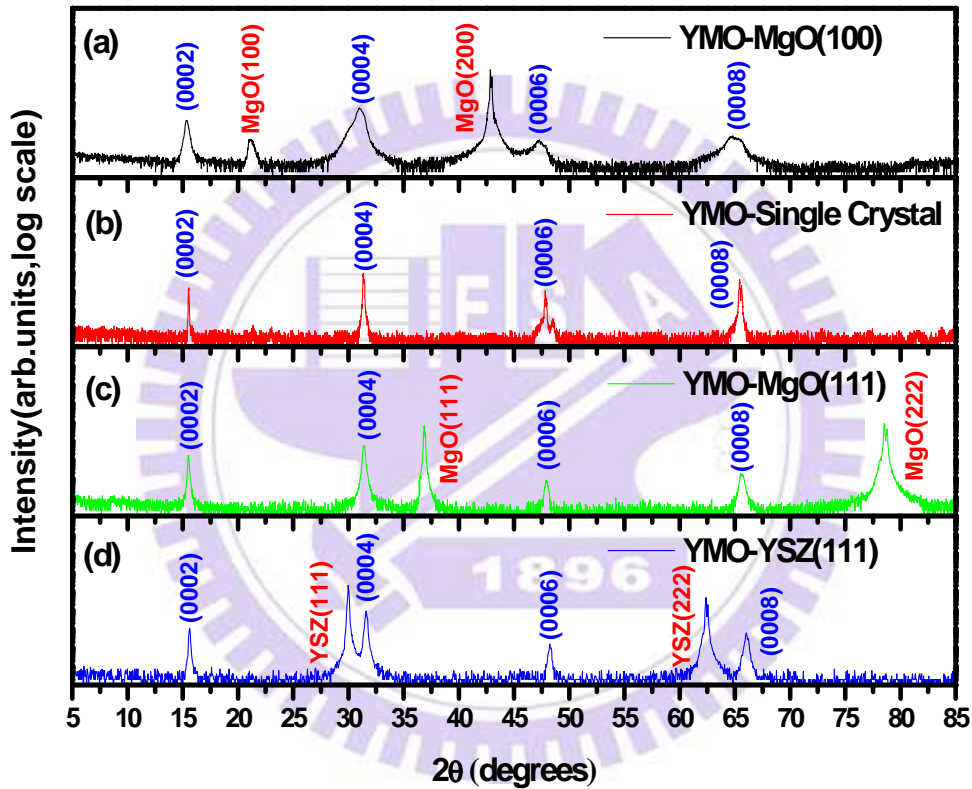


Fig.2-4 XRD patterns of (a) $h\text{-YMnO}_3/\text{MgO}(100)$, (b) $h\text{-YMnO}_3$ single crystal, (c) $h\text{-YMnO}_3/\text{MgO}(111)$ and (d) $h\text{-YMnO}_3/\text{YSZ}(111)$ samples

The c -axis lattice constants of YMnO_3 thin films were calculated according to Bragg's law and (hkl) planes the lattice constants for hexagonal structure (Eq. 2-1 and Eq. 2-2):

$$2 d_{hkl} \sin \theta = n \lambda$$

Eq. 2-1

Where

$$\frac{1}{d_{hkl}} = \frac{4}{3} \left(\frac{h^2 + hk + k^2}{a^2} \right) + \frac{l^2}{c^2} \quad \text{Eq. 2-2}$$

Using above formula, Table 2-3 show the c-axis lattice constants calculated from the position of (0004) peak for YMO-MgO(100), YMO-Single Crystal, YMO-MgO(111) and YMO-YSZ(111) are 11.440Å, 11.404 Å, 11.387Å and 11.319Å, respectively. Moreover, *a/c* ratio for YMO-Single Crystal, YMO-MgO(111) and YMO-YSZ(111) are 0.538, 0.543 and 0.548, respectively. In YMO-MgO(100) thin film, the observed tensile strain along the c-axis is probably resulted from the compressive stress in the film plane from the mismatch of the YMnO₃ epilayer respect to the MgO(100) substrate. On the contrary, the compressive strain along the *c*-axis appeared in both films (YMO-MgO(111) and YMO-YSZ(111)).

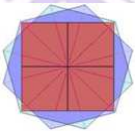
Sample	A	B	C	D
	YMO-MgO(100)	YMO-Single Crystal	YMO-MgO(111)	YMO-YSZ(111)
<i>a/c</i>		0.538	0.543	0.548
<i>c</i> (Å)	11.440	11.404	11.387	11.319
Ratio of out-of-plane (%)	+0.316	0.000	-0.149	-0.745

Table 2-3 *c*-axis lattice constants, *a/c* ratio and ratio of out-of-plane.

Except for using the mismatch between film and substrate, we also control the thickness of *h*-YMnO₃ thin film. The different thickness thin film will suffer the different strain effect. Fig.2-5 shows the XRD patterns of different thickness from 9KP to 1.5KP of *h*-YMnO₃.

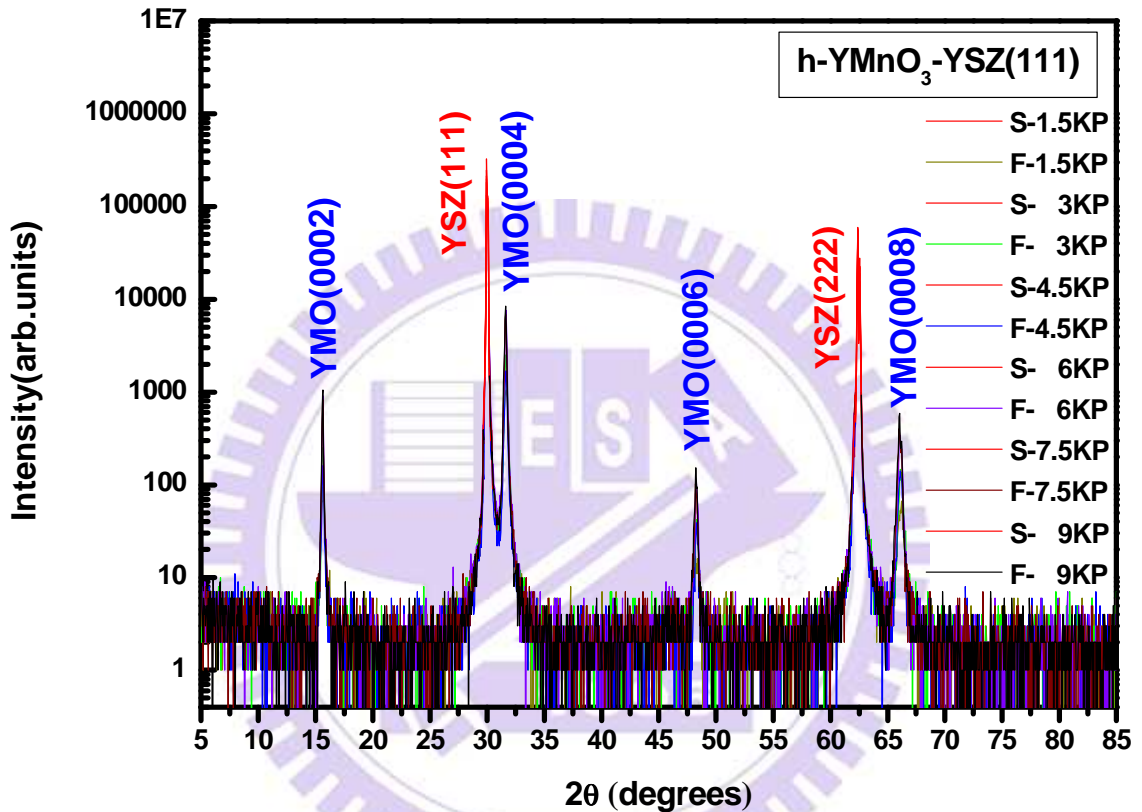


Fig.2-5 XRD patterns of the different thickness of *h*-YMnO₃/YSZ(111).

Fig.2-6 shows the relationship of *c*-axis lattice constant and pulse number. When the pulse number decrease from 9KP to 1.5KP, *c*-axis lattice constant become smaller from 11.3193 Å to 11.2969 Å (~0.0224 Å), ratio of out-of-plane change from -0.739% to -0.936% (~0.2%).

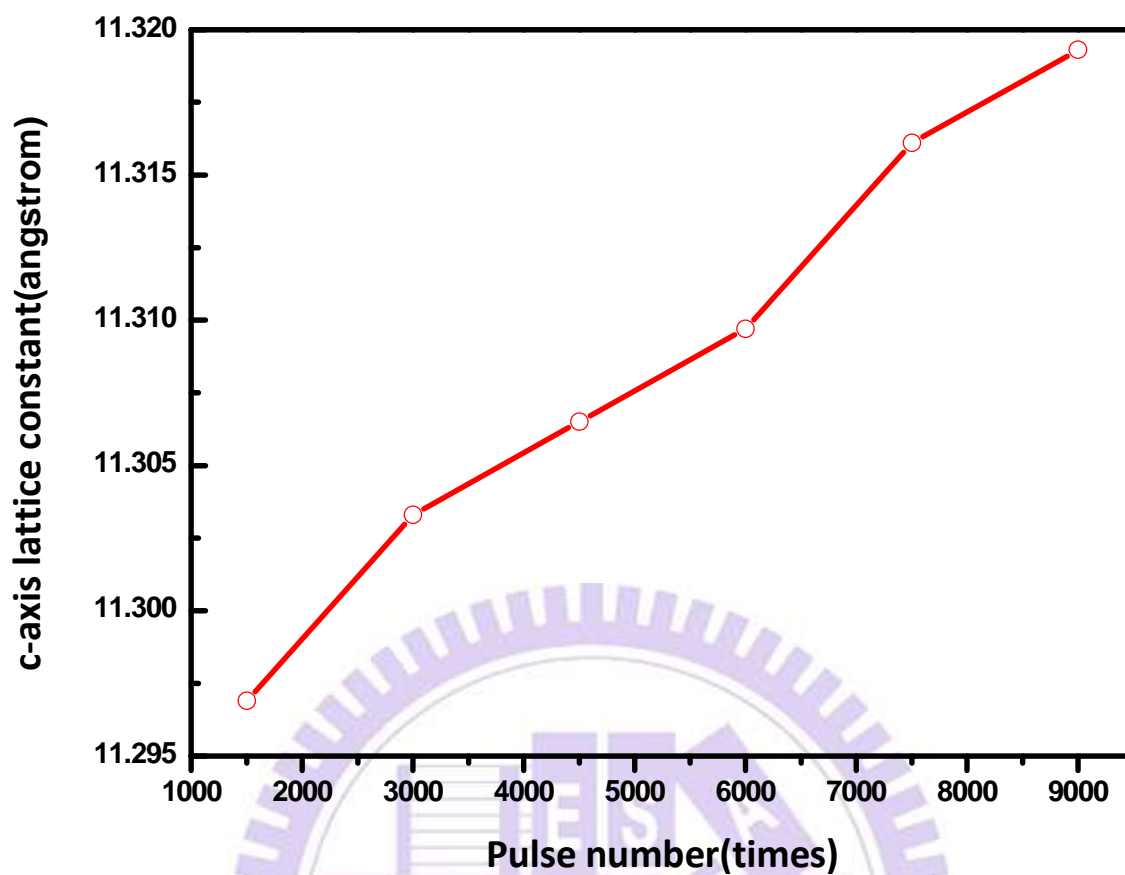


Fig.2-6 shows the relationship of c-axis lattice constant and pulse number.

<i>h</i> -YMnO ₃ /YSZ(111)	2θ (0004)	c(Å)	Ratio of out-of-plane change (%)	
Pulse number	9000	31.60°	11.3193	-0.739
	7500	31.62°	11.3161	-0.767
	6000	31.64°	11.3097	-0.823
	4500	31.65°	11.3065	-0.851
	3000	31.66°	11.3033	-0.880
	1500	31.68°	11.2969	-0.936

Table 2-4 c-axis lattice constant of different thickness of *h*-YMnO₃/YSZ(111) thin films.

2-2-2 Φ -Scan

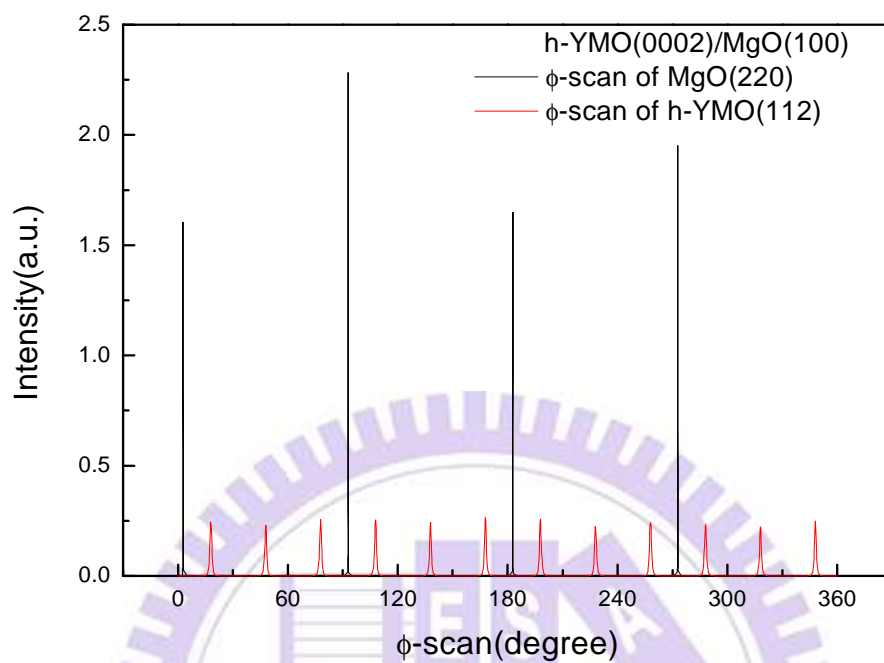


Fig.2-7 show Φ -scan result of *h*-YMO/MgO(100) [13]

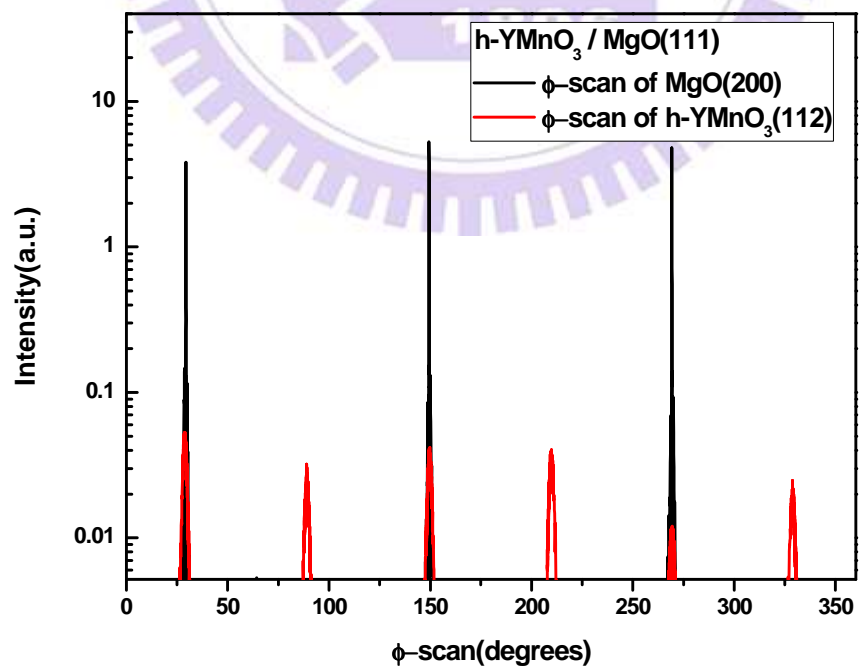


Fig.2-8 show Φ -scan result of *h*-YMO/MgO(111)

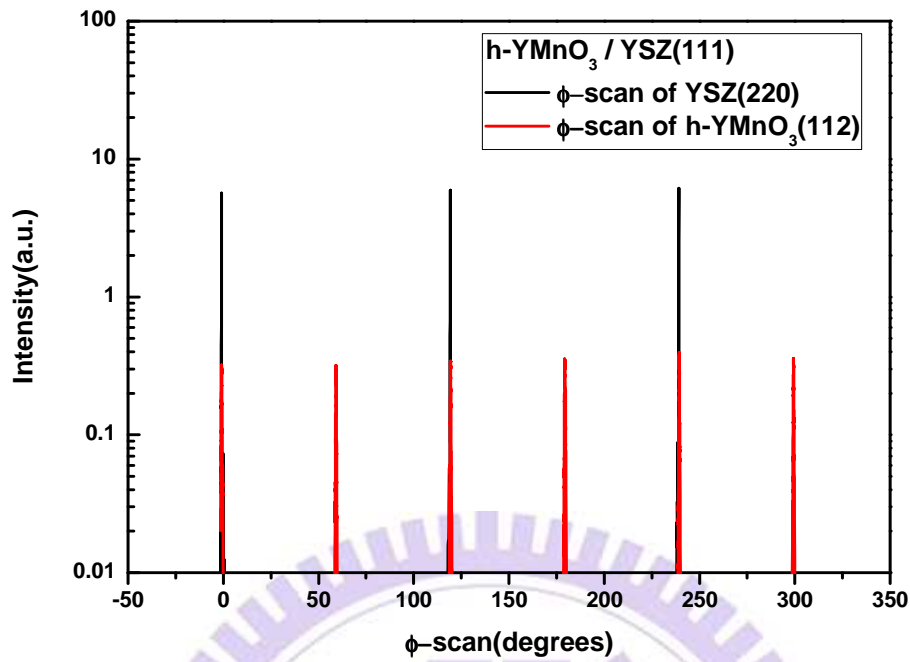


Fig.2-9 show Φ scan result of *h*-YMO/YSZ(111).

From the Φ -scan results, it shows the epitaxial relationship between film and substrate. Moreover, we can also know the orientation characteristics. *h*-YMO/MgO(111) and *h*-YMO/YSZ(111) are six-fold symmetry, but *h*-YMO/MgO(100) is twelve-fold symmetry. Hence, the YMnO_3 growth on MgO(100) substrate maybe along MgO(011) or MgO(0-11) direction. It's show in Fig.2-10

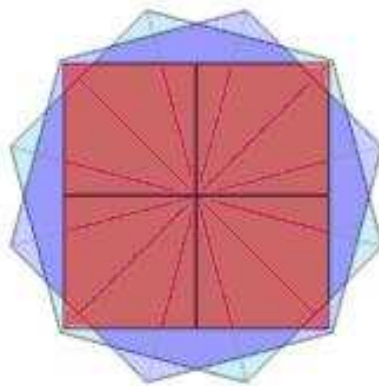


Fig.2-10 The growth situation of *h*-YMO/MgO(100). The structure of YMnO_3 is hexagonal, MgO(100) substrate is square.

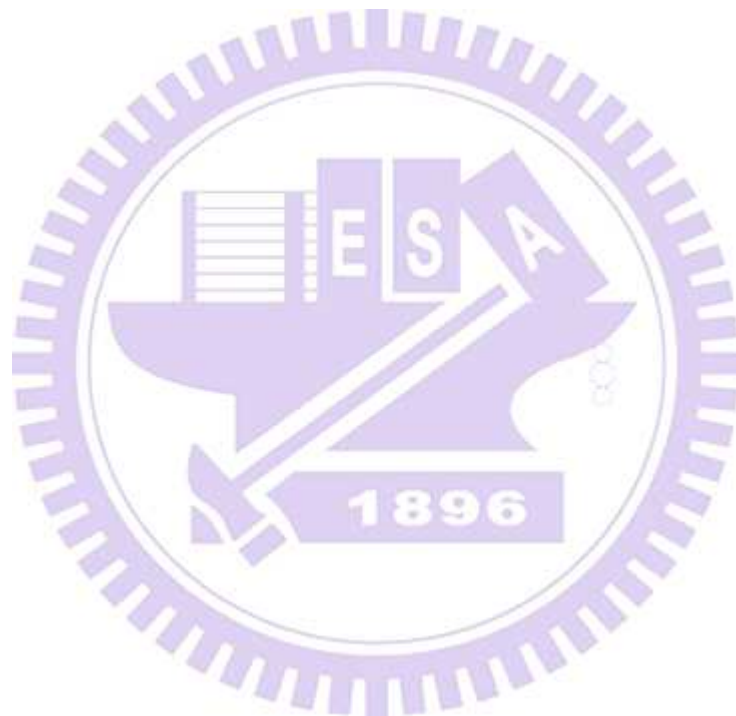
2-2-3 SQUID

The temperature dependent magnetization ($M(T)$) along various crystalline axes was measured in a Quantum Design® superconducting quantum interference device (SQUID) with a small applied magnetic field parallel to the in-plane (perpendicular to the c -axis) to delineate the possible magnetism anisotropy in this material.

Temperature dependent magnetization ($M(T)$) showed the magnetic behavior of the h -YMO/MgO(100), h -YMO/MgO(111), h -YMO/YSZ (111) thin films and h -YMO single crystal. All the thin films are collected with an applied field 500 Oe. Single crystal was measured with applied field 5000Oe [14]. Both the zero field cool (ZFC) and field cool (FC) schemes were measured in Fig.2-11, Fig.2-13 and 2-14.

There are two magnetic phase transitions (around $T_N=70\text{K}$ and $T_{SR}=40\text{K}$, respectively) that might be regarded as the intrinsic Néel temperature and a super spin-glass-like (SSG) transition associated with disorder-coupled spin reorientation behavior. But in most of cases, we just observe the Néel temperature, spin-glass-like (SSG) transition can't if it's less disorder in sample. Fig.2-11, Fig.2-12 and Fig.2-14 show magnetization vs temperature (M - T) curves and the reciprocal magnetization vs temperature ($1/M$ - T) for h -YMO/MgO(100), h -YMO/MgO(111), and h -YMO/YSZ(111) thin films with FC and ZFC parallel to the film surface. Fig.2-13 shows the susceptibility vs temperature (χ - T) of h -YMO single crystal [14]. The reciprocal magnetization vs temperature ($1/M$ - T) show the Néel temperature of h -YMO/MgO(100), h -YMO single crystal, h -YMO/MgO(111) and h -YMO/YSZ(111) are 63K, 70K, 103K and 140K. Why the Néel temperature shift from 63K to 140K? We think it's to

be in connection with the strain effect. In chapter 4, we will use optical pump-optical probe to confirm this discover further.



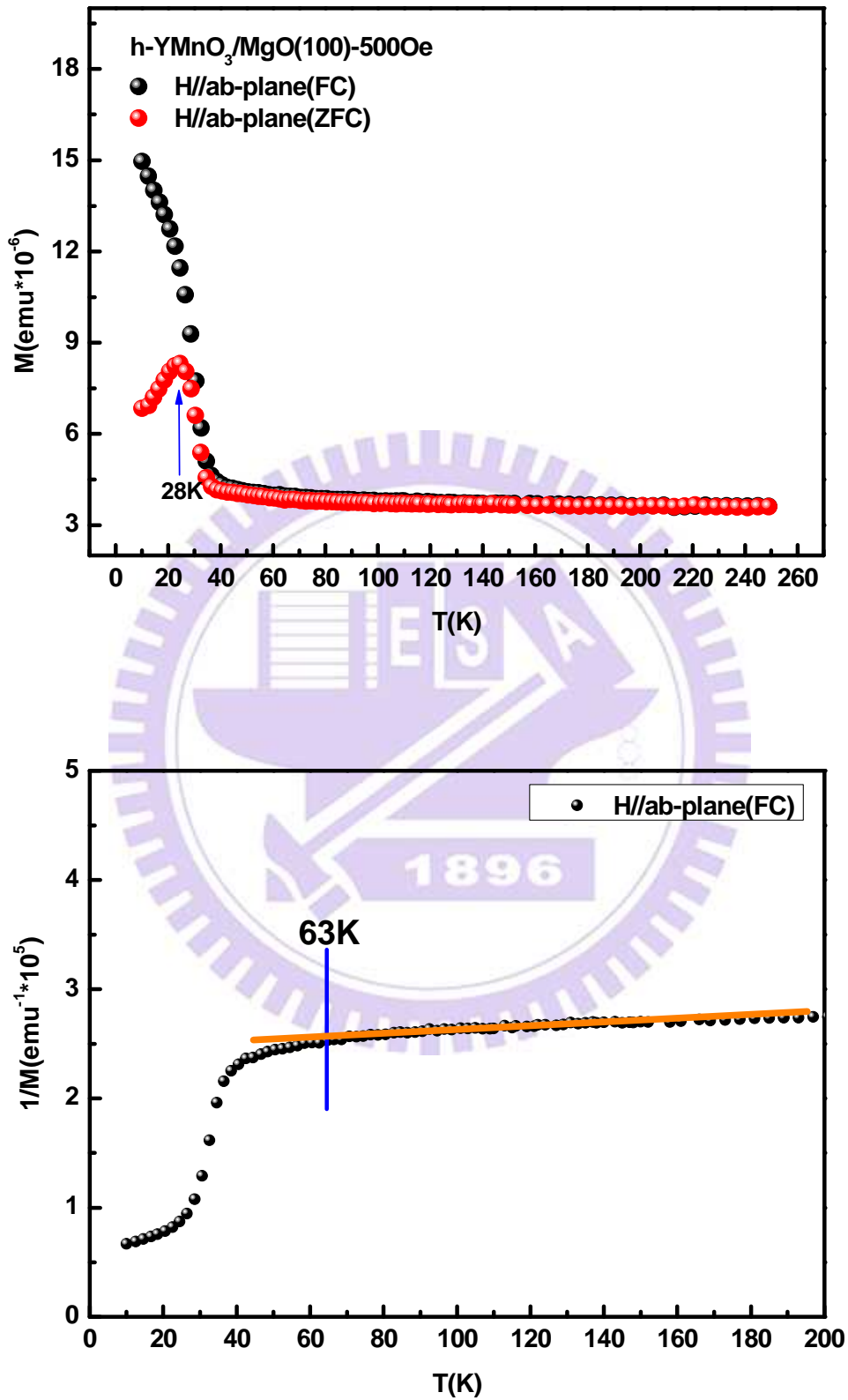


Fig.2-11 show magnetization vs temperature (M-T) curves and the reciprocal magnetization vs temperature (1/M-T) for $h\text{-YMO}/\text{MgO}(100)$ with FC and ZFC parallel to the film surface.

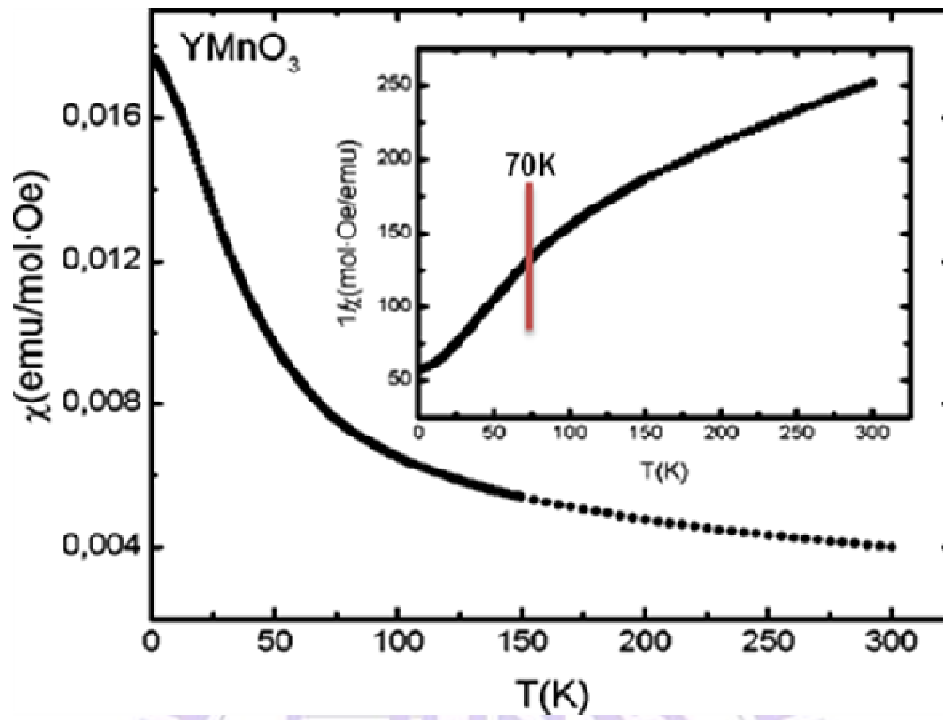
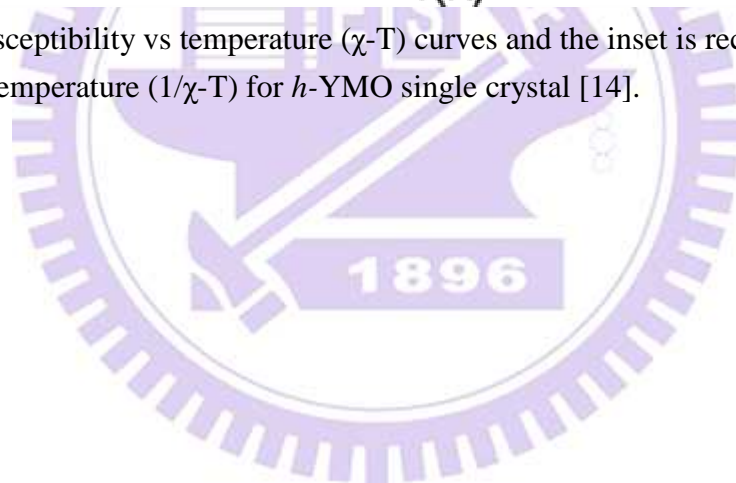


Fig.2-12 show susceptibility vs temperature (χ -T) curves and the inset is reciprocal susceptibility vs temperature ($1/\chi$ -T) for *h*-YMO single crystal [14].



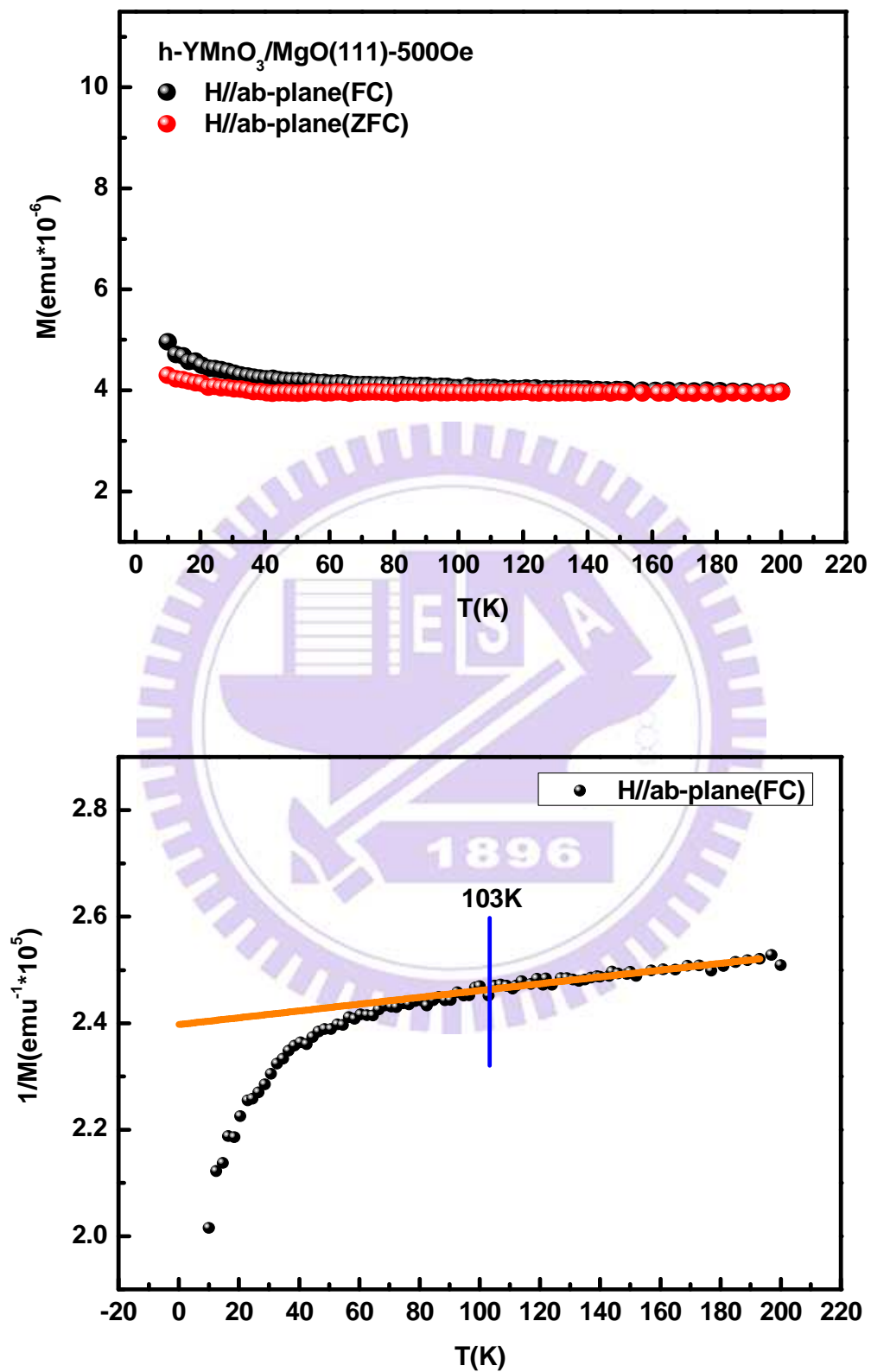


Fig.2-13 show magnetization vs temperature (M-T) curves and the reciprocal magnetization vs temperature (1/M-T) for *h*-YMO/MgO(111) with FC and ZFC parallel to the film surface.

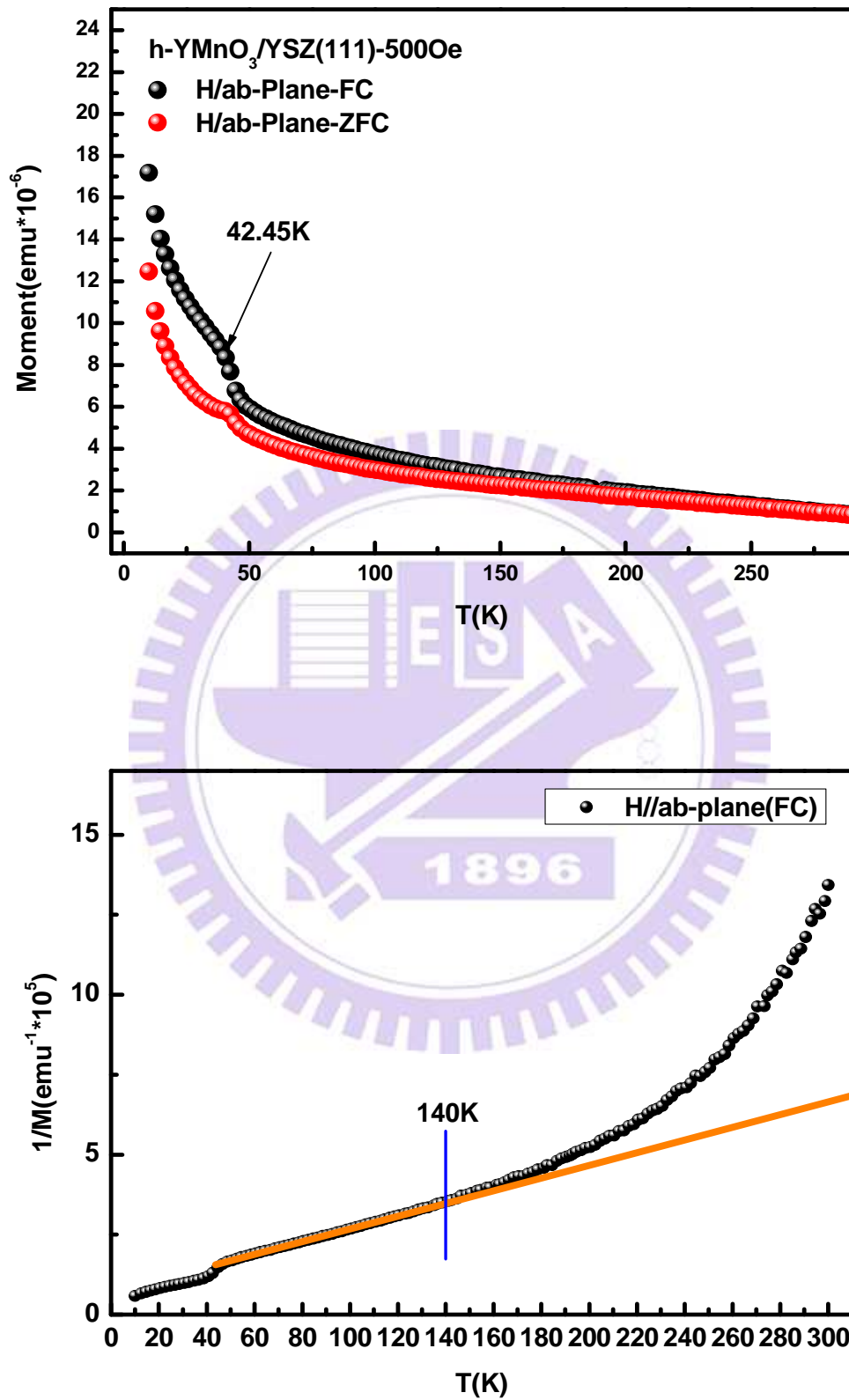


Fig.2-14 show magnetization vs temperature (M-T) curves and the reciprocal magnetization vs temperature ($1/M$ -T) for $h\text{-YMO}/\text{YSZ}(111)$ with FC and ZFC parallel to the film surface.

Chapter 3 Optical pump-optical probe (OPOP)

3-1 OPOP Background

In optical pump-optical probe measurement, we separate the pulse laser beam into pump and probe beam, separately. The ratio of intensity between pump and probe beam is (60mW): (2mW).

First, we adjusted the optical path difference to control the time difference of pump and probe beam reaching the sample, this way we called delay time. When pump beam reached the sample, it will cause an event, $n(t)$, its lifetime between two pulses must not exceed 13ns between two pulses.

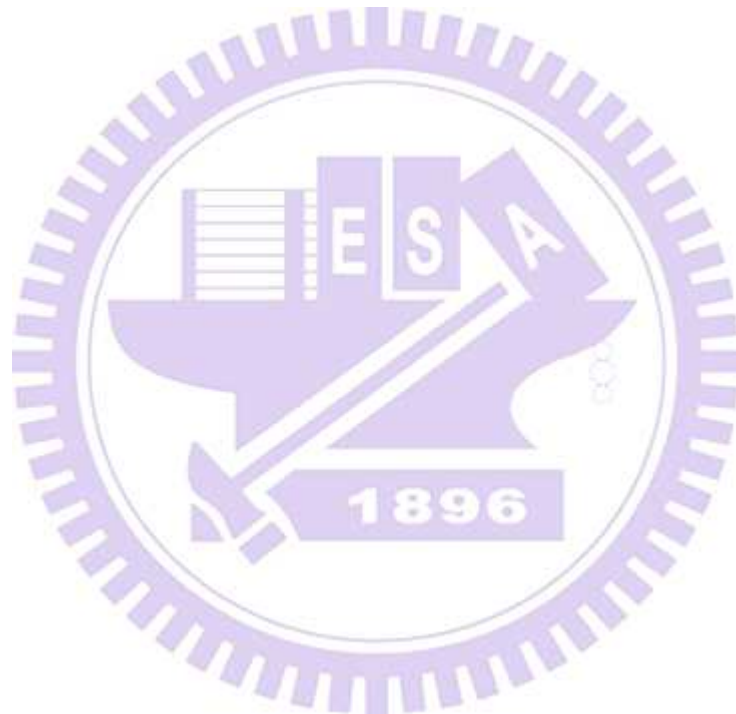
Since $n(t)$ is triggered by a laser (pump) pulse train, $n(t)$ shows its replica with a period of 13 ns. Assuming that the $n(t)$ could be related to the index of reflection, the reflection(or transmission) intensity of probe pulses from sample will vary with $n(t)$ while the probe pulses temporally overlapped with $n(t)$. However, this change due to $n(t)$ is very small, typically between $10^{-5} \sim 10^{-7}$, and is very difficult to detect directly under the noisy background (including laser noise, electronic noise, mechanic vibration etc.) by photodiode.

Hence, the lock-in amplifier was usually used to remove the background noise and amplify the signals. Accordingly, we also added an acousto-optic modulator (AOM) on the pump path with modulating at 97.733 KHz, the frequency is the same with lock-in amplifier where the noise was smaller and the gain of the narrow band amplifier was maximum. By varying the time delay (t) between pump and probe pulses, $\Delta I(t)$ would change as a function of time delay. It's show as Eq.3-1, $I_o(t)$ is DC voltage signal that it stand for the intensity of reflectivity. And $\Delta I(t)$ is stand for the change (ΔR) of reflectivity. Finally, due to the value of $\Delta I(t)/\Delta I_o(t)$ will understand the situation of $\Delta R(t)/R(t)$.

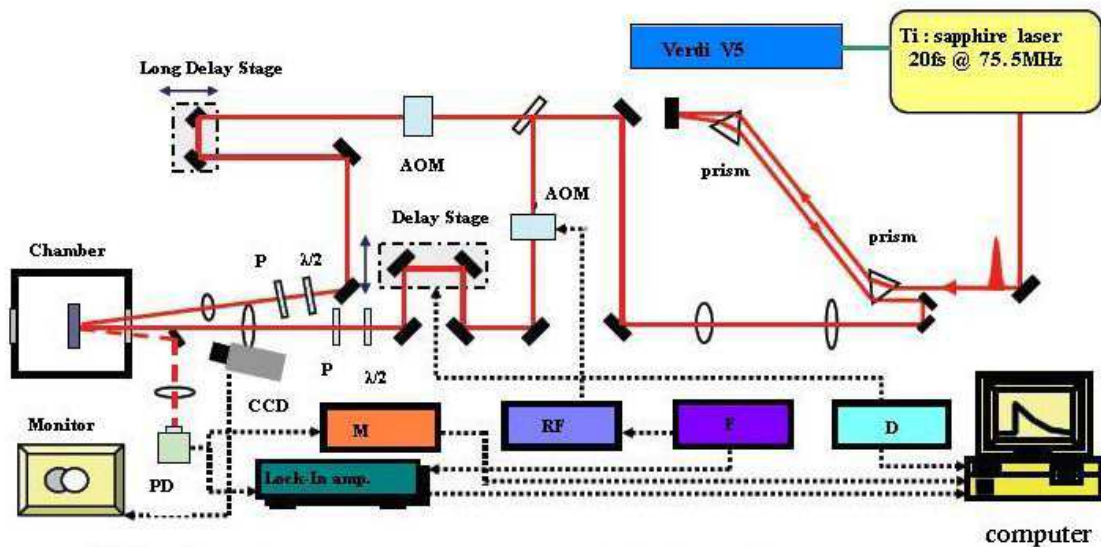
$$\frac{\Delta R}{R} = \frac{R_{Pump\ Open} - R_{Pump\ Closed}}{R_{Pump\ closed}} = \frac{\left(\frac{I_r}{I_i}\right)_{Pump\ Open} - \left(\frac{I_r}{I_i}\right)_{Pump\ Closed}}{\left(\frac{I_r}{I_i}\right)_{Pump\ Closed}} = \frac{(I_r)_{Pump\ Open} - (I_r)_{Pump\ Closed}}{(I_r)_{Pump\ Closed}} = \frac{\Delta I}{I_0}$$

where $(I_i)_{Pump\ Open} = (I_i)_{Pump\ Closed}$ and $(I_r)_{Pump\ Closed} \equiv I_0$ [15]

Eq. 3-1, $I_o(t)$ is DC voltage signal that it stand for the intensity of reflectivity. And $\Delta I(t)$ is stand for the change (ΔR) of reflectivity.



3-2 System of OPOP



P : Polarizer , PD : Photo Diode , AOM : Acousto-Optic Modulator ,
M : Multimeter , RF : RF Driver , F : Function Generator ,
D : Delay Stage Controller ,

Fig.3-1 the setup of pump-probe spectroscopy. AOM: acousto-optic modulator.

P: polarizer. CCD: CCD camera. PD: photodiode. M: multimeter. RF: RF driver. F: function generator. D: delay controller. The solid and dashed lines represent the laser beam path and the dotted lines stand for the electrical signal connection [15].

Fig. 3-1 is the pump-probe system. The light source is Ti: sapphire laser, excited source is Coherent Verdi V5 solid-state laser, wavelength is 532nm and the maximum output is 5W. After mode-lock, the central wavelength of pulse laser is 800nm. Pulse width is about 20fs, and its repetition rate is 75.5MHz.

Although the pulse width is 20fs, it will broaden the pulse width after pulse laser go through a series of optical components. For example, lens, reflector, gold mirror, acousto-optic modulator, polarizer, half-wave plates and quartz windows of the chamber...etc. These optical components will get rise to positive group velocity dispersion. Hence, we will add a pair of prisms to pre-chirp the pulses. That is two prisms provide negative group velocity dispersion to cancel out the positive group velocity dispersion.

It can make sure the pulse width to reach the sample is same as output pulse width from the laser. In brief, we used a pair of prisms to add in the optical components with negative GVD to compensate the positive GVD. Next, we used beamsplitter to get pump beam (60mW) and probe beam (2mW).

Pump beam

First, pump beam will go through an acousto-optic modulator (AOM), and it will be driven by the RF driver and modulated the pump beam at 97.733 KHz. At the same time, it also sent the same frequency into lock-in amplifier.

Then, pump beam will pass time delay stage. This stage is composed of retroreflector and high precision stage. By varying the position of stage, we have the function of time-resolve to control the relative τ time between pump and probe beam when these beams reached the sample. The stage we used is Newport PM500 series. Next, pump beam will pass the $\lambda/2$ plate and polarizer; it allowed us to adjust the intensity and polarization (electric field, E) of pump beam, respectively.

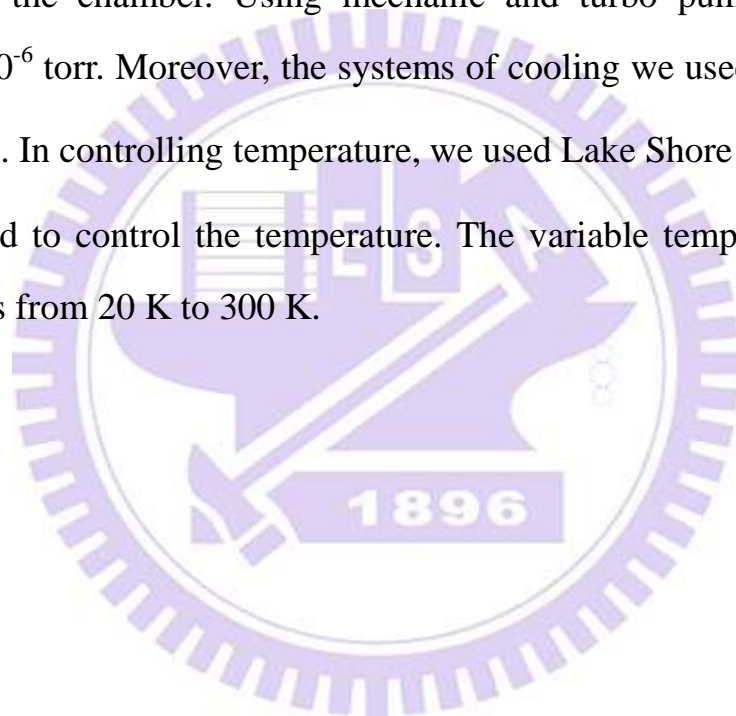
Probe beam

In the beginning, probe beam also go through the same AOM like pump beam. We will not modulate the frequency, because we just made the same compensate dispersion on pump and probe beams. Next, probe beam will pass beamsplitter to separate two beams, one is go through a polarizer and detect by photodetector directly as reference signal. The other is like pump beam, pass the $\lambda/2$ plate, polarizer to control the direction of polarization and intensity, respectively. The spatial overlap of pump and probe beams on the sample was monitored by the CCD camera. The reflection of the probe beam (its sample signal) was received by the photodiode. It will transform photon signal into electric signal. The

multimeter and the lock-in amplifier took the DC (R) and AC (ΔR) components in the signal, respectively. Finally, we used the computer to control the delay stage and measured the data ($\Delta R/R(t)$).

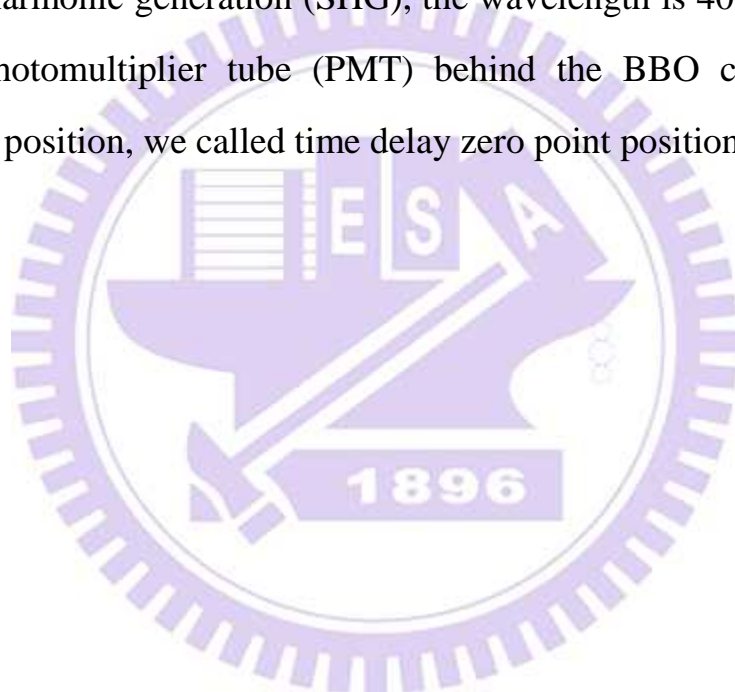
3-3 Cooling system

In order to measuring properties of the sample under low temperature, we established a cooling system. First, we put the sample on the holder, and then put them into the chamber. Using mechanic and turbo pump to lower the pressure into 10^{-6} torr. Moreover, the systems of cooling we used are open cycle and close cycle. In controlling temperature, we used Lake Shore 331, it is a $25\ \Omega$ heater was used to control the temperature. The variable temperature range in this system was from 20 K to 300 K.



3-4 Time delay zero point positioning

In our experiments, when pump beam and probe beam hit the sample simultaneously, they must get to the time and spatial overlap. The spatial overlap of pump and probe beams on the sample was monitored by the CCD camera. The reflection of the probe beam was received by the photodiode. In other way, we can use a nonlinear second harmonic crystal, BBO (Beta-Barium Borate) to do the time overlap. The pump and probe beam were focused and crossed on the BBO crystal. Under the phase-matched condition, it could radiate the maximum of the second harmonic generation (SHG), the wavelength is 400nm, it could be detected by photomultiplier tube (PMT) behind the BBO crystal. And the phase-matched position, we called time delay zero point positioning.



3-5 Experimental methods and process

After setup the OPOP system, we can start to do the measurement of ultrafast laser spectroscopy. And the detail experiment steps are showed below:

I. Open the laser power:

Ti-sapphire laser needed two hours from the beginning to stabilization, and it should notice the temperature of cooling system and water flow. Then, let the laser under mode-locked operation and write down the power, beam profile and position. Using the spectroscopy to check if CW term still exist. After checking the situation of the laser, the high S/N (signal to noise) ratio of spectra will be achieved.

II. Paste samples:

We put the sample on the holder by double coated carbon conductive tapes. Because carbon conductive tapes have thickness, we must do the best to paste it evenly. It could avoid the error.

III. Guide the light:

After pasting samples and putting into the chamber, we adjusted the light path, and made sure pump beam and probe beam would reach the sample surface accurately. Then, we adjusted the reflected mirrors, it let probe beam reflect to the photo detector. But we must avoid the pump beam reflect to the detector, we would put a polarizer in front of the detector to reduce it. After double checking the light path, we opened the pump, lowering the pressure under 10^{-6} torr.

IV. Spectrum measurement under room temperature:

In experiment process, we measured the direction of polarization and power of pump beam and probe beam by adjusting polarizer and $\lambda/2$ plate, respectively. In this experiment, the power of pump and probe beam are 60mW and 2mW. And the angle of the polarization direction of both the pump and probe pulses are 90° . However, the reference signal must be twice larger than the reflective signal in order to lower the background noise. The spot would be a little bit shifted after delay stage working. In general, we would let the pump beam spot is larger than probe beam spot. After doing this, we could make sure the overlap of pump and probe pulses, even if there were a little bit shift.

V. Spectrum measurement under lower temperature:

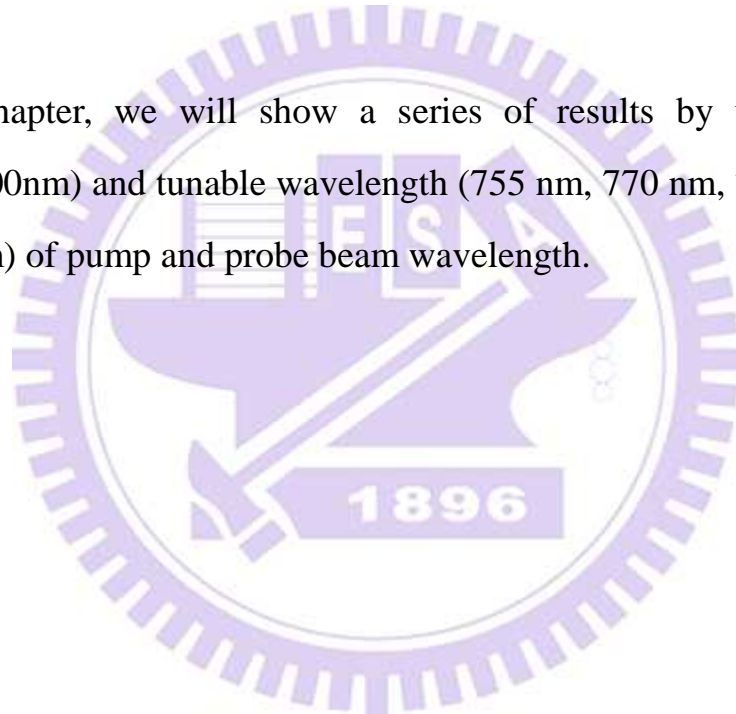
We controlled the flow of liquid Helium and liquid Nitrogen in cooling the sample, and $25\ \Omega$ heater was used to control the temperature. We could do the spectrum measurement under lower temperature by repeating step IV when it reached the temperature we wanted.

Chapter 4 Experimental Result and Discussion

4-1 Epitaxial-strain effect on Mn^{3+} d-d energy difference

We already prepared pure (001)-oriented hexagonal YMnO_3 (*h*-YMO) thin films on (100)MgO, (111)MgO and (111)YSZ substrates by pulsed laser deposition, respectively. We will show the results of the ultrafast dynamics in these samples probed by the OPOP technique, especially, the effect of strain due to lattice mismatch between the substrate and *h*-YMO films on the magnitude of E_{dd} . We found that E_{dd} change due to the small change of the ratio of lattice constant a/c .

In this chapter, we will show a series of results by using the same wavelength (800nm) and tunable wavelength (755 nm, 770 nm, 777 nm, 785 nm, 800 and 815nm) of pump and probe beam wavelength.



4-1-1 Pump-Probe results (Fix wavelength)

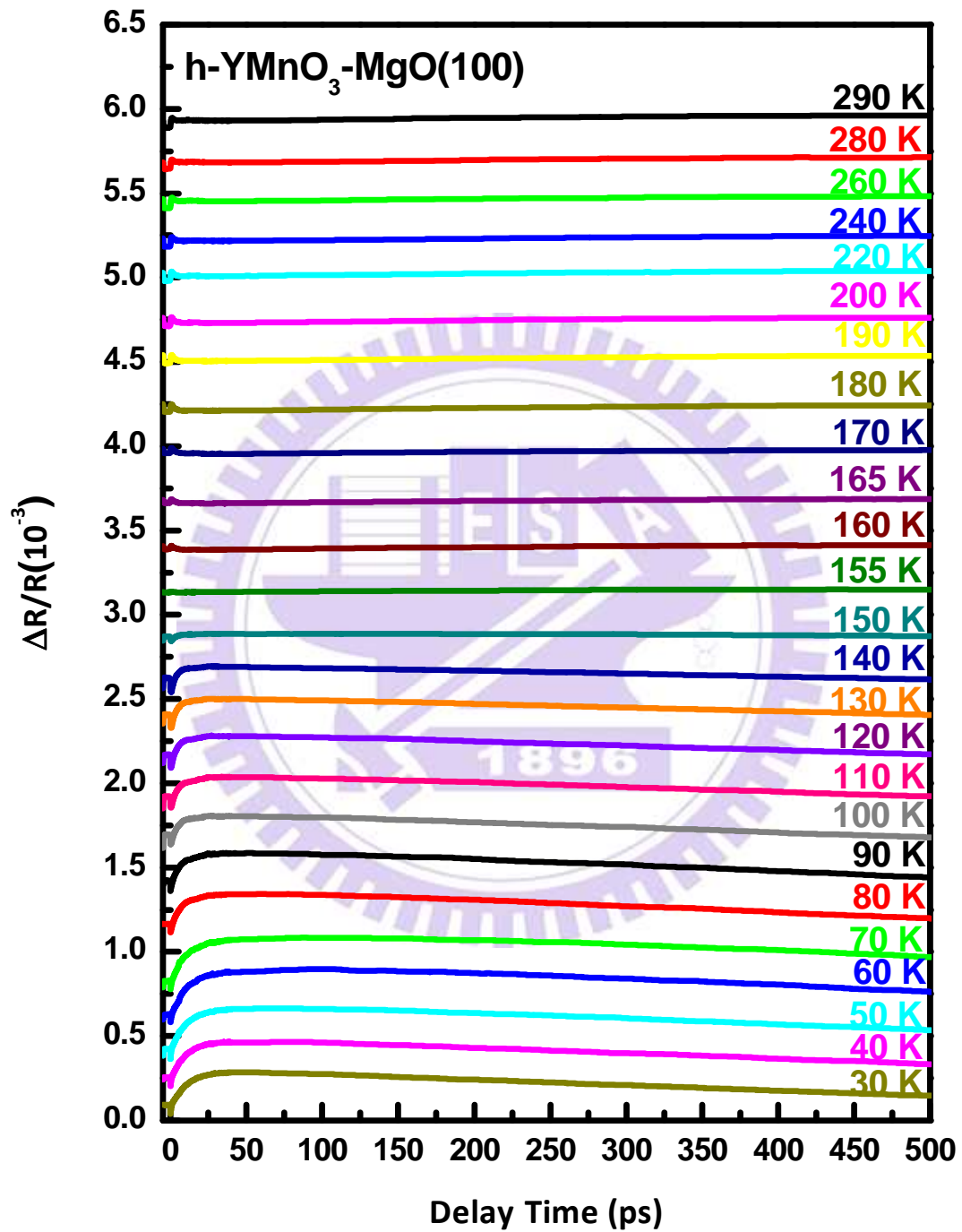


Fig. 4-1 The transient reflectivity $\Delta R/R$ curves of h -YMnO₃/MgO(100) samples measured at various temperatures.

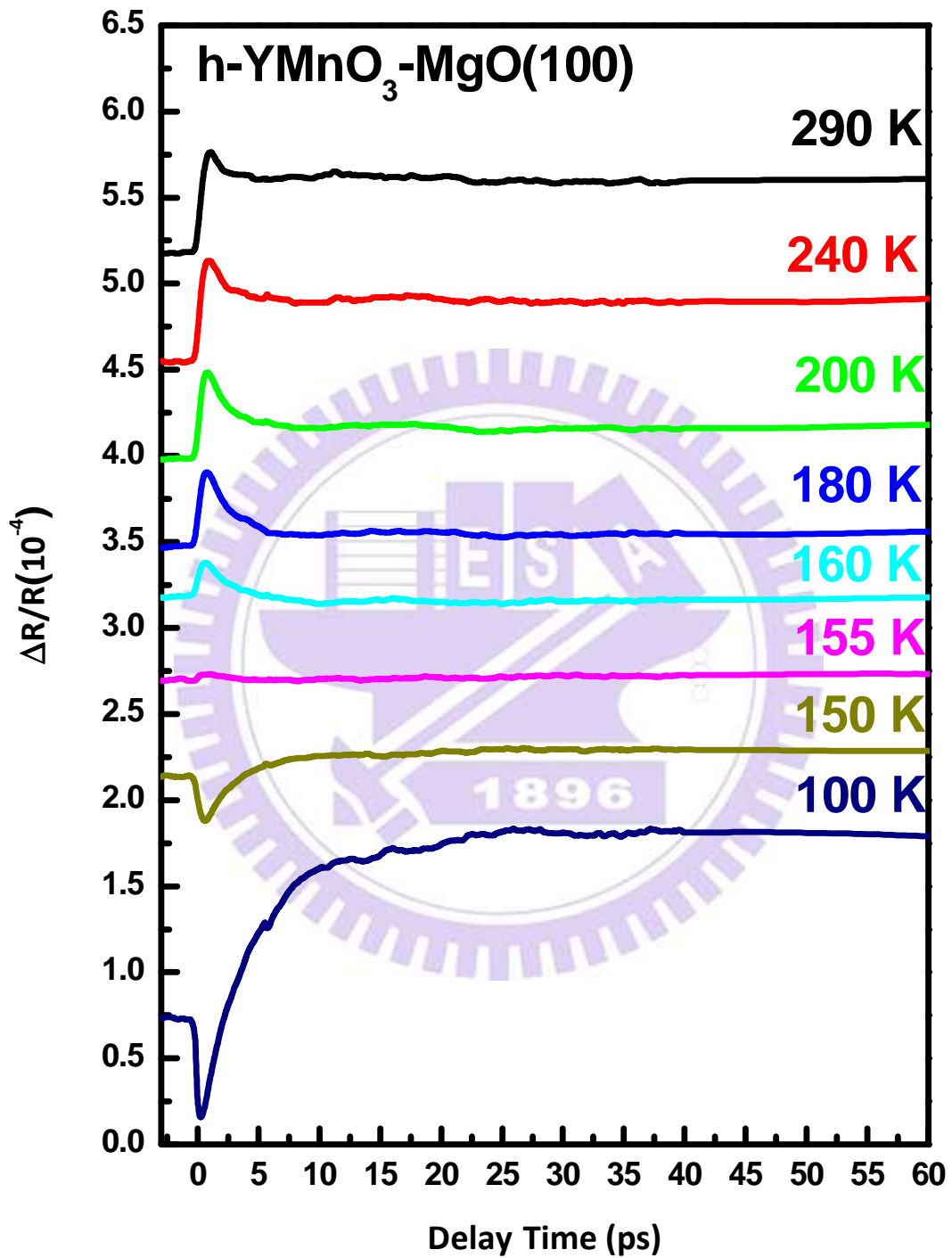


Fig. 4-2 The transient reflectivity $\Delta R/R$ curves of h -YMnO₃/MgO(100) samples measured at various temperatures (Part of Fig.4-1 data).

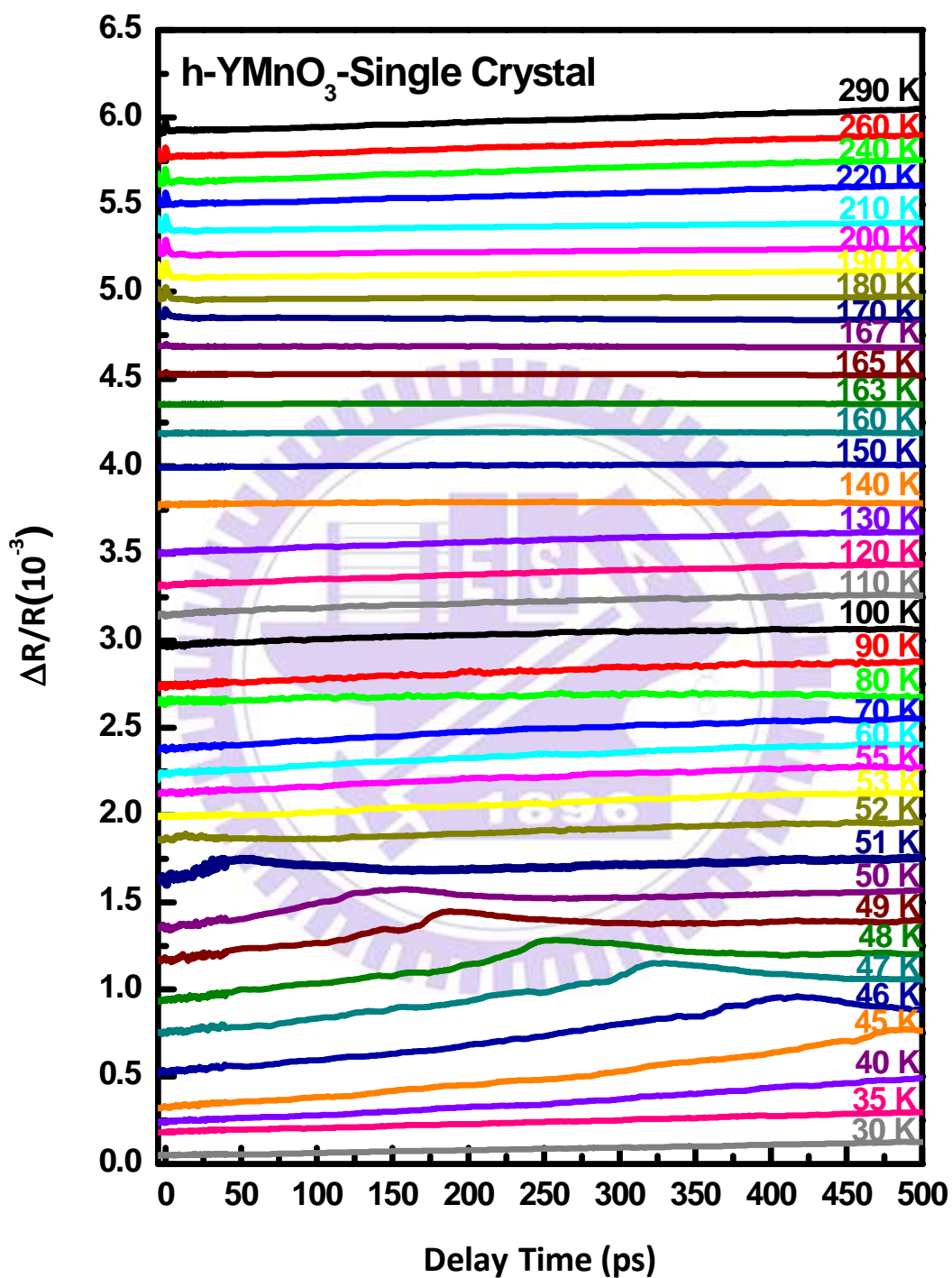


Fig. 4-3 The transient reflectivity $\Delta R/R$ curves of h -YMnO₃ single crystal samples measured at various temperatures.

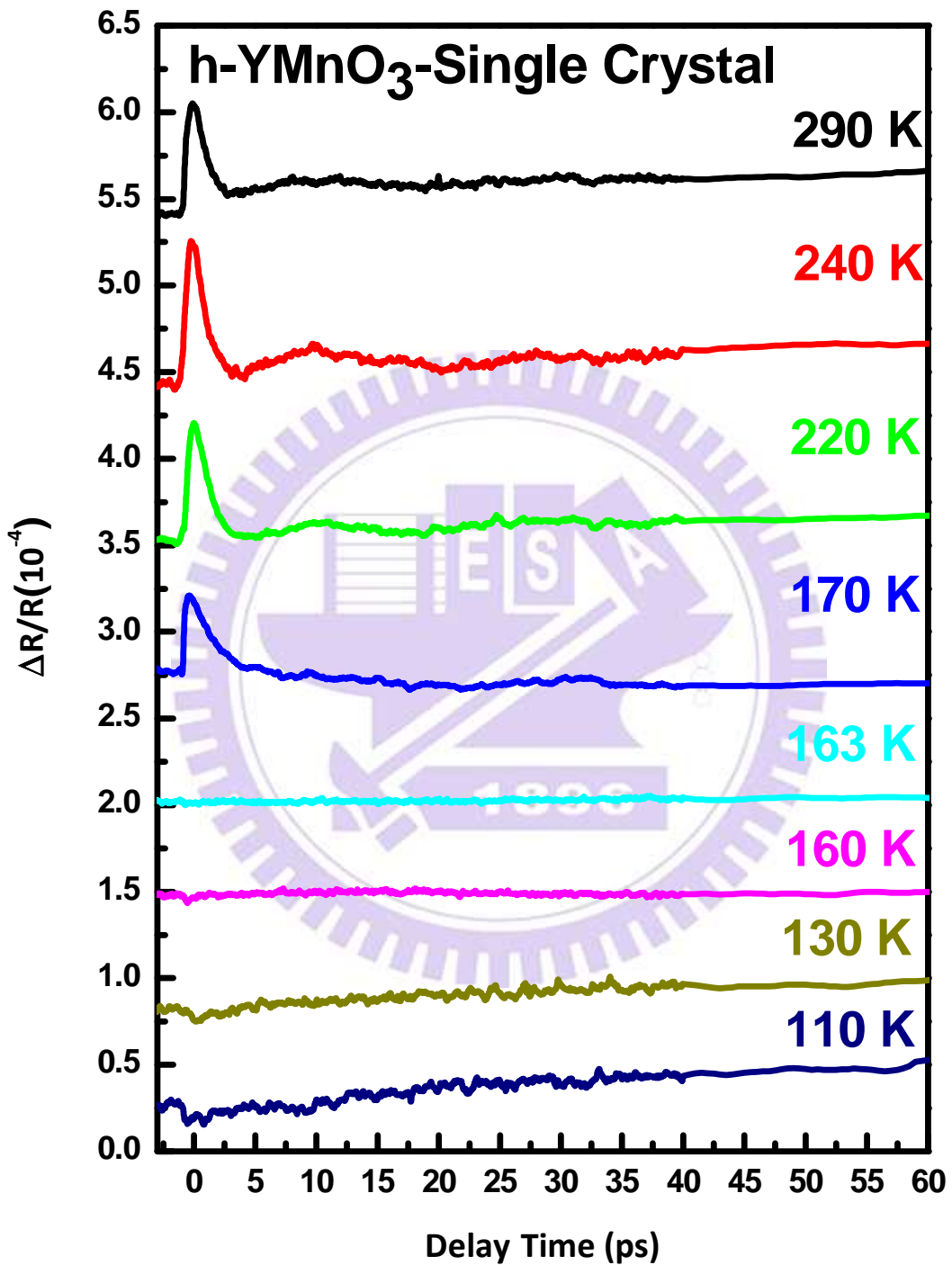


Fig. 4-4 The transient reflectivity $\Delta R/R$ curves of h -YMnO₃ single crystal samples measured at various temperatures (Part of Fig.4-3 data).

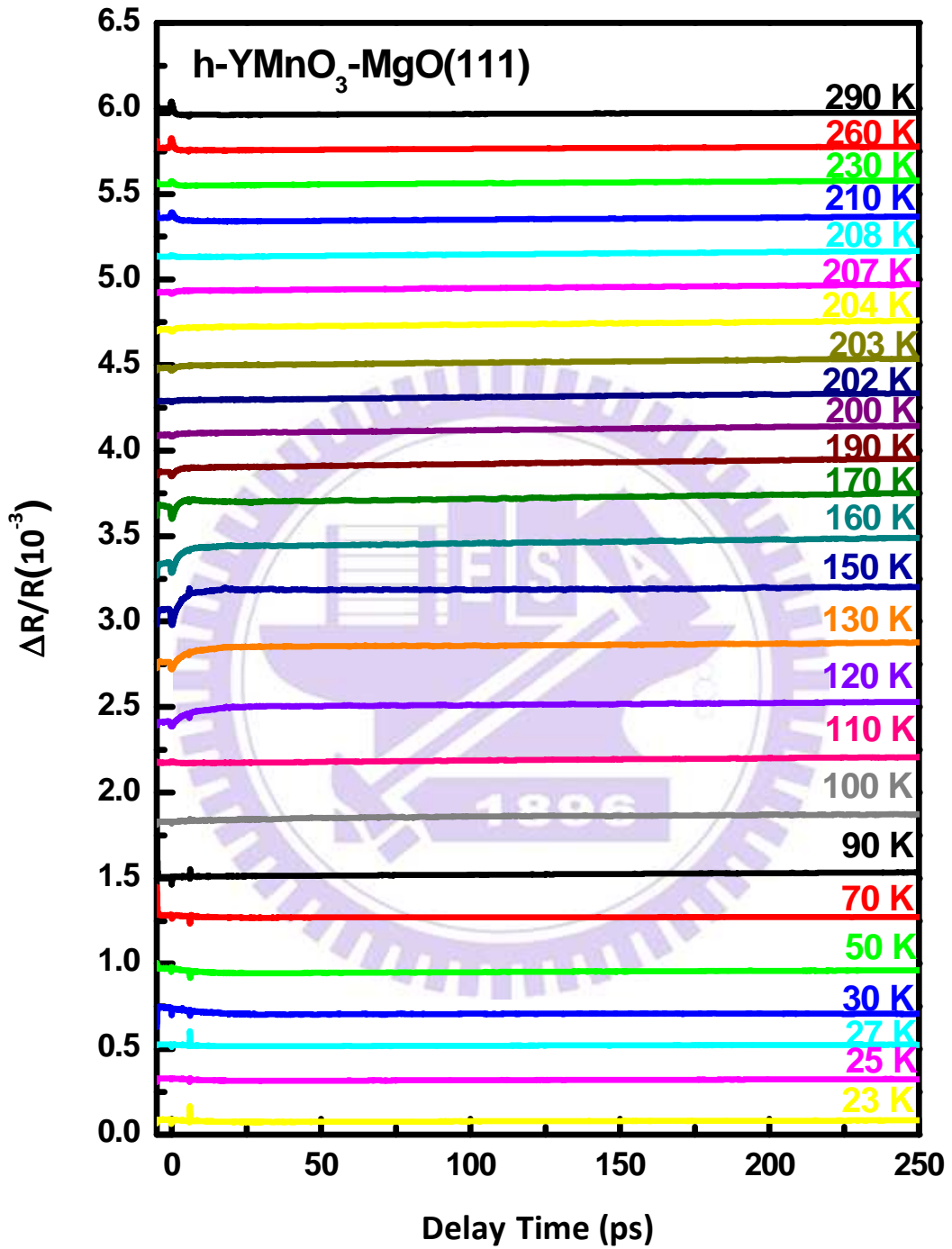


Fig. 4-5 The transient reflectivity $\Delta R/R$ curves of h -YMnO₃/MgO(111) samples measured at various temperatures.

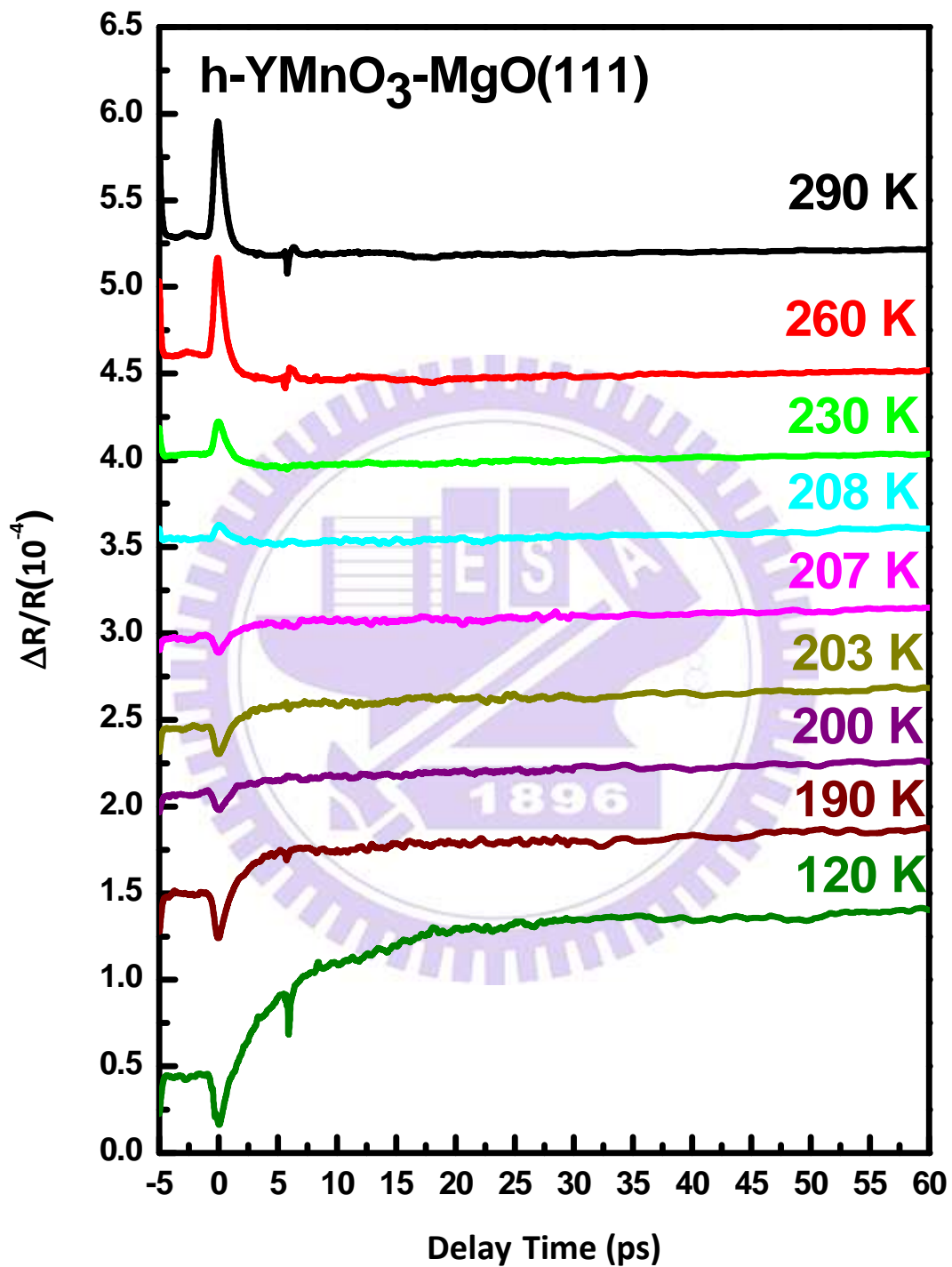


Fig. 4-6 The transient reflectivity $\Delta R/R$ curves of h -YMnO₃/MgO(111) samples measured at various temperatures (Part of Fig.4-5 data).

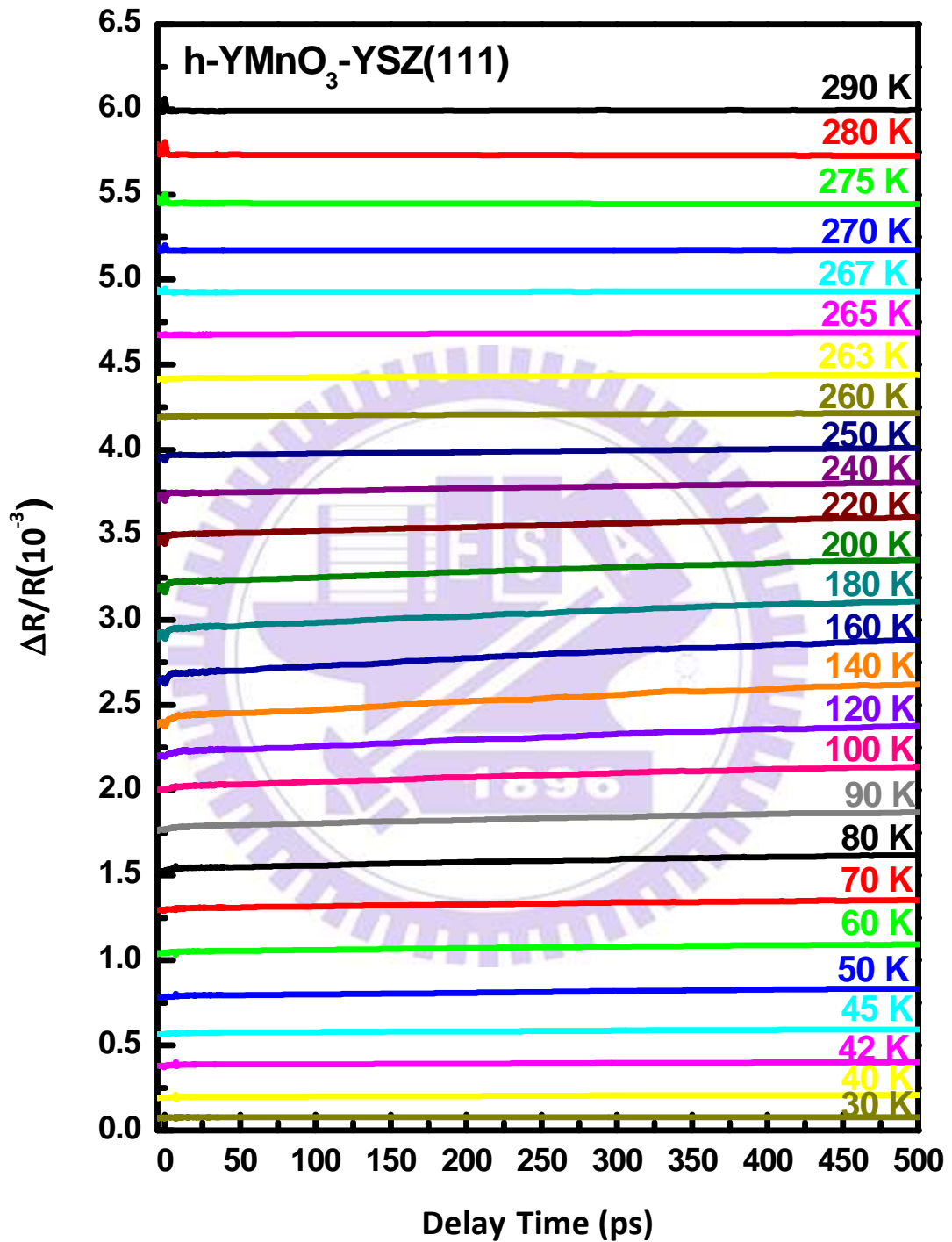


Fig. 4-7 The transient reflectivity $\Delta R/R$ curves of h -YMnO₃/YSZ(111) samples measured at various temperatures.

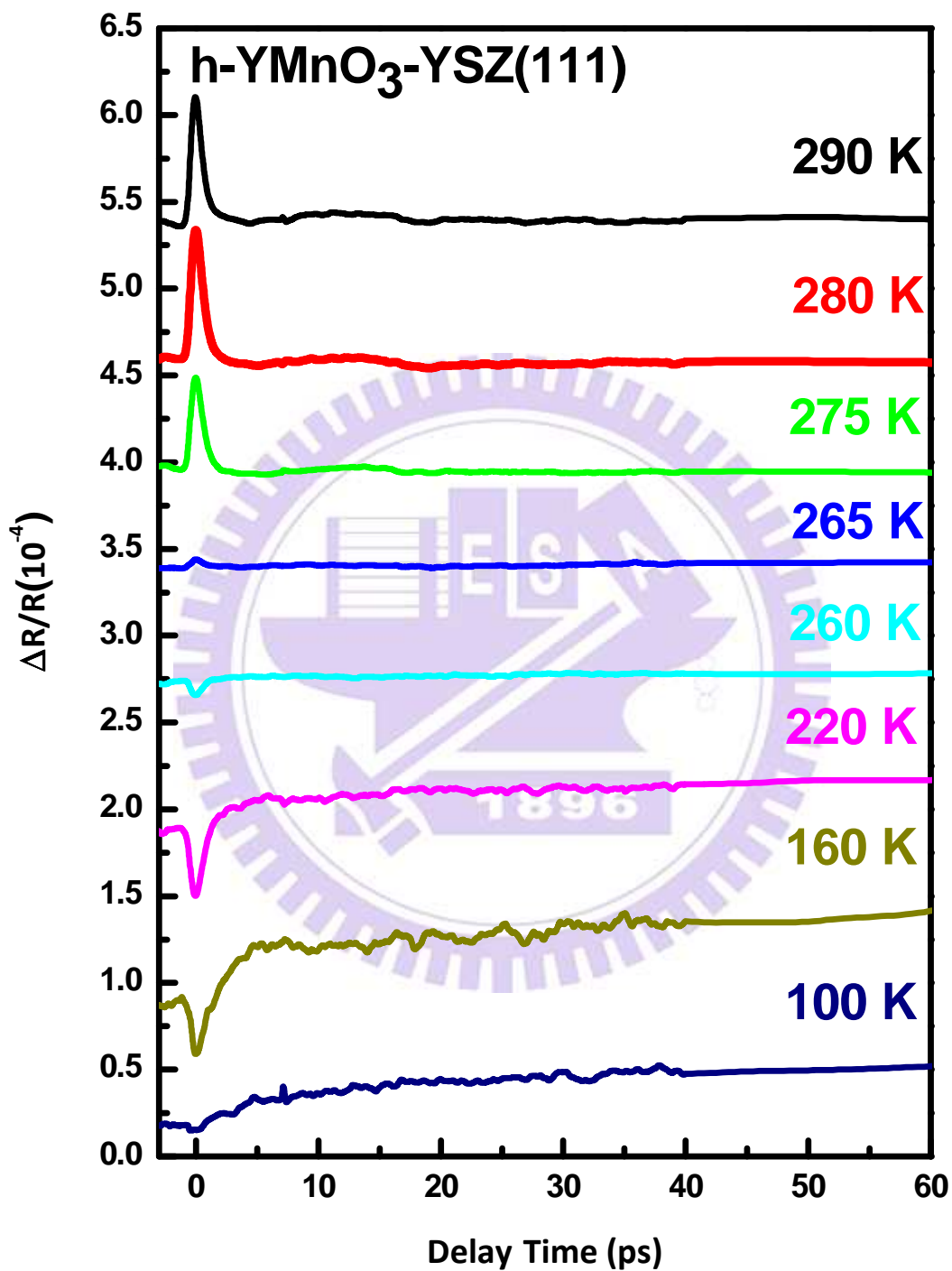


Fig. 4-8 The transient reflectivity $\Delta R/R$ curves of $h\text{-YMnO}_3\text{/YSZ}(111)$ samples measured at various temperatures (Part of Fig.4-7 data).

Base on the Fig. 4-8 at zero delay time, the amplitude of $\Delta R/R$ as a function of temperature of h -YMnO₃/YSZ(111) at 800nm show in Fig. 4-9(a). The amplitude of the $\Delta R/R$ appears to remain constant above 280K until it starts to drop noticeably from T=275 K. At T=265 K the amplitude of the excitation component has diminished completely and with T=260 K it even becomes negative. When the excitation component has diminished, the E_{dd} is equal to the photon energy at the moment. Fig.4-9(b) it's show energy difference of the Mn³⁺ energy levels in the local environment MnO₅ for photon energy above and below E_{dd} . Fig.4-9(c) it's show orbital-resolved densities of states of Mn 3d orbital's and the in-plane O 2p orbital for YMnO₃ [16], the range between two red lines we called Mn³⁺ d-d energy difference(E_{dd}).

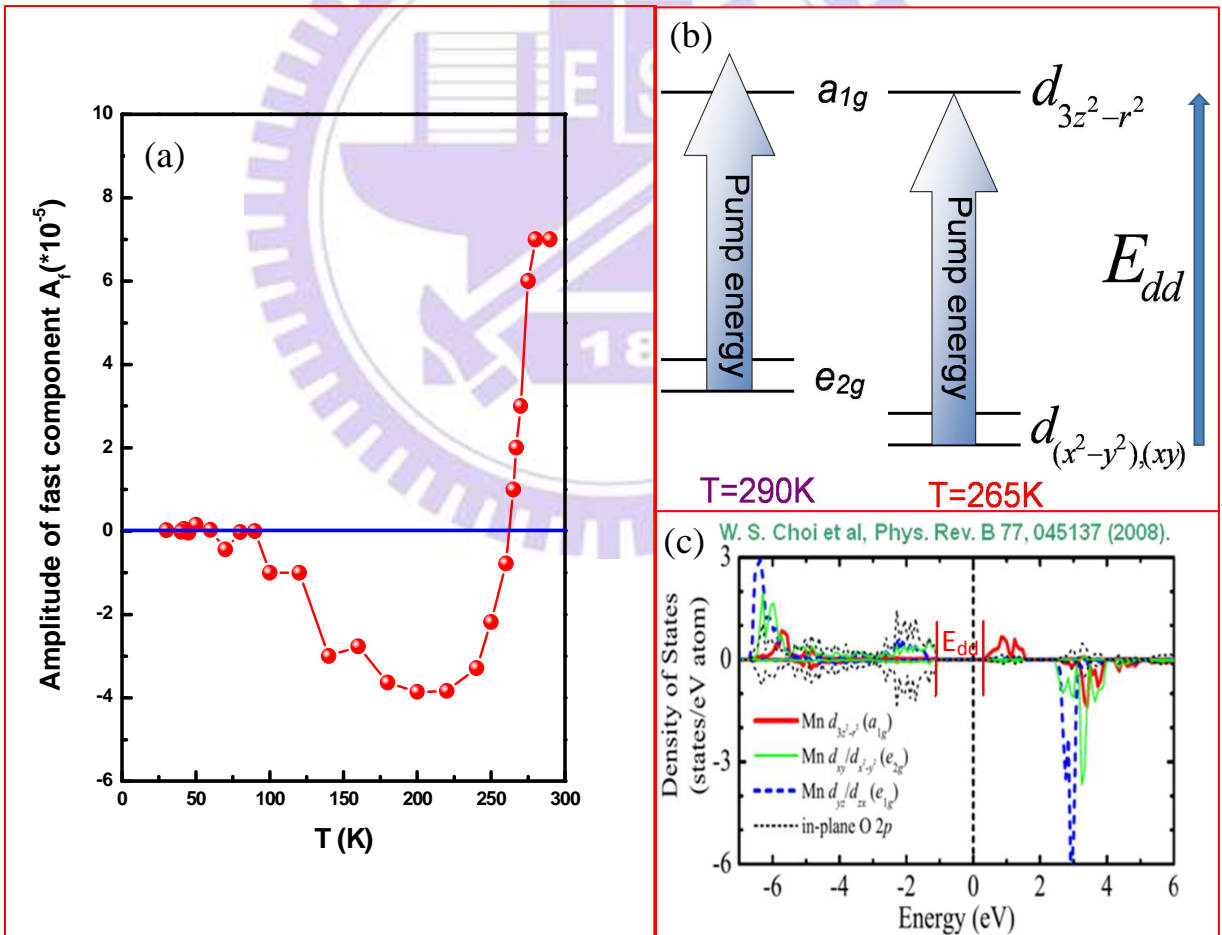


Fig.4-9 (a) The amplitude of $\Delta R/R$ as a function of temperature at 800nm taken from Fig.4-8 at zero delay time. (b) Energy difference of the Mn³⁺ energy levels in the local environment MnO₅ for photon energy above and below E_{dd} . (c) Orbital-resolved densities of states of Mn 3d orbitals and the in-plane O 2p orbital for YMnO₃ [16].

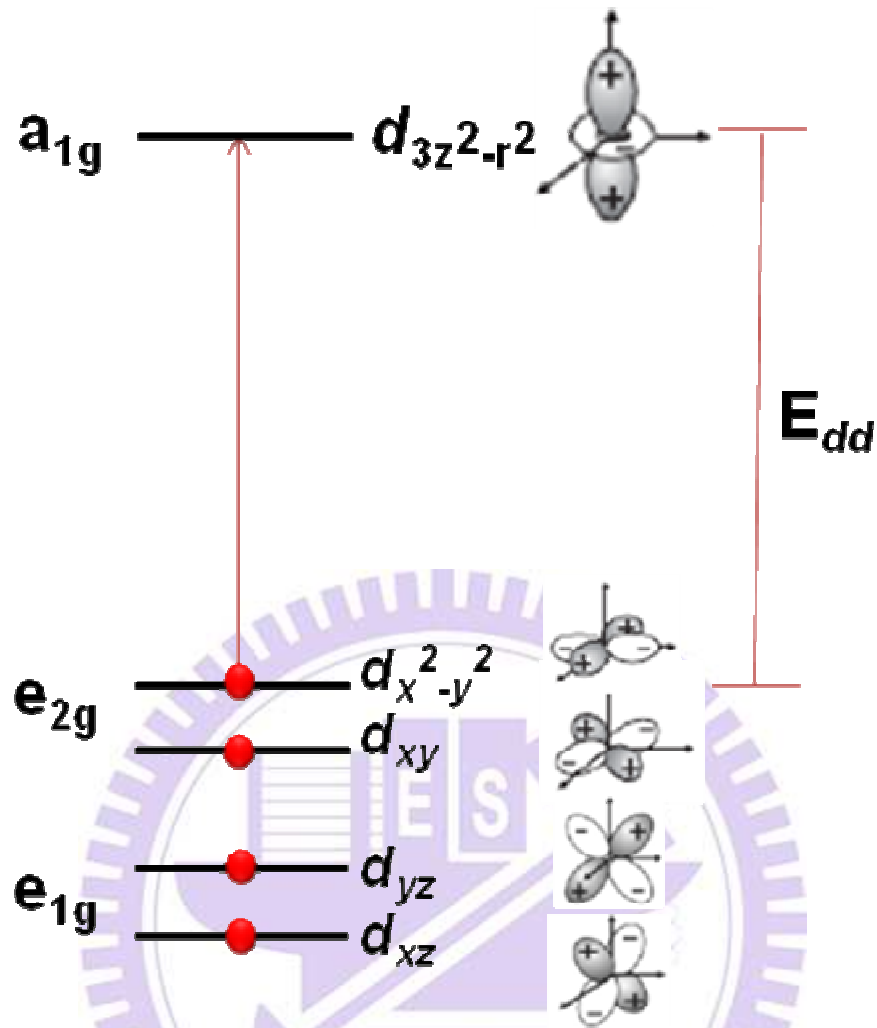


Fig.4-10 It illustrates the splitting of the Mn^{3+} energy levels in the local environment MnO_5 .

The electrons residing on the e_{2g} orbital (d_{xy} and $d_{x^2-y^2}$) can transfer to the unoccupied a_{1g} orbital ($d_{3z^2-r^2}$) by absorbing pumping photons with energy exceeding E_{dd} .

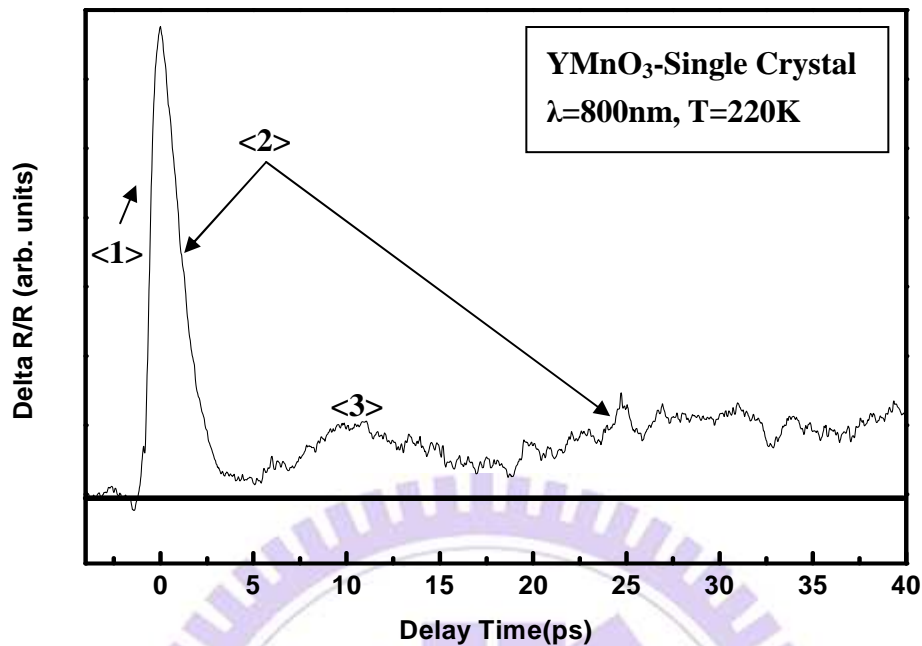


Fig.4-11 Three primary features of dynamics in the $\Delta R/R$ curves.

As show in Fig.4-11, the typical temperature-dependent $\Delta R/R$ for the h -YMnO₃/YSZ(111). **The initial excitation component <1>**, **the relaxation component <2>** and **the oscillation component <3>** is show Fig.4-11 process.

For example, YMnO₃/YSZ(111) show in Fig.4-8, the amplitude of the excitation of the $\Delta R/R$ process 1 appears to remain constant at high temperature until it starts to drop noticeably around T=280 K. At T=265K, it has diminished, and T=260K it even becomes negative.

The relaxation of the $\Delta R/R$ process 2 is higher than the beginning level above 290K, and it will be negative $\Delta R/R$ which appears to grow gradually with decreasing temperature.

The oscillator of the $\Delta R/R$ process 3 appears above T=265K. We can see in Fig.4-8, when there is positive excitation component, it will cause the oscillator component. The oscillation period is about 15ps.

4-1-2 Pump-Probe results (Tunable wavelength)

Pump-Probe: 815nm-815nm

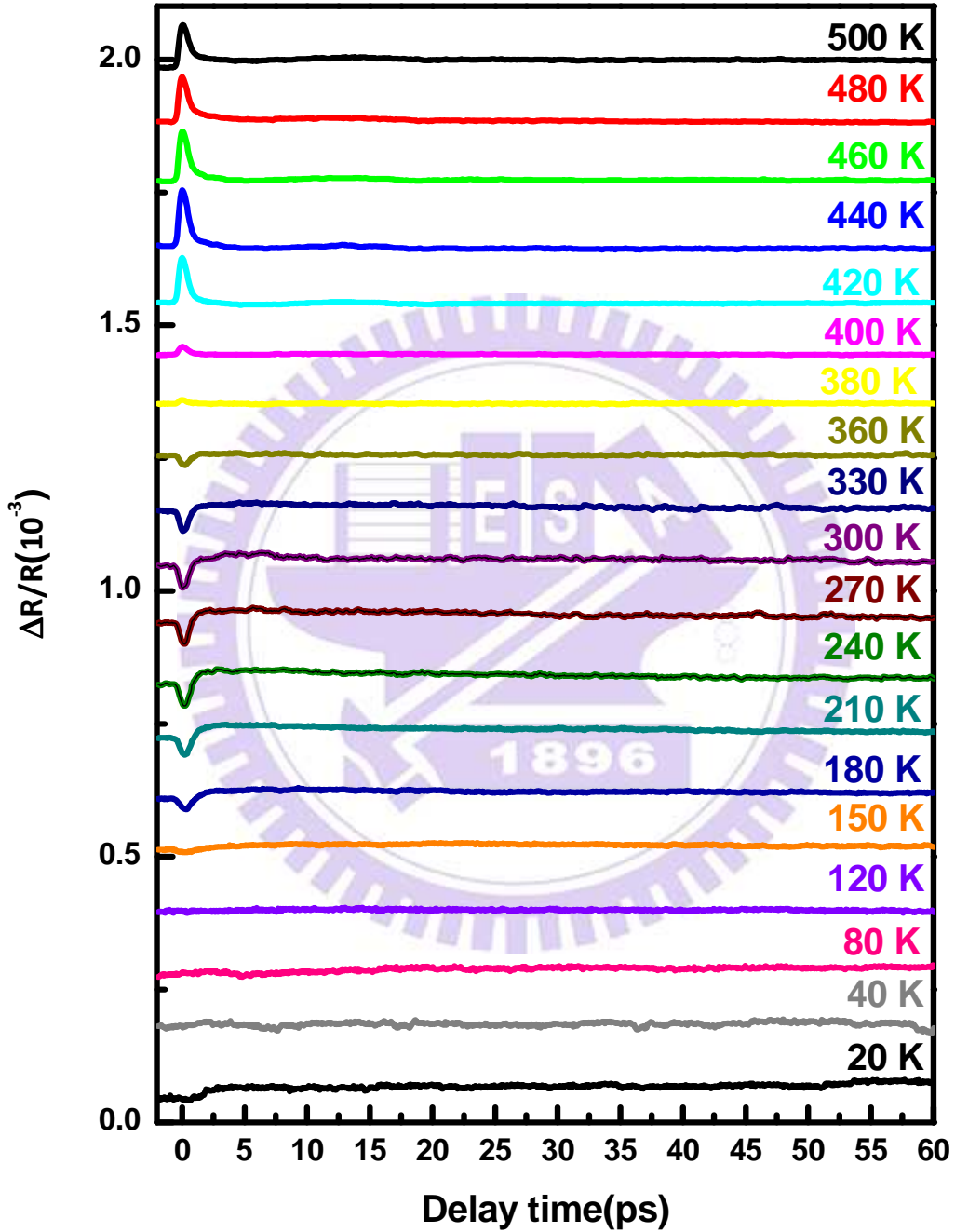


Fig. 4-12 The transient reflectivity $\Delta R/R$ curves of h -YMnO₃/YSZ(111) samples measured with the same pump and probe beam wavelength(815nm) at various temperatures.

Pump-Probe: 800nm-800nm

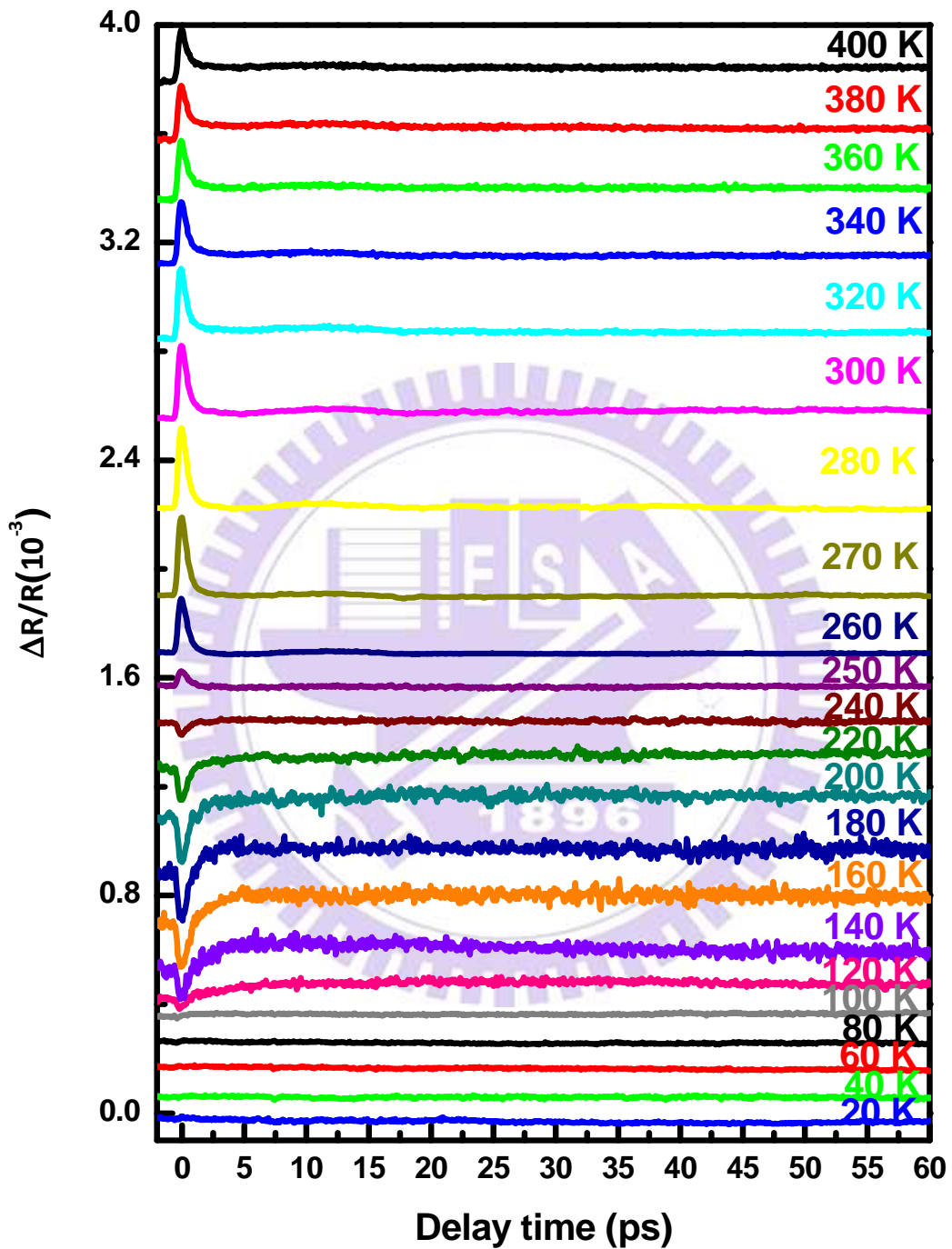


Fig. 4-13 The transient reflectivity $\Delta R/R$ curves of h -YMnO₃/YSZ(111) samples measured with the same pump and probe beam wavelength(800nm) at various temperatures.

Pump-Probe: 785nm-785nm

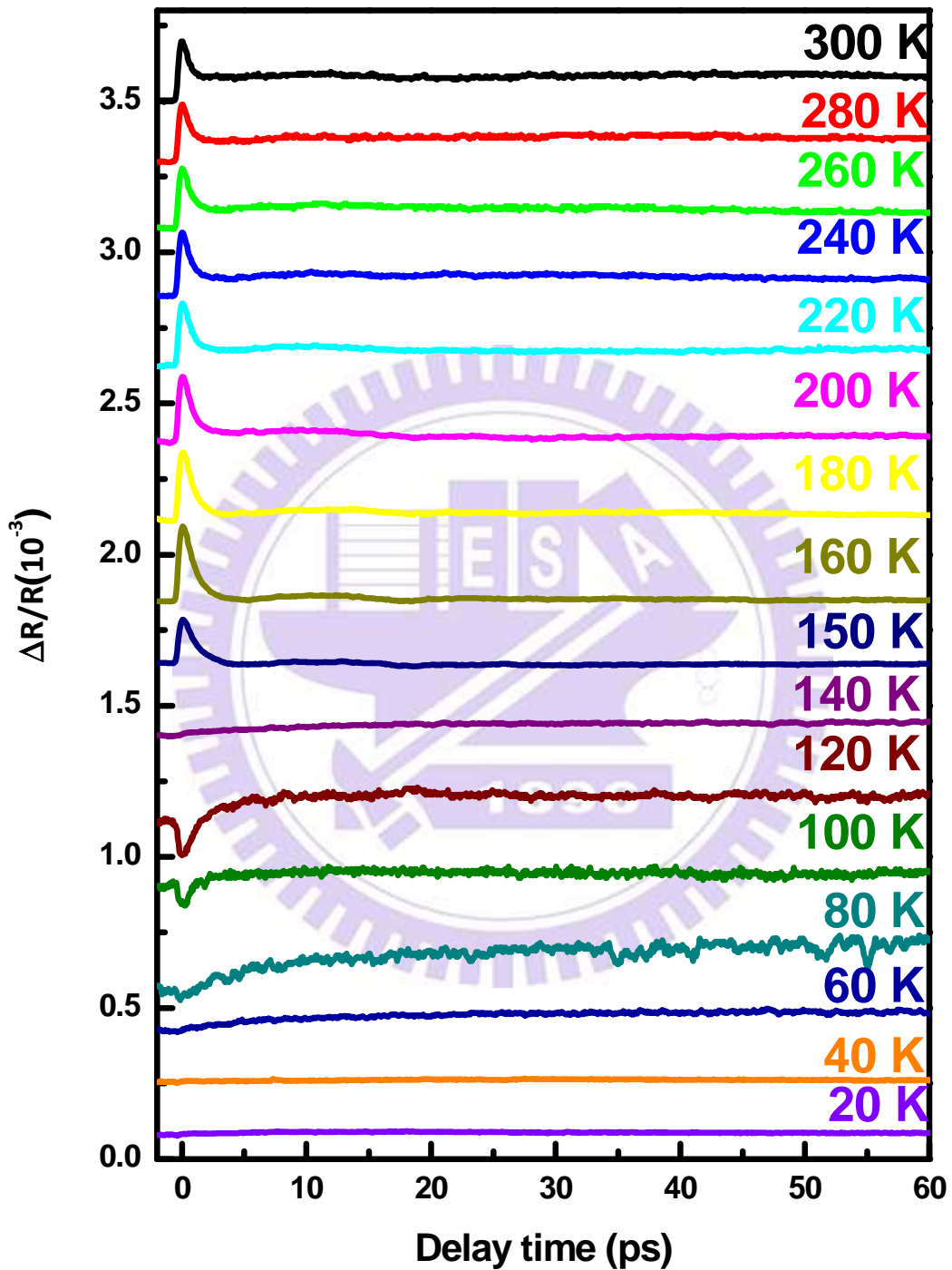


Fig. 4-14 The transient reflectivity $\Delta R/R$ curves of h -YMnO₃/YSZ(111) samples measured with the same pump and probe beam wavelength(785nm) at various temperatures.

Pump-Probe: 777nm-777nm

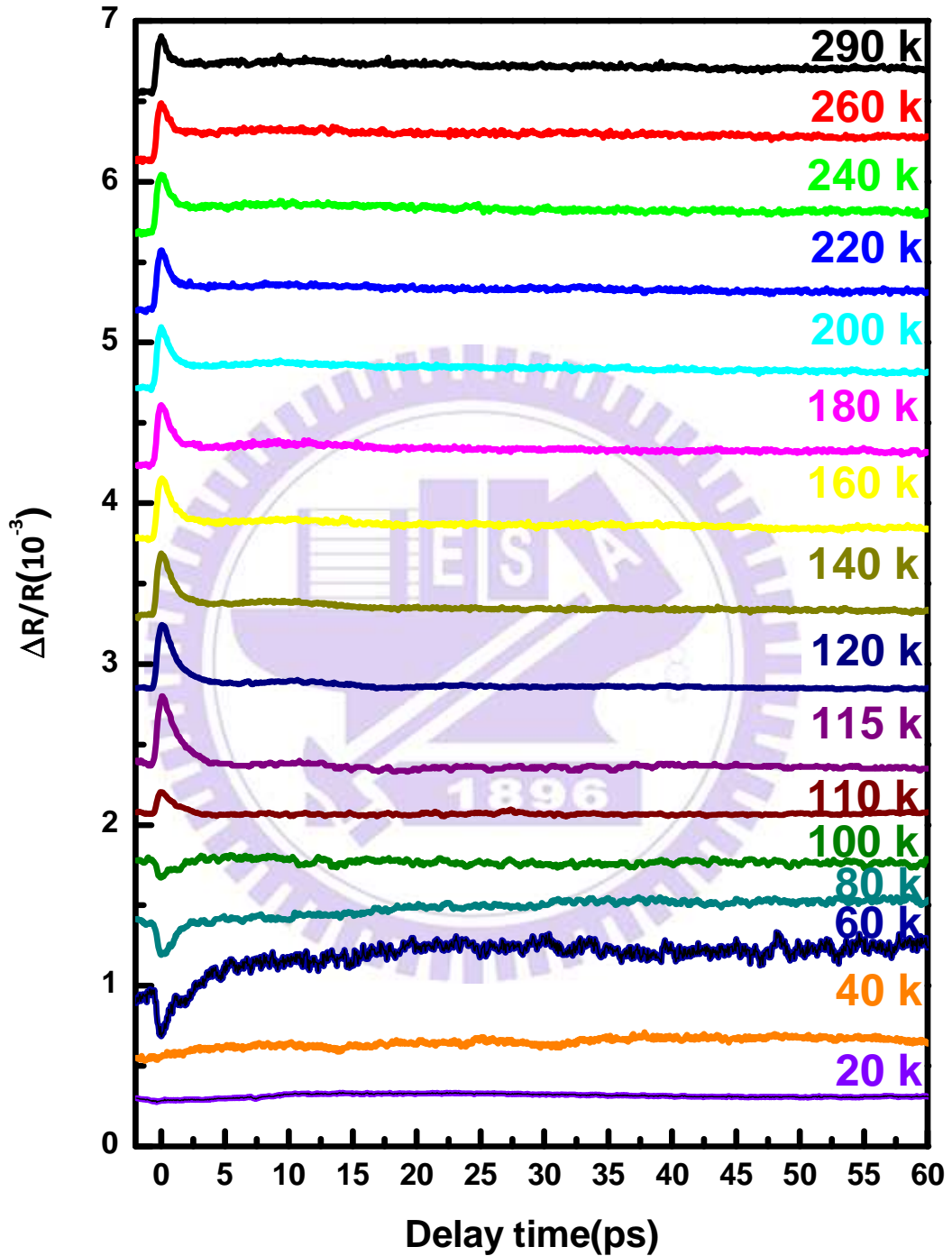


Fig. 4-15 The transient reflectivity $\Delta R/R$ curves of h -YMnO₃/YSZ(111) samples measured with the same pump and probe beam wavelength(777nm) at various temperatures.

Pump-Probe: 770nm-770nm

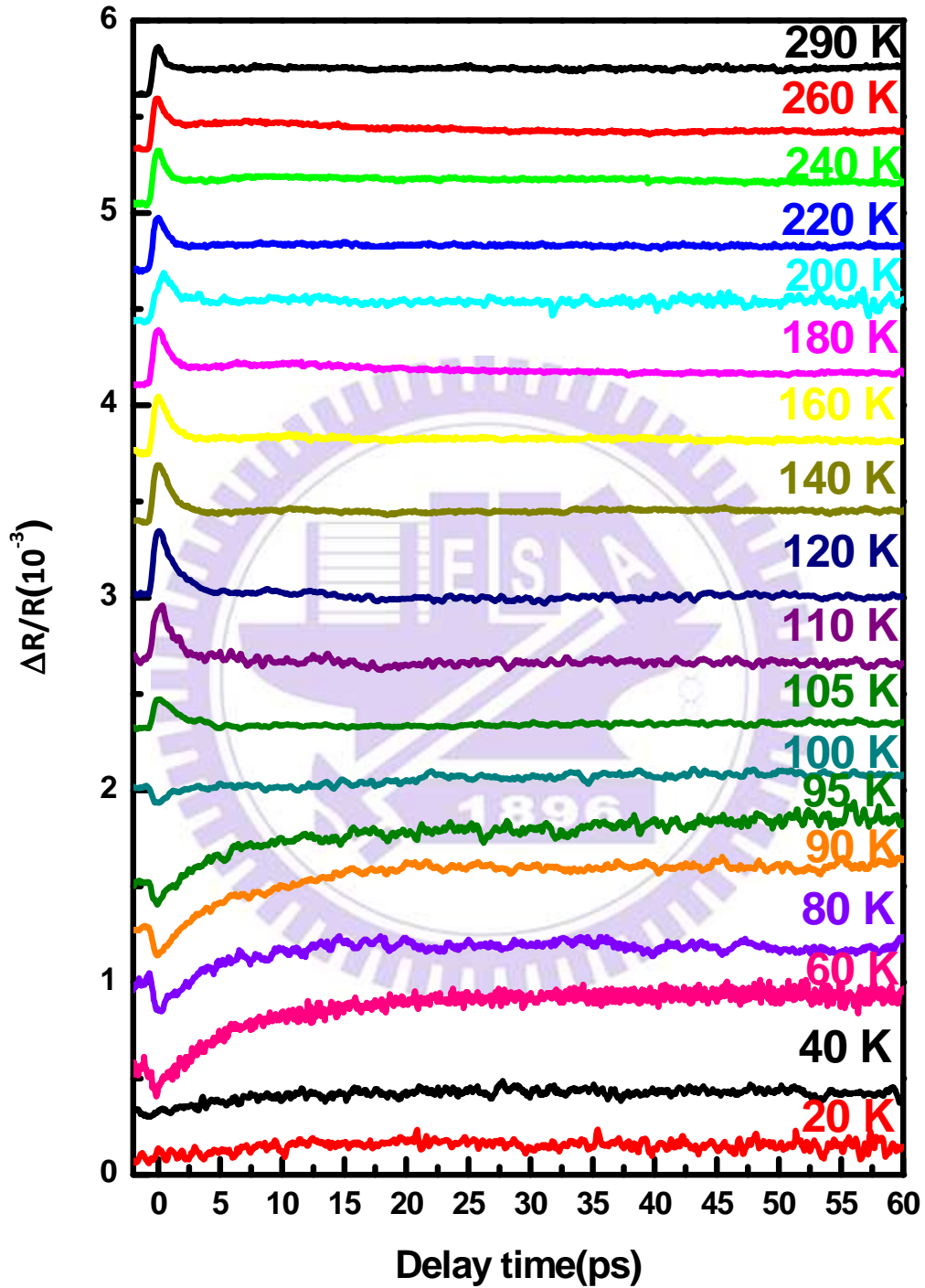


Fig. 4-16 The transient reflectivity $\Delta R/R$ curves of h -YMnO₃/YSZ(111) samples measured with the same pump and probe beam wavelength(770nm) at various temperatures.

Pump-Probe: 755nm-755nm

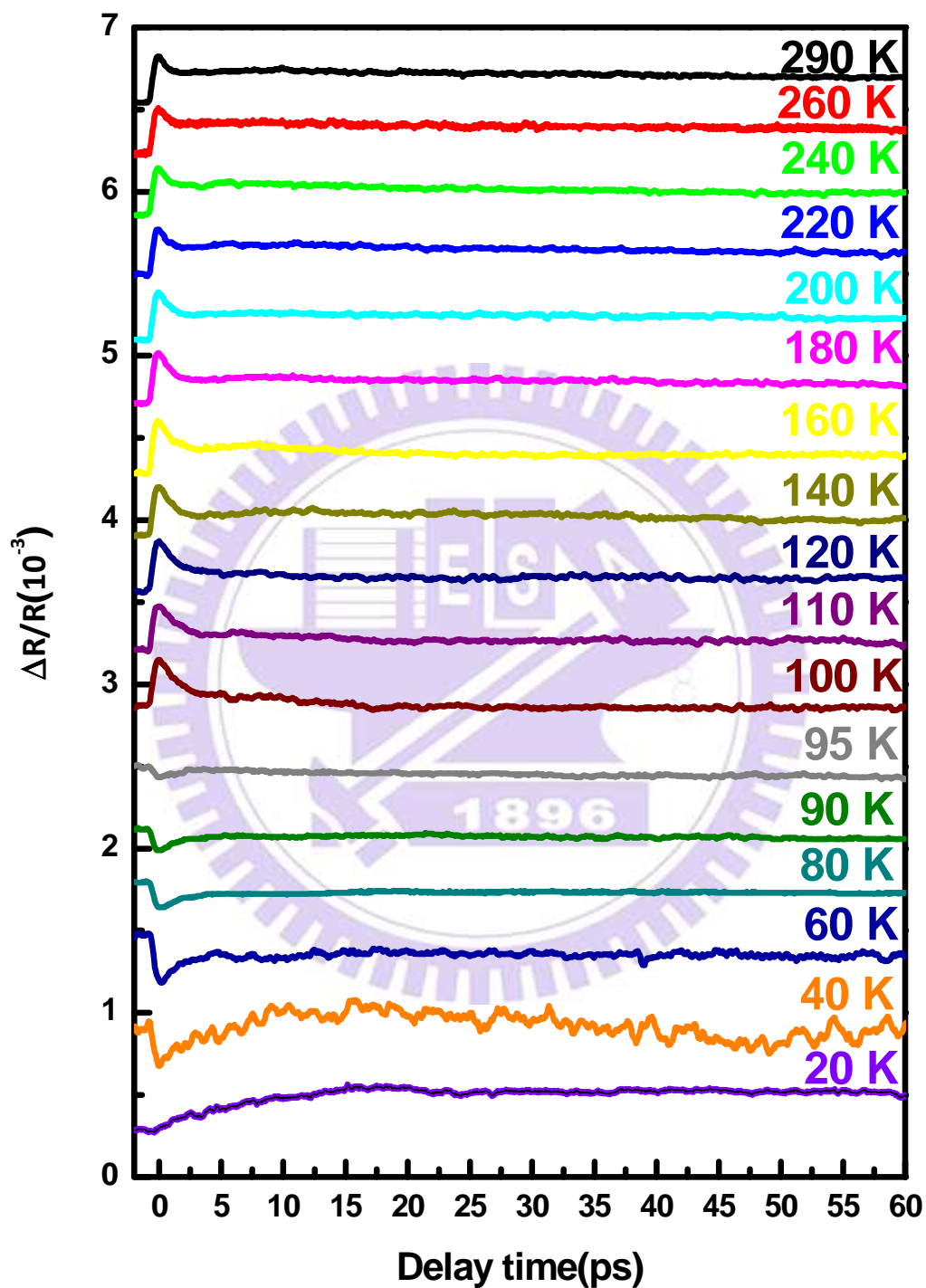


Fig. 4-17 The transient reflectivity $\Delta R/R$ curves of h -YMnO₃/YSZ(111) samples measured with the same pump and probe beam wavelength(755nm) at various temperatures.

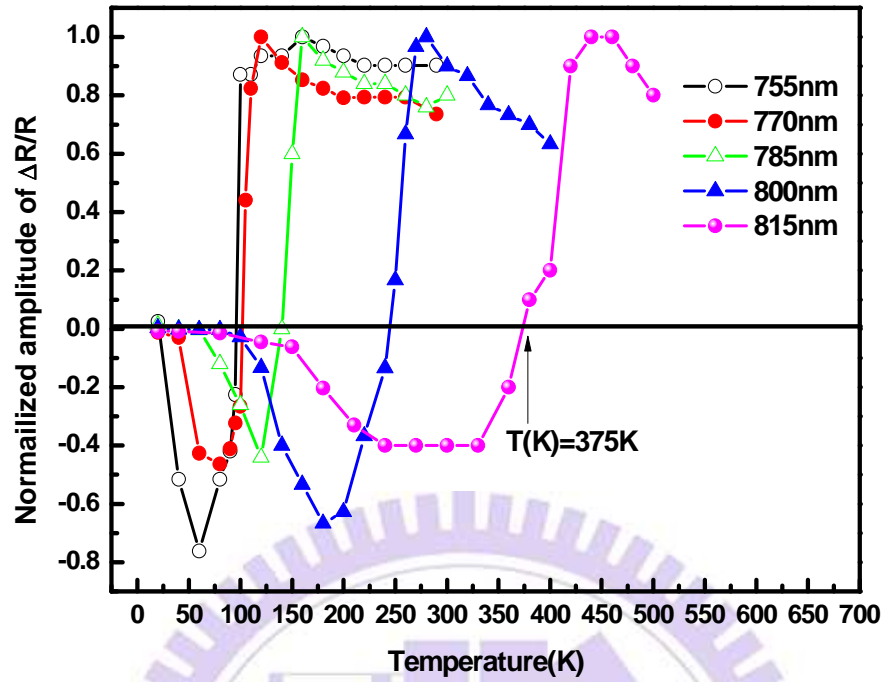


Fig. 4-18 Normalized amplitude of $\Delta R/R$ as a function of temperature of h -YMnO₃/YSZ(111) at various wavelengths (λ) at zero delay time.

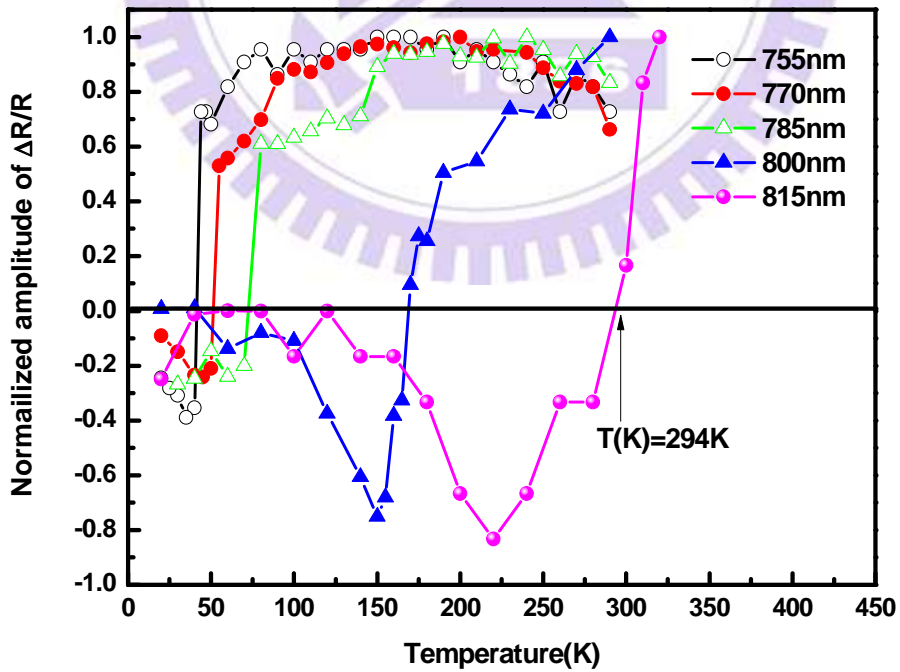


Fig. 4-19 Normalized amplitude of $\Delta R/R$ as a function of temperature of h -YMnO₃ single crystal at various wavelengths (λ) at zero delay time.

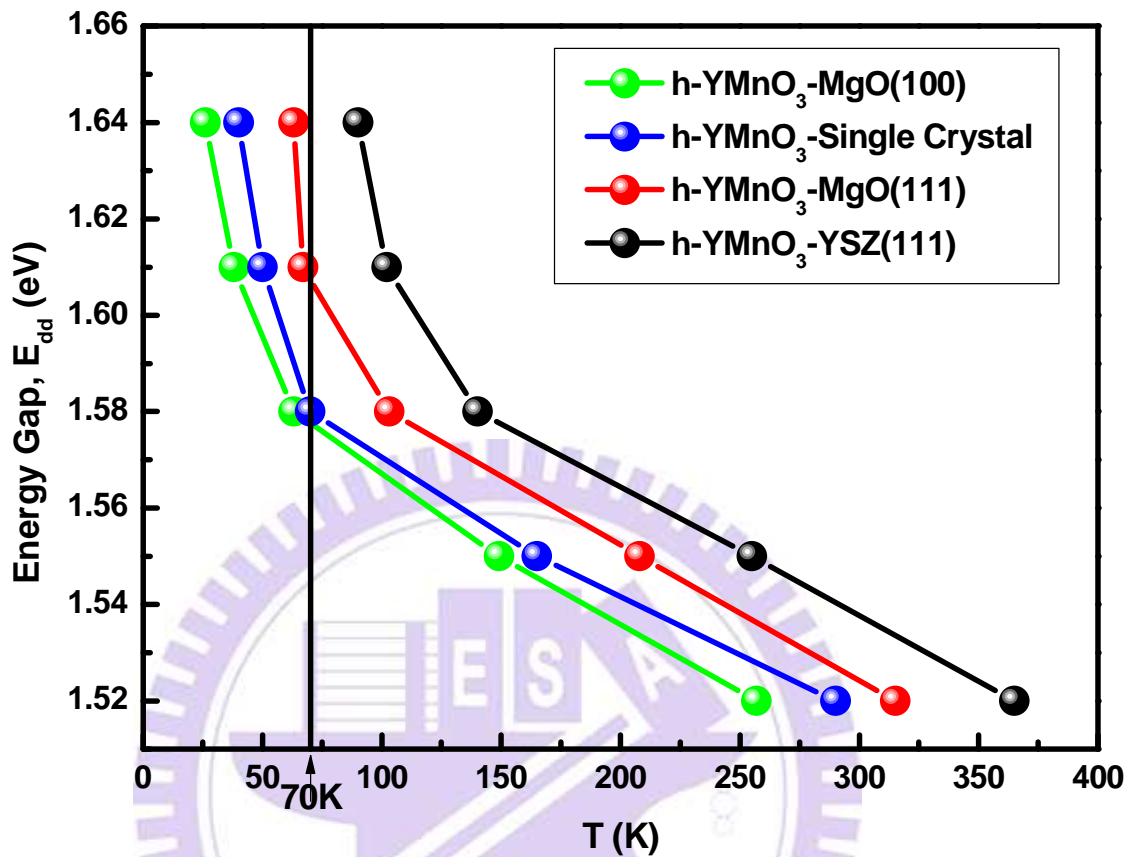


Fig.4-20 The energy gap E_{dd} as a function of temperature $T(K)$. E_{dd} is estimated from the different wavelengths (755,770,785,800,815nm). The black line is the T_N (Néel temperature) for the $YMnO_3$ single crystal to be a standard sample.

Fig.4-20 show the energy gap E_{dd} as a function of temperature $T (K)$. E_{dd} is estimated from the different wavelengths (755,770,785,800,815nm). The black line is the T_N (Néel temperature) for the h - $YMnO_3$ single crystal to be a standard sample.

Sample	YMO-MgO(100)	YMO-Single Crystal	YMO-MgO(111)	YMO-YSZ(111)
<i>a/c</i> ratio		0.538	0.543	0.548
<i>c</i> -axis lattice constant(Å)	11.440	11.404	11.387	11.319
<i>T</i> (K), $\Delta R/R=0$ at 1.55eV	149	165	208	255
E_{dd} (eV), at 200K	1.536	1.542	1.553	1.565

Table 4-1 The parameter of *a/c* ratio, *c*-axis lattice constant (Å), *T* (K, $\Delta R/R=0$) at 1.55eV, and E_{dd} (eV) at 200K of *h*-YMO/MgO(100), *h*-YMO/single crystal, *h*-YMO/MgO(111) and *h*-YMO/YSZ(111), respectively.

Due to Table 4-1 and Fig. 4-20, when *a/c* ratio increase from 0.538 to 0.548, the temperature of $\Delta R/R=0$ at 1.55eV will increase from 165K to 255K; the E_{dd} (eV) at 200K is relative to the *a/c* ratio increase from 1.542 eV to 1.565 eV **(about 23meV change if $\Delta(a/c)=0.01$).**

In the reference [16], the position of the first peak shows a systematic change between 1.61 eV and 1.81 eV, depending on the R (rare earth) ion. The vertical dotted line in Fig.4-21 indicates the first peak position of YMnO₃. **As the radius of the R ion increases from Y to Gd, the position of the first peak shifts to higher energy.** The shift in peak position becomes significant for artificially fabricated *h*-RMnO₃ films, especially *h*-GdMnO₃. The systematic change of the sharp optical transition peak in *h*-RMnO₃ implies that there should be systematic variations in their electronic structures depending on the radius of the R (rare earth) ion.

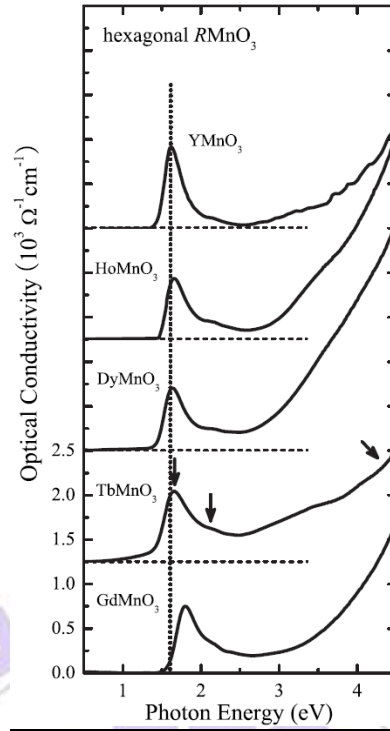


Fig.4-21 Optical conductivity spectra of hexagonal HoMnO_3 , DyMnO_3 , TbMnO_3 , and GdMnO_3 thin films. For clarity, the spectra have been plotted with offsets of $1250 \Omega^{-1} \text{cm}^{-1}$ vertically between each curve, and the base line for each curve is shown by the horizontal dashed line. The arrows in the TbMnO_3 spectrum indicate the three peak positions where optical absorption occurs. The vertical dotted line indicates the first optical transition peak position of YMnO_3 [16].

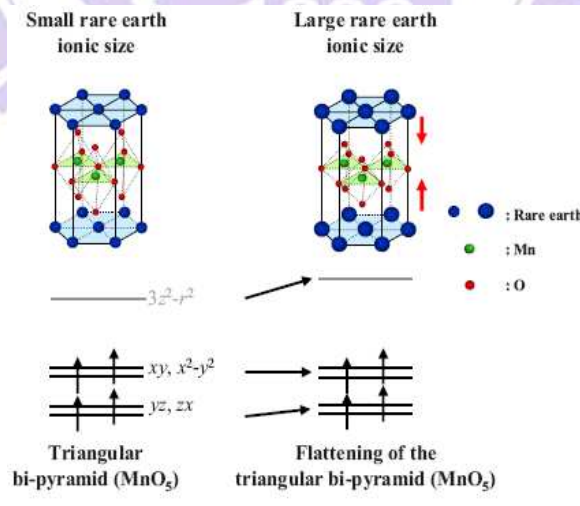


Fig. 4-22 Schematic representation of the crystal field splitting changes due to flattening of the MnO_5 triangular bipyramid. The flattening occurs due to the increase of the rare earth ionic radius with the fixed c -axis lattice constant. As the flattening occurs, due to the orbital symmetries, the $d_{3z^2-r^2}$ orbital will shift to higher energy, whereas the d_{xy} and $d_{x^2-y^2}$ orbitals stay the same [16].

According to Fig.4-22, the flattening occurs due to the increase of the rare earth ionic radius with the fixed c-axis lattice constant. As the flattening occurs, due to the orbital symmetries, the $d_{3z^2-r^2}$ orbital will shift to higher energy, whereas the d_{xy} and $d_{x^2-y^2}$ orbitals stay the same. **That is to say if c-axis lattice constant decrease, the a/c will increase show in Fig.4-23, then the E_{dd} will increase.**

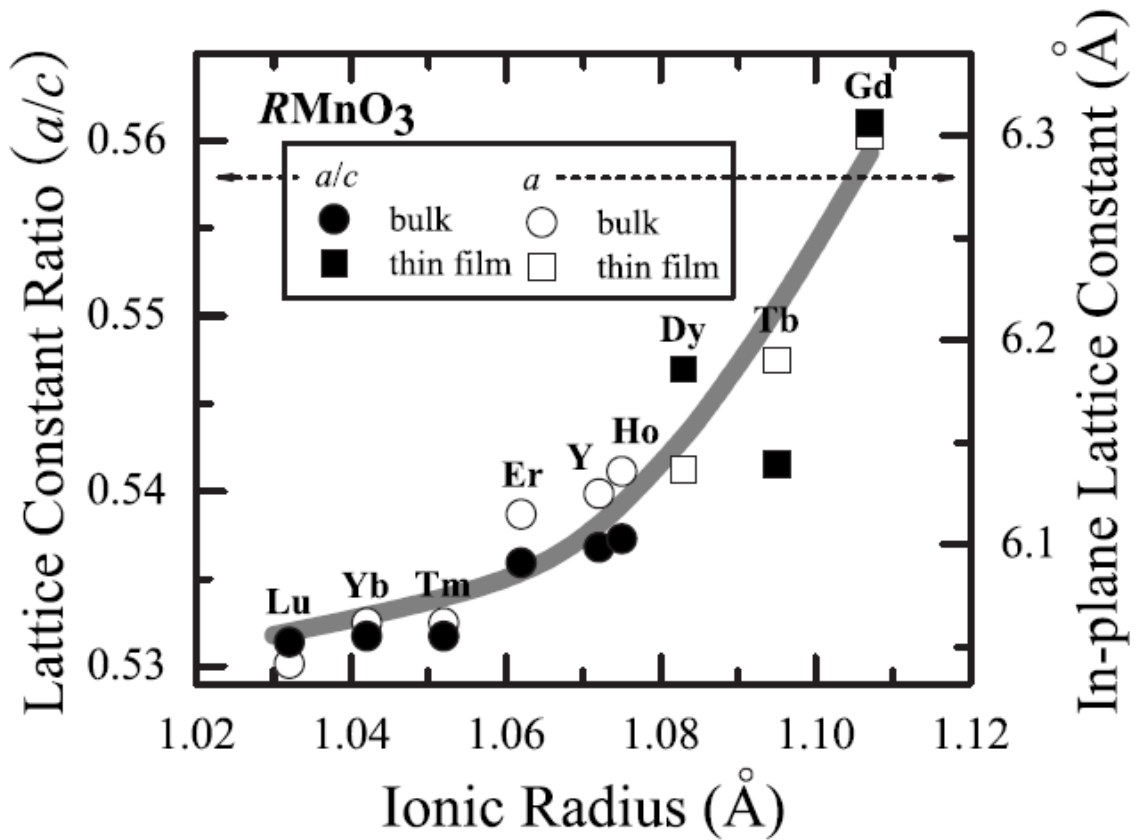


Fig.4-23 the lattice constant ratio (a/c , filled symbols) and the in-plane lattice constant (a , empty symbols) of bulk hexagonal $RMnO_3$ (circles, $R=Lu, Yb, Tm, Er, Y,$ and Ho [24]), and film hexagonal $RMnO_3$ (squares, $R=Dy, Tb,$ and Gd).

4-1-3 $\Delta R/R$ Signal analysis

In this section, we used fitting to analysis these data. The formula of fitting as following:

$$\frac{\Delta R}{R}(T, t) =$$

$$A_f(T)e^{-\frac{t}{\tau_f}} \dots\dots\dots \text{Electron dynamics}$$

$$+ A_{s_1}(T) \left[1 - e^{-\frac{t}{\tau_{s1'}}} \right] e^{-\frac{t}{\tau_{s1}}} \dots\dots\dots \text{Lattice dynamics}$$

$$+ A_{s_2}(T) \left[1 - e^{-\frac{t}{\tau_{s2'}}} \right] e^{-\frac{t}{\tau_{s2}}} \dots\dots\dots \text{Spin dynamics}$$

$$+ A_o(T)e^{-\frac{t}{\tau_d}} \cos(\omega_o t + \varphi_o) \dots\dots\dots \text{Coherent acoustic phonon}$$

Description as following:

1. For multiferroic material, there are two different time scales behavior of exponential decay. That is the equilibrium of electron-phonon (The faster decay behavior, the time scale is usually in sub-picosecond) and the equilibrium of spin-phonon (The slower decay behavior, the time scale is about several dozen of picosecond).

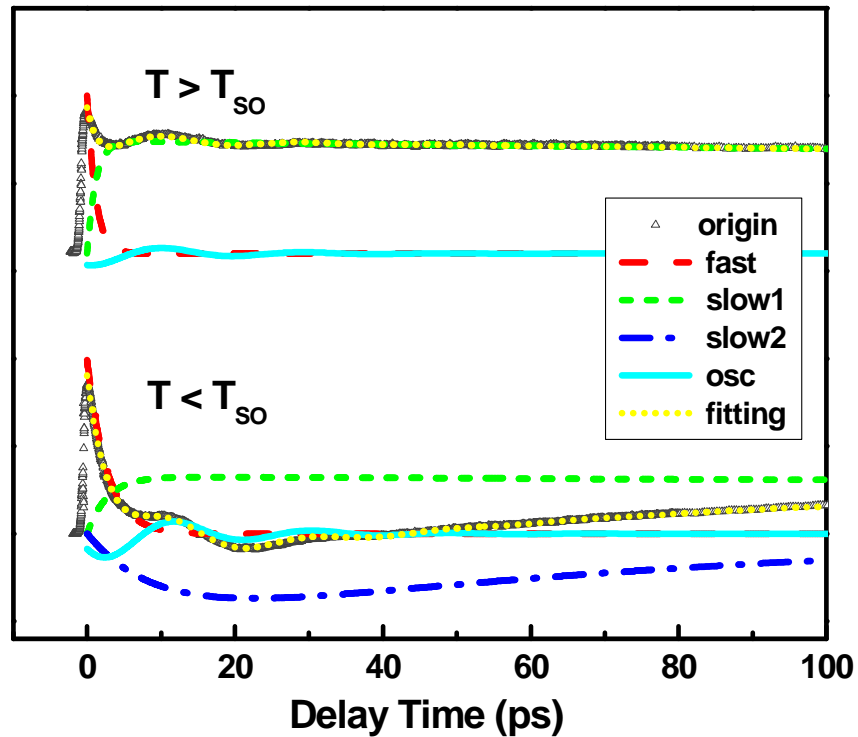


Fig.4-24 shows the fitting of h -YMnO₃. There are fast, slow1, slow2 and oscillation components. When $T < T_{so}$, we added a slow 2 component for magnetization.

When laser excited the sample surface, the localized electron absorbed the pulse energy, the temperature of electron in the system (T_e) increases rapidly. Hence, the electron-electron interaction let the localized electron get to thermal equilibrium. The time scale of electron-electron thermalization is about femtosecond. At present, electron temperature is larger than lattice temperature ($T_e > T_l$), the electron-lattice interaction will let the system into thermal equilibrium, related to fast and slow1 components in Fig.4-24 where electrons and lattice have the same temperature (T_{el}). The time scale of electron-lattice thermalization is about subpicosecond.

At this time, the temperature is different between electron-lattice and spin, so the spin system interacts with lattice and reaches thermal equilibrium, related

to Fig.4-24 slow1 and slow2 components. This process we called spin-lattice relaxation, and the time scale is several to several dozen picoseconds.

In addition, we can calculus the amplitude of slow component. The results show in Fig.4-25, it's the *h*-YMO/MgO(111) thin film slow component for magnetization. The amplitude of slow component appears to remain constant above 200K. It appears to the short range magnetic ordering under 200K. Moreover, the AFM correlation evolves in the sample as the temperature approaches Néel temperature (T_N), hence, we can see the long range ordering at 62K. Because the laser energy will increase the temperature of the sample about 5~10K, so the long range temperature equals to the Néel temperature approximately.

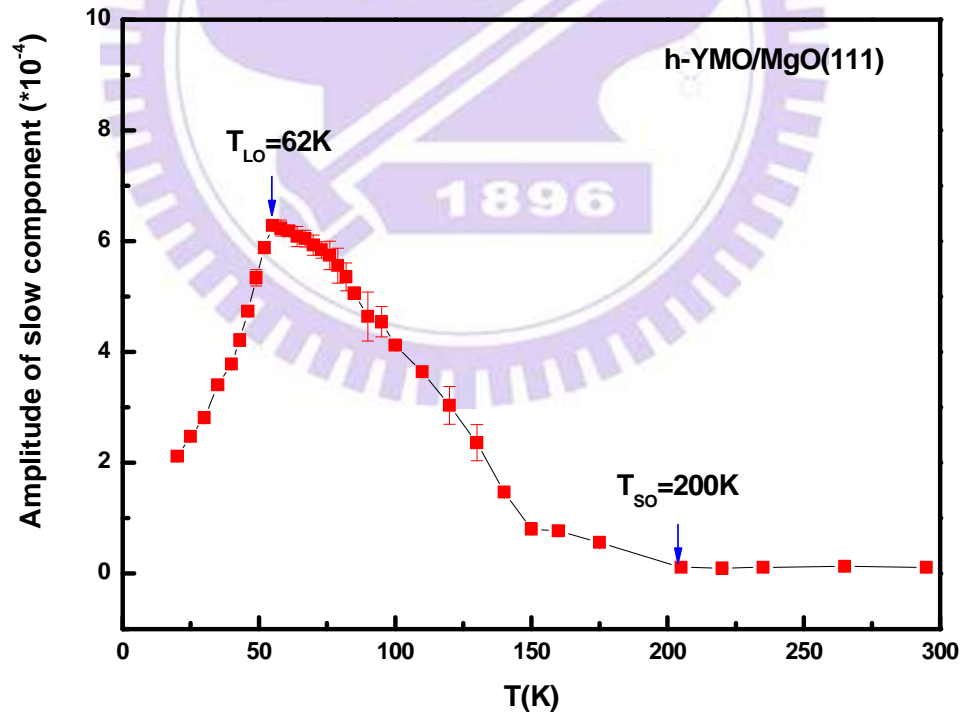


Fig.4-25 Amplitude of slow 2 component as various temperatures.

Below $T=200\text{K}$, it appears to the short range ordering gradually. The long range AFM ordering correlation evolves in the sample as the temperature approaches $T=62\text{K}$.

2. Coherent acoustic phonon term, it can explain by the strain pulse model [13]. After absorbing the energy of the excited beam, lattices will expansion due to temperature rising. Hence, it caused deformation wave into the film. When probe beam hit the deformation wave, the partial reflective wave will interfere with the reflective beam from the surface. As the following graph:

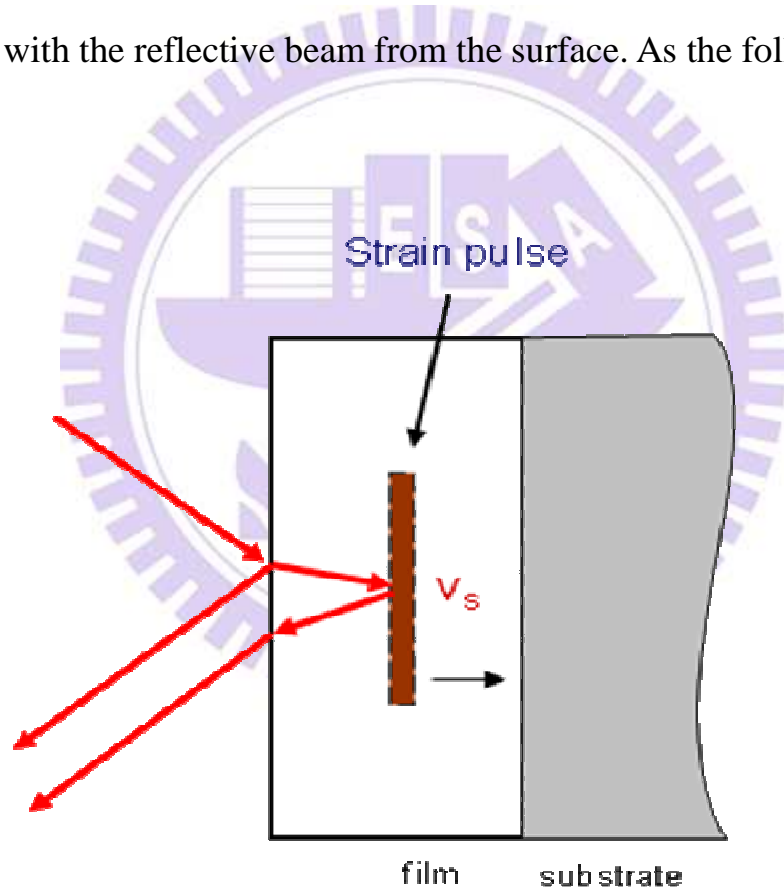


Fig.4-26 Strain pulse model (Interference between surface and strain layer).

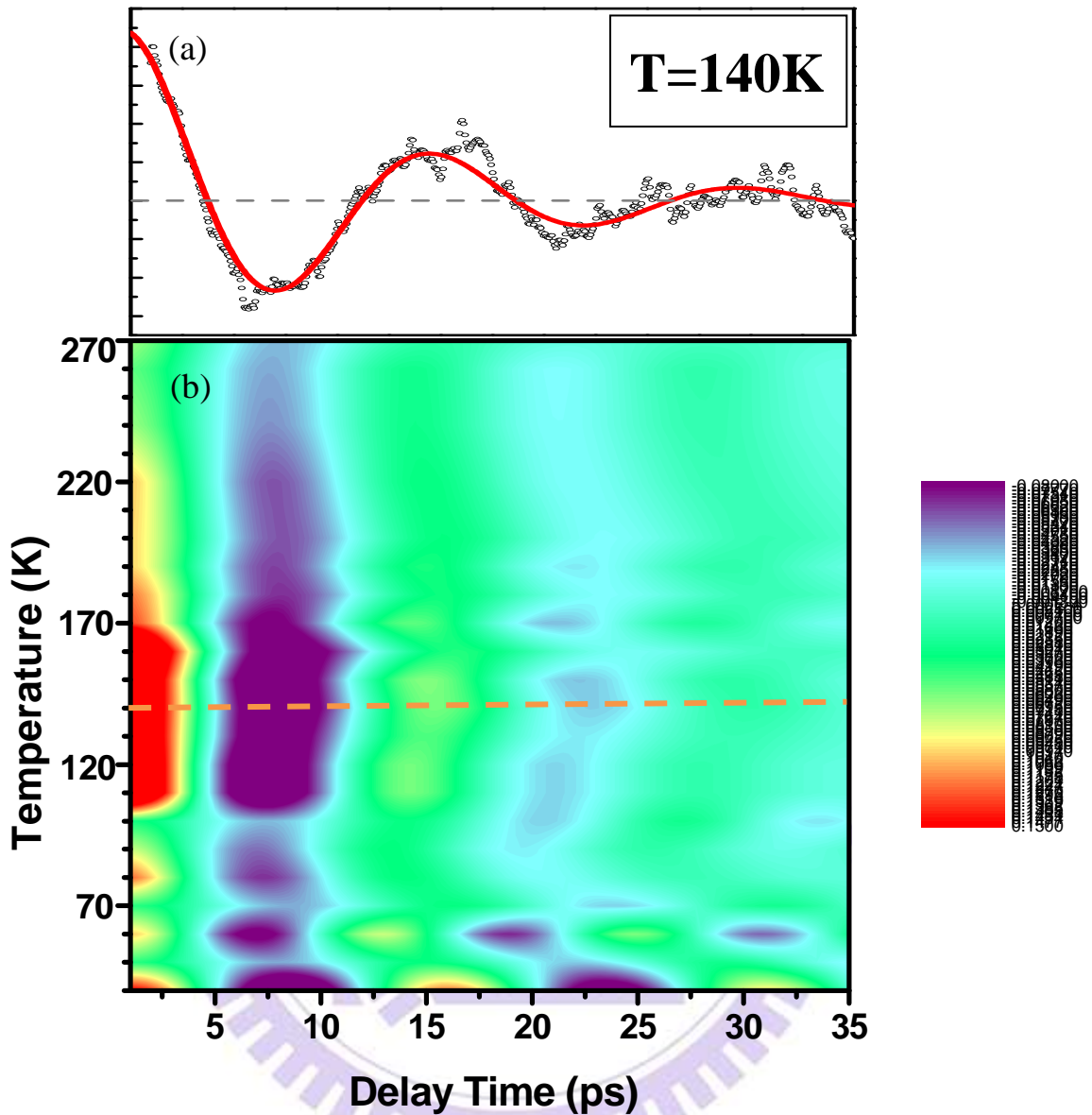


Fig.4-27 Coherent acoustic phonon mode measured at 140 K in (a) and at various temperatures in (b).

From Fig.4-27 we know, when the temperature drop slowly from the room temperature, the amplitude will increase gradually above $T=110\text{K}$. Below $T=110\text{K}$, it will drop quickly and there is a obviously peak at 62K , we think it called Néel temperature. Moreover, the period will rise quickly above $T=200\text{K}$, below $T=200\text{K}$, it begins to drop until its minimum at $T=62\text{K}$. Hence, at Néel temperature, long range ordering will influence on the lattice, the amplitude of

coherent acoustic phonon we can discover there is obviously change, the period become minimum and the frequency become faster (67GHz).

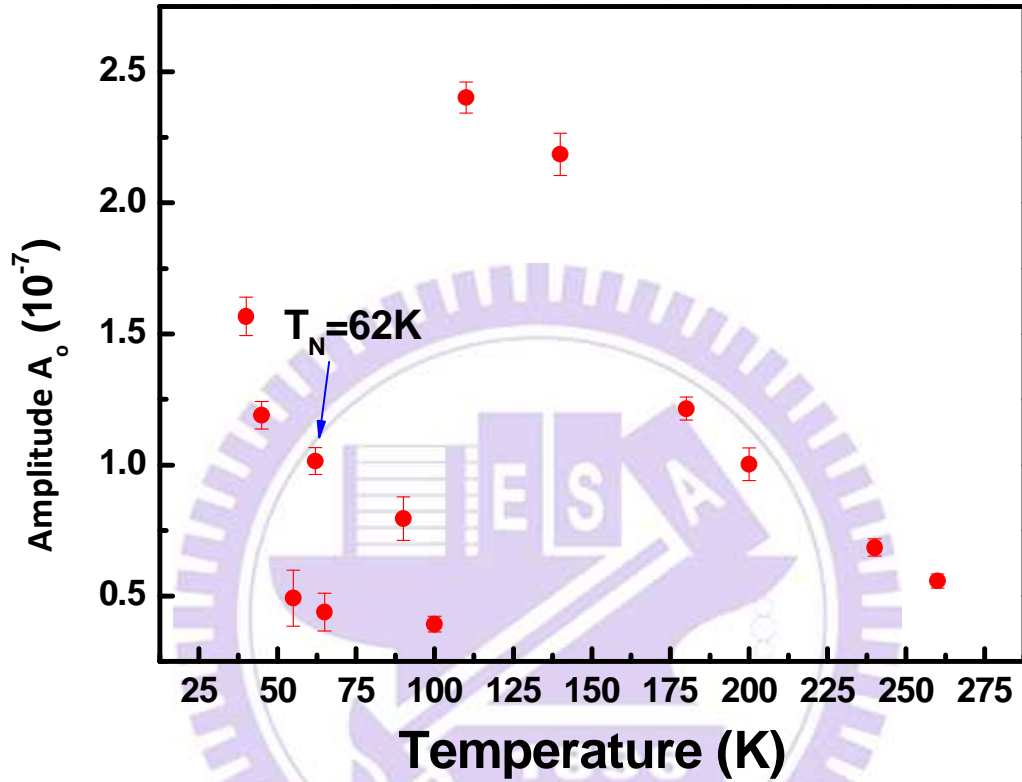


Fig.4-28 the amplitude (A_0) of coherent acoustic phonon mode at various temperatures.

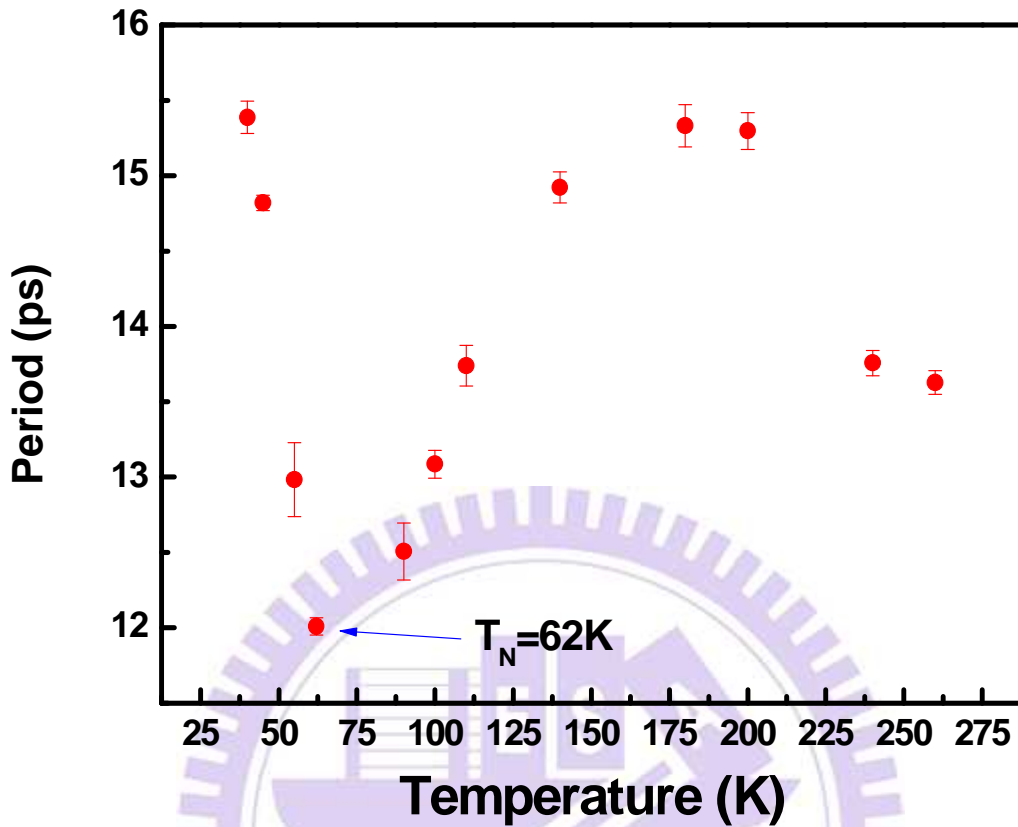


Fig.4-29 the period of coherent acoustic phonon mode at various temperatures.

Compare to the coherent acoustic phonon mode of amplitude and period, we can discover there are obviously change at $T=62\text{K}$, but this temperature is less than the AFM phase transition temperature ($T_N=70\text{K}$). Because the laser pulse hit the sample, it will cause heating effect. Hence, we used the below formula to calculus the heating effect in our sample.

$$\Delta T(x, y, z) = \frac{\alpha(1-R)P_L^3 e^{-\alpha z}}{4\pi^2 d^2 \kappa_x \kappa_y \kappa_z} \times$$

$$\int_0^{2\pi} d\varphi \int_0^\infty r \cdot dr \exp\left[-\left(\frac{x}{d} - \frac{r \cos \varphi}{\kappa_x d}\right)^2 - \left(\frac{y}{d} - \frac{r \sin \varphi}{\kappa_y d}\right)^2\right] \times$$

$$\left[\int_{\kappa_z z}^\infty \xi(u) du + \int_{-\kappa_z z}^\infty \xi(u) du \right]$$

Eq. 4-1 the formula of heating effect from reference [18].

According to Eq. 4-1 in the reference [19], we can get the $\Delta T(0,0,0)=12\text{K}$, $\alpha \sim 10^{-7} \text{ m}^{-1}$ [16], $R=0.35$ [20], $d=100 \mu \text{ m}$, $\kappa_{xy}=5\text{W/mk}$, $\kappa_z=10\text{w/mk}$ [21], $P = 50 \text{ mW}$. After calculating, we can know the heating effect will raise the temperature about 10K. If we consider the heating effect condition, the temperature ($T=62\text{K}$) can correspond to the phase transition temperature ($T_N=70\text{K}$).

4-2 Epitaxial-strain effect on Néel temperature shift

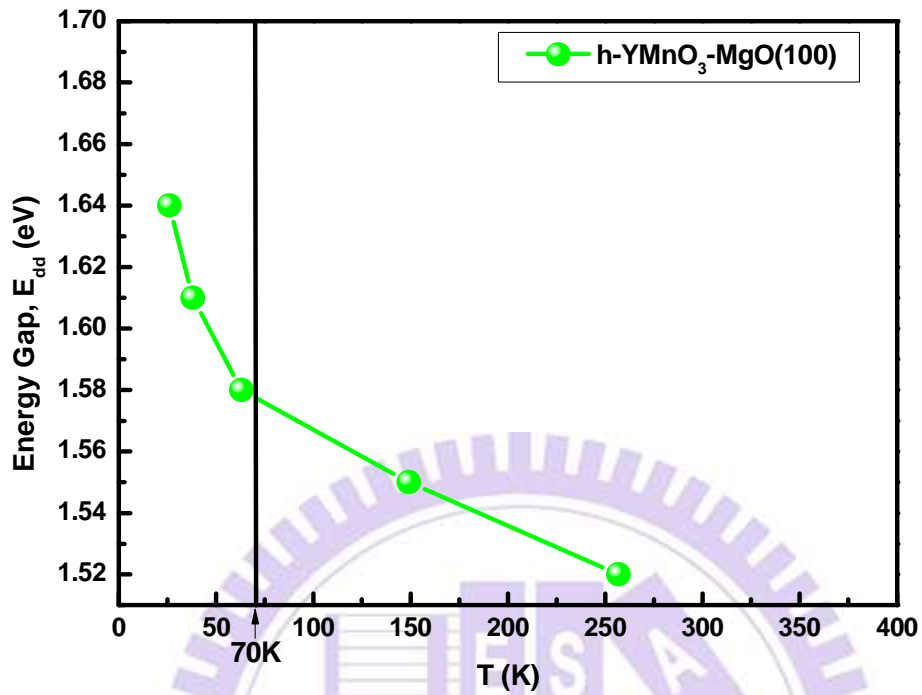


Fig.4-30 the energy gap E_{dd} as a function of T (K) for $h\text{-YMnO}_3\text{/MgO}(100)$.

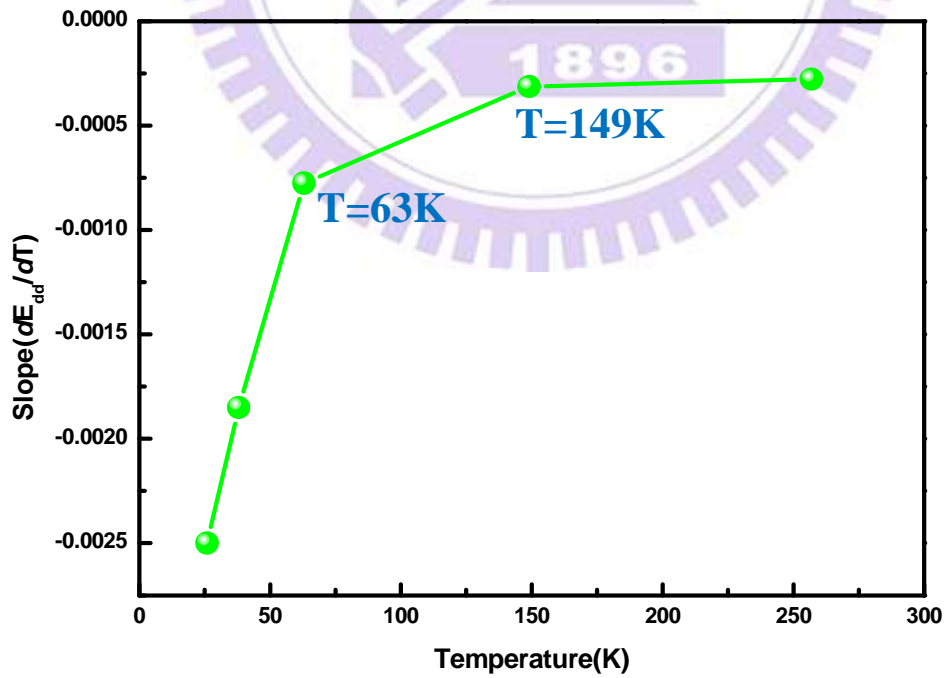


Fig.4-31 the slope (dE_{dd}/dT) as a function of T (K) for $h\text{-YMnO}_3\text{/MgO}(100)$.

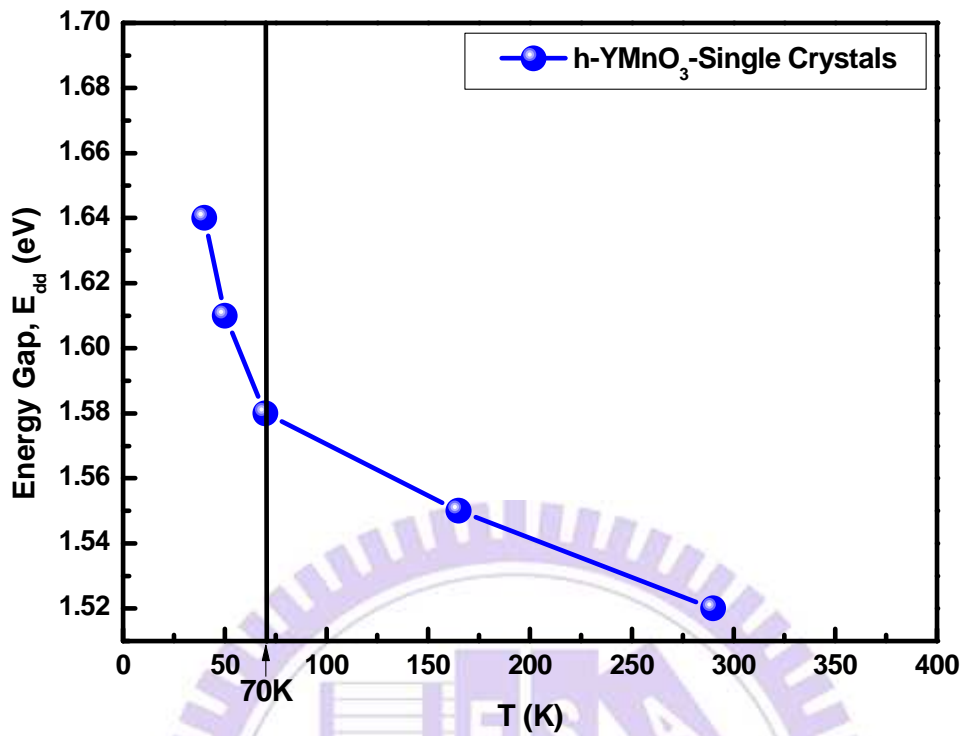


Fig.4-32 the energy gap E_{dd} as a function of T (K) for h -YMnO₃/Single Crystal.

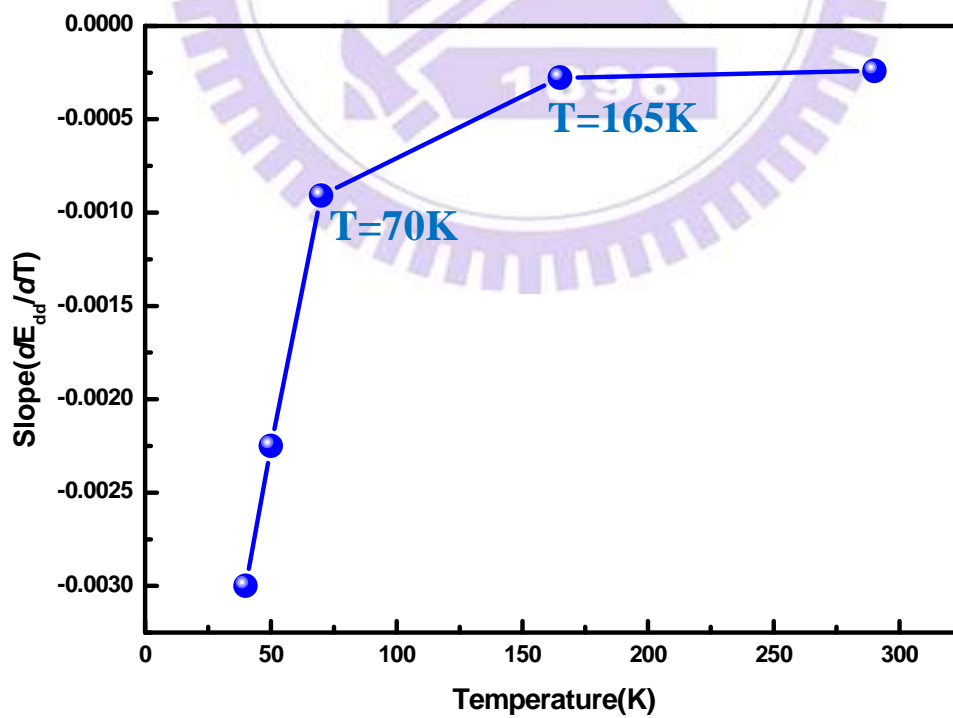


Fig.4-33 the slope (dE_{dd}/dT) as a function of T (K) for h -YMnO₃/Single Crystal.

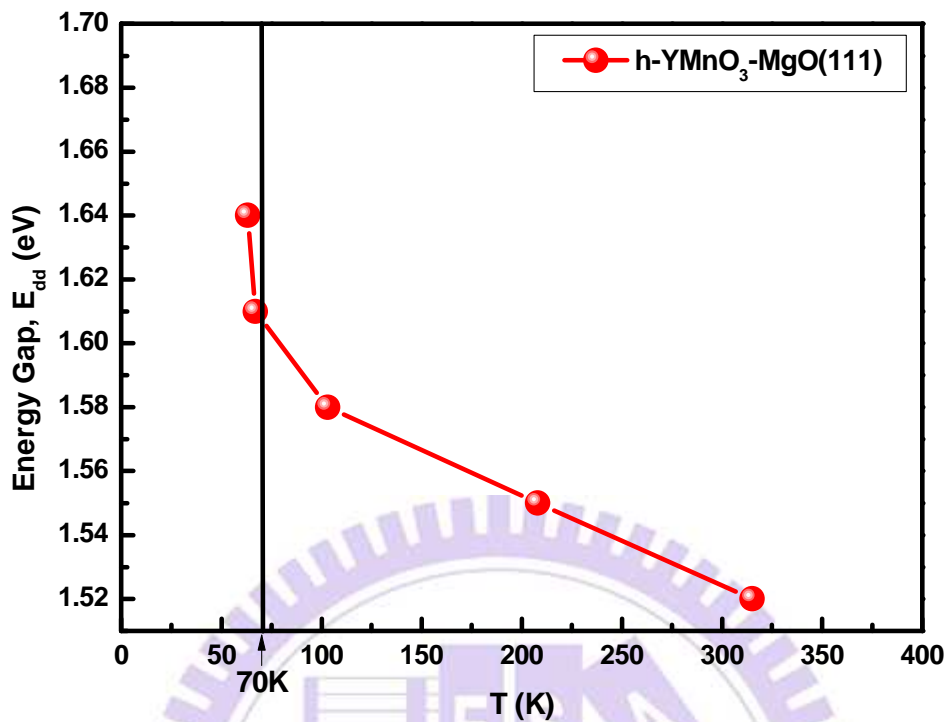


Fig.4-34 the energy gap E_{dd} as a function of T (K) for $h\text{-YMnO}_3$ /Single Crystal.

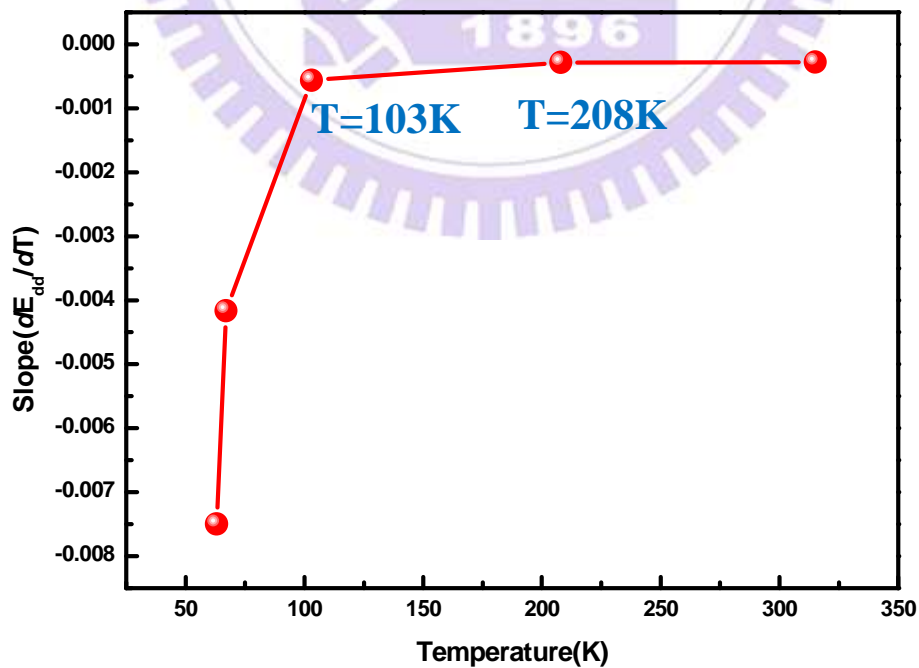


Fig.4-35 the slope (dE_{dd}/dT) as a function of T (K) for $h\text{-YMnO}_3\text{-MgO}(111)$.

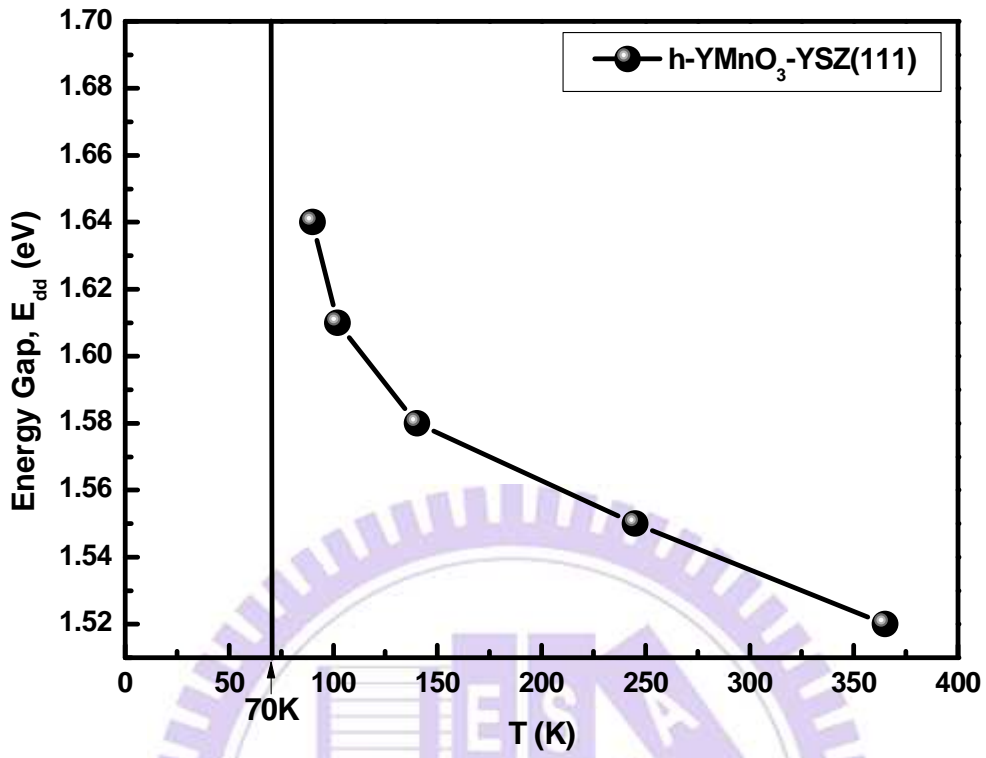


Fig.4-36 the energy gap E_{dd} as a function of T (K) for h -YMnO₃/YSZ(111)

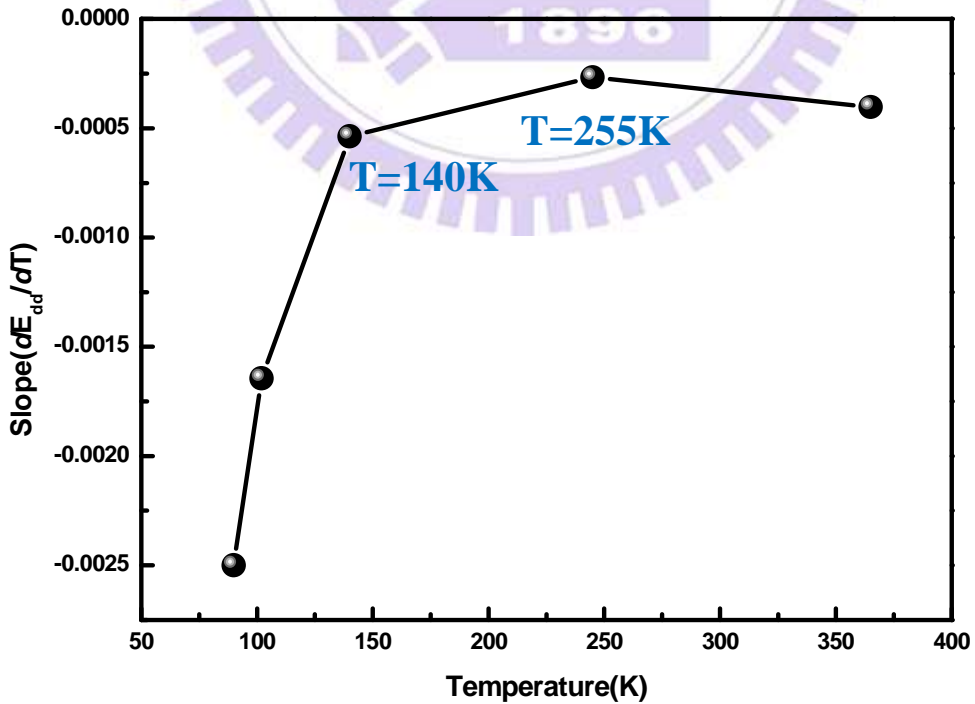


Fig.4-37 the slope (dE_{dd}/dT) as a function of T (K) for h -YMnO₃/YSZ(111).

Sample	YMO- MgO(100)	YMO- Single Crystal	YMO- MgO(111)	YMO- YSZ(111)
$T(K), \Delta R/R=0$ at 1.55eV	149	165	208	255
$T(K), \Delta R/R=0$ at 1.58eV	63	70	103	140

Table 4-2 the parameter of $T(K)$, $\Delta R/R=0$ at 1.55eV and 1.58eV of h -YMO/MgO(100), h -YMO/single crystal, h -YMO/MgO(111) and h -YMO/YSZ(111), respectively.

In table 4-2, we know the change of slope (dE_{dd}/dT) as a function of $T(K)$ for h -YMnO₃/MgO(100), h -YMnO₃/single crystal, h -YMnO₃/MgO(111) and h -YMnO₃/YSZ(111) is not obvious until it starts to change noticeably below 149 K, 165K, 208K and 255K, respectively. It begins to form the short range ordering. Furthermore, the slope starts to drop quickly at 63K, 70K, 103K and 140K, we think extra enhancement in the blueshift of E_{dd} due to the long-range ordering.

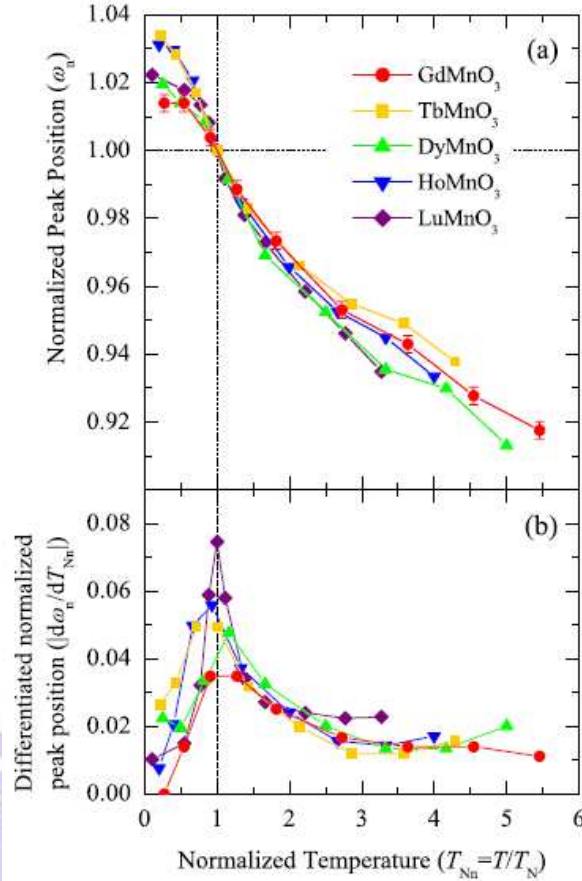


Fig.4-38 temperature dependence of the optical transition at ~ 1.7 eV.(a)Temperature dependence of the peak positions normalized to the peak position at $T_N(\omega_n)$ as a function of the normalized temperature $T_{Nn}(=T/T_N)$. Temperature values of 56, 70, 60, 75, and 90 K were used as T_N and the energy values of 1.9725, 1.77, 1.785, 1.7711, and 1.7249 eV were used as the peak energy values at T_N for R=Gd, Tb, Dy, Ho, and Lu, respectively. (b) Absolute value of normalized peak position differentiated to normalized temperature [22].

As shown in Fig. 4-38 (a), the normalized spectra for all h -RMnO₃ compounds show consistent temperature dependent features. The largest change in ω_n can be observed near T_N . In addition, the change in ω_n for $T > T_N$ is about three times larger than that for $T < T_N$. These observations suggest that all h -RMnO₃, including both single crystal bulk samples and thin-film samples, should experience similar changes in electronic structure in close relation with the magnetic state. To observe the temperature dependence of the ~ 1.7 eV peak position more clearly, Fig.4-38 (b) show the absolute differentiated values of the

normalized peak position at each temperature point. As shown in Fig.4-38(b), there is a clear peak at T_N . **The largest change in the optical spectra across T_N implies that a significant change in the electronic structure of $h\text{-RMnO}_3$ occurs due to the effect of long-range antiferromagnetic ordering.** The result is corresponding to our observation, which is the phenomenon of anomalous blueshift near T_N . This behavior strongly suggests coupling between the electronic structure and the magnetic structure through a strong charge-spin interaction.

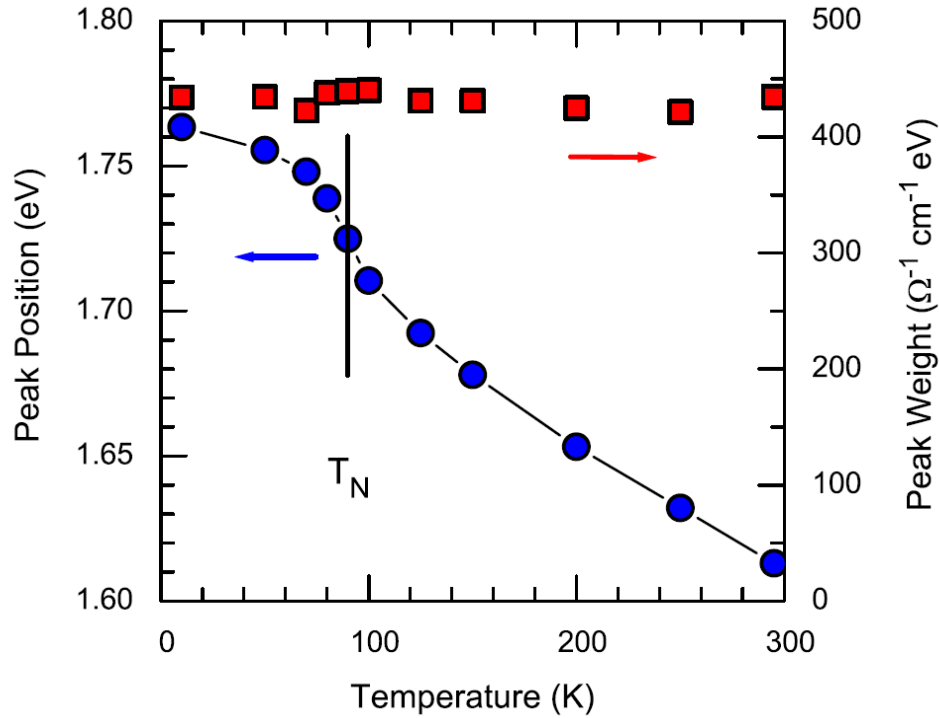


Fig.4-39 temperature dependence of the peak energy (Blue circle) of the 1.7 eV feature and its spectral weight (Red square) [23].

Moreover, in Fig.4-39 [23], the peak position of LuMnO_3 will shift obviously near T_N . The origin of ~ 0.15 eV shift of the 1.7 eV peak with temperature shown in Fig. 4-39. A spectral shift due to thermal expansion mainly from 300K to 200K is expected. From 200K to 100K, the peak position starts to shift quickly. The anomalous shift at T_N indicates that the mainly shift is

associated with the magnetic phase transition. However, the observed shift is larger than is typically observed in interband features in red square (~ 0.1 eV). We attribute to the magnetic part of the shift to the effects of the exchange interactions between the Mn ions. The shift of the Mn d levels due to superexchange between Mn neighbors leads to a lowering of the $d_{x^2-y^2}$ and d_{xy} (e_{2g}) in the antiferromagnetic state, while the relatively $d_{3z^2-r^2}$ orbital is little affected.

According to above discussion, the anomalous blueshift of E_{dd} in the optical spectra near T_N in the electronic structure of h -RMnO₃ occurs due to the effect of long-range AFM ordering.

Consequently, when $\Delta(a/c)=0.01$ between h -YMnO₃/single crystal and h -YMnO₃/YSZ(111), it will cause the Néel temperature shift to higher temperature (from 70K to 140K, $\Delta T=70$ K).

Chapter 5 Summary and future work

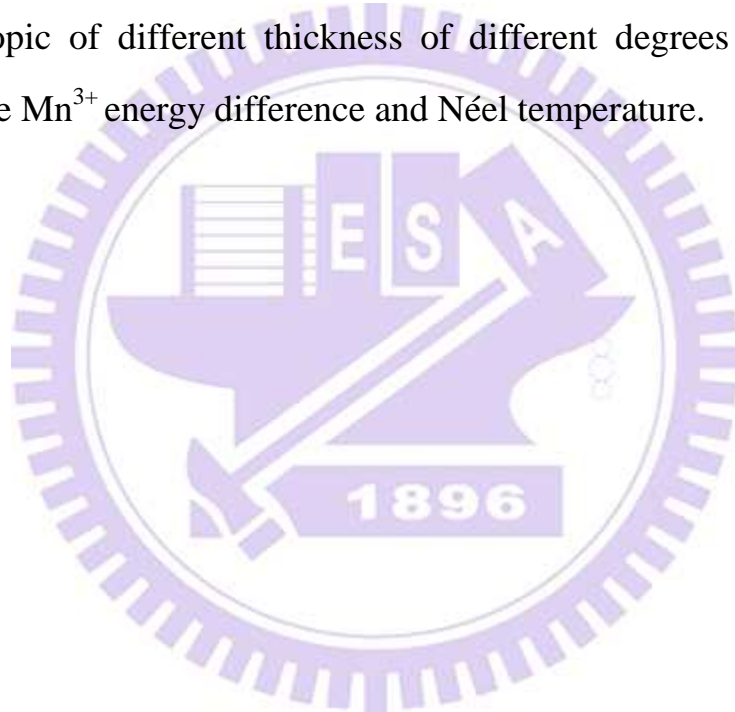
5-1 Summary

We prepared pure (001)-oriented hexagonal YMnO₃ (*h*-YMnO₃) thin films on (100)MgO, (111)MgO and (111)YSZ substrates with good quality by pulsed laser deposition, respectively. We found that E_{dd} change due to the small change of the ratio of lattice constants a/c . Not only the effect of strain due to lattice mismatch between the substrate and *h*-YMnO₃ films, but also decreasing temperature could be due to the flattening of the MnO₅ bipyramids and increase in the a/c ratio. We found that E_{dd} change ($\Delta E_{dd}=23\text{meV}$) due to the small change of the ratio of lattice constants a/c ($\Delta(a/c)=0.01$).

The anomalous blueshift of E_{dd} in the optical spectra near T_N in the electronic structure of *h*-RMnO₃ occurs due to the effect of long-range AFM ordering. Moreover, $\Delta(a/c)=0.01$ will cause the Néel temperature shift (from 70K to 140K, $\Delta T=70\text{K}$)

5-2 Future work

Except for using different substrates make the different effect of strain on h -YMnO₃ films, we can also get the different thickness of h -YMnO₃ thin films by changing the pulse number. In chapter 2, we show the relationship of c -axis lattice constant and pulse number. When the pulse number decrease from 9KP to 1.5KP, c -axis lattice constant become smaller from 11.3193 Å to 11.2969 Å (~ 0.0224 Å), ratio of out-of-plane change from -0.739% to -0.936% ($\sim 0.2\%$). Chances are that we can use the tunable wavelength pump-probe technique to research the topic of different thickness of different degrees of strain effect influence on the Mn³⁺ energy difference and Néel temperature.



References

- [1] H. Schmid, Multiferroic Magnetoelectrics, *Ferroelectrics* 162, 317 (1994).
- [2] W. Eerenstein, N. D. Mathur and J. F. Scott, *Nature* 442, 759-765(2006).
- [3] (a) P. Curie, *J. Phys.* 1894, 3, 393; (b) L. D. Landau, E. M. Lifshitz, *Electrodynamics of Continuous Media*, Pergamon Press, Oxford, 1960; (c) D. N. Astrov, *Sov. Phys. JETP* 1960, 11, 708; (d) G. T. Rado, V. J. Folen, *Phys. Rev. Lett.* 7, 310 (1961).
- [4] Bas B. Van Aken, Thomas T. M. Palstra, Filippetti Alessio and Nicola A. Spaldin, *Nat. Mater.* 3, 164 (2004).
- [5] Seongsu Lee, A. Pirogov, Jung Hoon Han, J. G. Park, A. Hoshikawa, and T. Kamiyama, *Phys. Rev. B* 71, 180413 (2005).
- [6] Seongsu Lee, A. Pirogov, Misun Kang, Kwang Hyun Jang, M. Yonemura, T. Kamiyama, S. W. Cheong, F. Gozzo, Namsoo Shin, H. Kimura, Y. Noda & J. G. Park, *Nat. Mater.* 451, 805 (2008).
- [7] N. Fujimura, T. Ishida, T. Yoshimura, T. Ito, *Appl. Phys. Lett.* 69, 1001-1013 (1996).
- [8] M. N. Iliev, H. G. Lee, V. N. Popov, M. V. Abrashev, A. Hamed, R. L. Meng, C. W. Chu, *Phys. Rev. B.* 56 , 2488-2494(1997).
- [9] T. Lonkai, D. Hohlwein, J. Ihringer, W. Prandl, *Applied Physics a-Materials Science & Processing.*74, 843-845(2002).
- [10] D. Y. Cho, J. Y. Kim, B. G. Park, H. J. Noh, B. J. Kim, S. J. Oh, H. M. Park, J. S. Ahn, H. Ishibashi, S. W. Cheong, J. H. Lee, P. Murugavel, T. W. Noh, A. Tanaka, and T. Jo, *Phys. Rev. Lett.* 98., 217601 (2007).
- [11] H. C. Shih, T. H. Lin, C. W. Luo, J.-Y. Lin, T. M. Uen, J. Y. Juang, K. H.

- Wu, J. M. Lee, J. M. Chen, and T. Kobayashi, *Phys. Rev. B* 80, 024427(2009).
- [12] A. K. Singh, M. Snure, A. Tiwari, and S. Patnaik, *J. Appl. Phys* 106, 014109 (2009).
- [13] T. F. Tsai, "Ultrafast Dynamic in YMnO_3 Thin Films Probed by Femtosecond Spectroscopy", a Master Thesis in National Chiao Tung University Electrophysics(2007).
- [14] A. Muñoz, J. A. Alonso, M. J. Martínez-Lope, M. T. Casáis, J. L. Martínez, M. T. Fernández-Díaz, *Phys. Rev. B* 62, 9498(2000).
- [15] C. W. Luo," Anisotropic Ultrafast Dynamics in $\text{YBa}_2\text{Cu}_3\text{O}_{7-\delta}$ Probed by Polarized Femtosecond Spectroscopy" , a PH.D Thesis in National Chiao Tung University Electrophysics(2007).
- [16] W. S. Choi, D. G. Kim, Sung Seok A. Seo, S. J. Moon, D. Lee, J. H. Lee, *Phys. Rev. B* 77, 045137, (2008).
- [17] W. C. YI, S. I. Kwun, J. G. Yoon, *J. Phys. Soc. Jpn.* 69, 2706-2707 (2000).
- [18] C. Thmosen, H. T. Grahn, H. J. Maris and J. Tauc , *Phys. Rev. B* 34, 6 (1986).
- [19] D. Mihailovic, J. Demsar, in "Spectroscopy of Superconducting Materials", ACS Symposium Series 730, Ed. E. Faulques, 230-244 (1999).
- [20] S. H. Kim, S. H. Lee, T. H. Kim, T. Zyung, Y. H. Jeong, M. S. Jang, *Cryst. Res. Technol.* 35, 1 (2000).
- [21] J. S. Zhou, J. B. Goodenough, J. M. Gallardo-Amores, E. Morán, M. A. Alario-Franco, and R. Caudillo, *Phys. Rev. B* 74, 014422 (2006).
- [22] W. S. Choi, S. J. Moon, S. S. A. Seo, D. Lee, J. H. Lee, P. Murugavel, T. W. Noh, and Y. S. Lee, *Phys. Rev. B* 78, 054440 (2008).

- [23] B. Souchkov, J. R. Simpson, M. Quijada, H. Ishibashi, N. Hur, J. S. Ahn, S. W. Cheong, A. J. Millis, and H. D. Drew, Phys. Rev. Lett.91, 2(2003).

